Tuning Functionality of Photocatalytic Materials

An infrared study on hydrocarbon oxidation

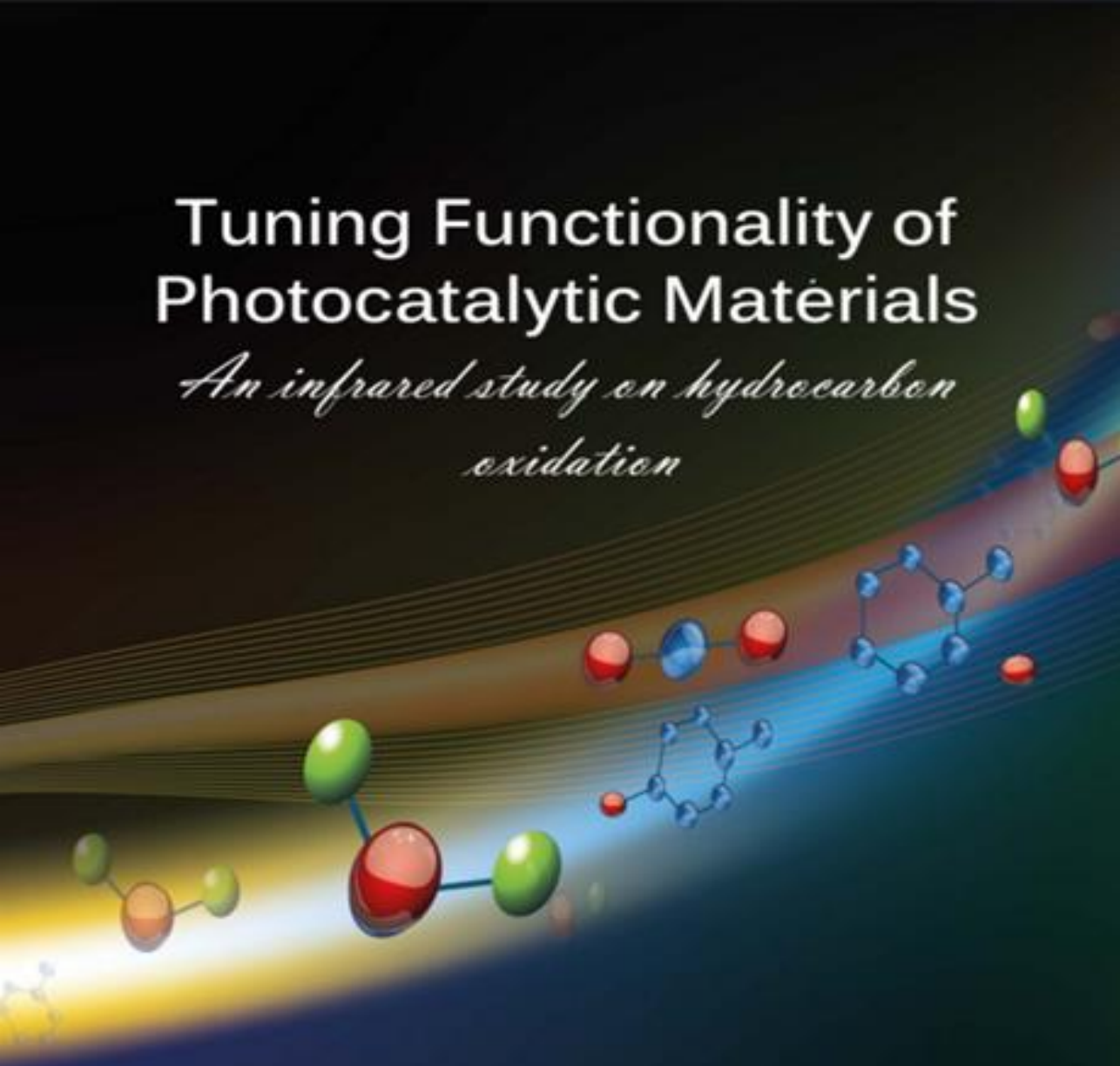

Rezvaneh Amrollahi Buky

TUNNING FUNCTIONALITY OF PHOTOCATALYTIC MATERIALS:
AN INFRARED STUDY ON HYDROCARBON OXIDATION

Rezvaneh Amrollahi Buky

Graduation committee:

Prof. dr. ir. J.W.M. Hilgenkamp, chairman	University of Twente
Prof. dr. G. Mul (Promoter)	University of Twente
Prof. dr. M. S. Hamdy (Assistant-promoter)	King Khalid University
Prof. dr. ir. L. Lefferts	University of Twente
Prof. dr. ir. J. E. ten Elshof	University of Twente
Prof. dr. ir. R. G. H. Lammertink	University of Twente
Prof. dr. J. A. Anderson	University of Aberdeen
Dr. J. Strunk	Max-Planck Institute for Chemical Energy Conversion

The research described in this thesis was carried out in the PhotoCatalytic Synthesis (PCS) group within the Faculty of Science and Technology (TNW), and the MESA+ Institute for Nanotechnology at the University of Twente, The Netherlands.

Cover design: Hadis Roghangarha and Rezvaneh Amrollahi Buky
Printed by Ridderprint B. V., Ridderkerk, the Netherlands

Author's email: Amrollahi.R@gmail.com
ISBN number: 978-90-365-4065-0
DOI-number is:10.3990/1.9789036540650

TUNNING FUNCTIONALITY OF PHOTOCATALYTIC MATERIALS:
AN INFRARED STUDY ON HYDROCARBON OXIDATION

DISSERTATION

to obtain
the degree of doctor at the University of Twente,
on the authority of the rector magnificus,
Prof.dr. H. Brinksma,
on account of the decision of the graduation committee,
to be publicly defended
on Friday February 26th, 2016 at 16:45

by

Rezvaneh Amrollahi Buky

born on the 24th August 1983 .
in Tehran, Iran

This dissertation has been approved by:
Prof. dr. Guido Mul (Promoter)
Prof. dr. Mohamed S. Hamdy (Assistant-promoter)

Contents

Chapter 1

General introduction

1. Background

Research in photocatalysis attracts a lot of attention, since photocatalysis can be applied for mitigation of several environmental issues, such as i) air and water purification, including decomposition of pollutants and eliminating bacteria and viruses, and ii) conversion of solar energy into chemical energy, e.g. by decomposition of water to hydrogen and oxygen [1]. Photocatalysis is "the change in the rate of a chemical reaction or its initiation under the action of ultraviolet, visible or infrared radiation in the presence of a substance, the photocatalyst, which absorbs light and is involved in the chemical transformation of the reaction partners." (IUPAC 2007). A photocatalyst can be activated by light absorption, which generates so-called electron/ hole pairs. This is possible when the energy of light is equal or larger than the band gap energy (E_g) of the photocatalyst. Generally, electrons and holes tend to recombine. However, if they can reach the surface of the catalyst, they can react at the same time with an electron acceptor (e.g. protons or oxygen) and an electron donor, such as water or various (adsorbed) organic compounds. In Scheme 1, for example the conversion of methylcyclohexane to 2-methylcyclohexanone is shown, initiated by a photo-excited catalyst. Electrons induce formation of super oxide anions, and holes the formation of hydroxyl radicals, both species with a sufficient oxidation potential able to induce methylcyclohexane conversion.

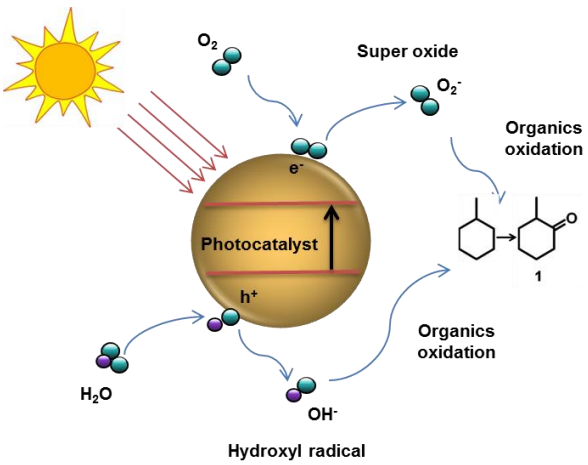

Scheme 1: The conversion of methylcyclohexane to 2-methylcyclohexanone using a photo-excited catalyst.

2. Photocatalytic materials

There are two types of photocatalysis; homogeneous and heterogeneous. In homogeneous photocatalysis, the photocatalyst and the reactants are present in the same phase. Examples of homogeneous photocatalysis include the Fenton reaction [2] or catalysis by photo-excited metal complexes [3]. Homogeneous photocatalysis can be used in water treatment, however the difficulties in removing the photocatalyst is a matter of concern. In heterogeneous photocatalysis, reactants and the photocatalyst are belonging to different phases, the catalyst being present as a coating or slurry in contact with gas phase or liquid phase media, respectively. Heterogeneous photocatalysis has been widely explored in the area of water treatment [4], air purification [5] and stimulation of organic chemistry [6].

2.1. TiO_2

Titanium dioxide (TiO_2) has been extensively studied as a photocatalyst in environmental applications. TiO_2 is an attractive photocatalyst since it is a cost-effective material, abundantly available, stable, and chemically and biologically inert. The photoactivity of TiO_2 depends on its crystallographic structure. The most relevant microcrystalline structures are anatase, rutile and brookite. The structure-activity relation of TiO_2 is strongly dependent on the reactant. For some reactions, literature shows the anatase phase induces the highest activity, while for some other substrates P25, composed of a mixture of rutile and anatase, is reported being the most attractive photocatalyst. In this thesis we used rutile and P25 (75% anatase and 25% rutile) as reference catalysts to compare activity of novel, modified photocatalysts.

TiO_2 has a wide band-gap (3.2 eV), and can only absorb ultraviolet (UV) light. This limits the use of TiO_2 in large scale industrial applications notably, since solar light contains only 4-5% UV radiation [7]. Therefore, around 15 years ago, researchers have directed their efforts to modify TiO_2 to allow activation by visible light, and at the same time introduce highly reactive sites on the surface via several modifications such as:

- Doping TiO_2 with transition element ions [8]: the aim of this modification is to reduce the band gap of TiO_2 by incorporating small amounts of transition metal ions into the lattice of TiO_2, such as ionic forms of Cr, V, Fe and Cu.
- Promoting TiO_2 with metallic nanoparticles [9]: metallic nanoparticles (e.g. Pt , Rh , Ru and Pd) act as an electron ‘beacon’ (reducing electron/hole

recombination), as well as catalytic center for reduction reactions, such as reduction of oxygen.

- Doping TiO_2 with anions [10]: Br, F, I, S, N, C. The purpose of this method, is to create intra-band energy levels allowing visible light absorption.
- Promoting TiO_2 with metallic nanoparticles of Au, Pt or Ag, to induce plasmonic effects [11]:
- Reduce the size of TiO_2 crystals [12]
- Coupling TiO_2 with some narrow band-gap semiconductors [13], such as CdS, CdSe, Bi_2S_3, WS_2, RuS_2
- Dispersion of TiO_2 in micro-, or mesoporous materials [14], such as synthesis of Ti-SBA [15], Ti-MCM [16], or Ti-TUD-1 [17].
- Synthesis of oxygen-deficient TiO_2: black TiO_2 [18], or blue TiO_2 [19] have been obtained, among others by hydrogenation under high pressure conditions.

2.1.1. Self-doped titania

As mentioned previously, TiO_2 is the most studied semiconductor metal oxide, and has been extensively used in the field of photcatalysis. The defect structure of TiO_2 has been focused on, since oxygen vacancies are usually the active sites. The presence and structure of defects has been extensively studied both by experimental characterization, and theoretical calculations [20].

Generally, the formation of oxygen vacancies in TiO_2 leads to the creation of unpaired electrons or Ti^{3+}, which results in so-called donor levels in the band diagram of TiO_2 [21].

Scheme 2 shows the effect of Ti^{3+} ions in promoting photocatalytic activity of Ti^{3+}-doped titania (TiO_2) [22]. Ti^{3+} ions induce a sub-level in the band gap, below the energy level of the conduction band of Ti^{4+}. Electrons can be photo-excited from the valence band (VB) to the conduction band (CB) of Ti^{4+} by exposure to UV radiation, or alternatively to the sub-level by irradiation with visible light. Relaxation of electrons from the conduction band (Ti^{4+}) to this sub-level (Ti^{3+}) has also been demonstrated (not shown in Scheme 2).

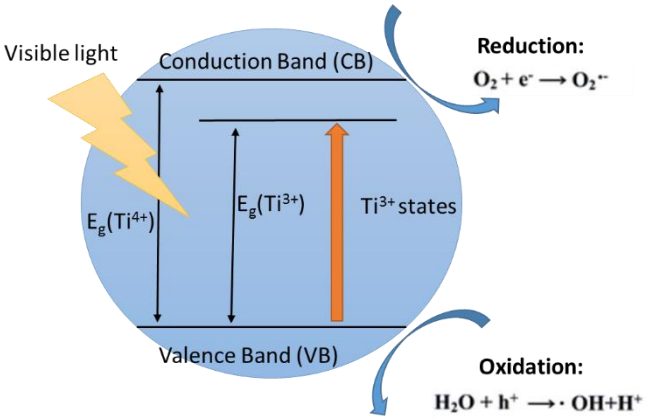

Scheme 2: Scheme of the photo-excitation of Ti^{3+} 'self-doped' titania [22]

2.2. TUD-1 as support material

Porous materials have been commonly used as catalysts or catalyst supports, due to their extraordinarily high surface area [23]. TUD-1 (the abbreviation of Technische Universiteit Delft) is a mesoporous material which was synthesized for the first time in 2001. Shan and co-workers demonstrated that a new templating technique using a low-cost, non-surfactant organic compound in the synthesis procedure, resulted in a 3D silica structure with high surface area (>600 m^2/g) [17].

Subsequently, more than 100 publications appeared, reporting its application and development. Different metals such as Al [24], Au [25], Co [26], Cr [27], Fe [28], Mo [29], Mn [30], or Ti [31] have been incorporated in TUD-1 with variable loadings. The resulting materials have been applied as catalysts in several reactions, with promising performance.

In this thesis, five different samples will be described, i.e. Ti-TUD-1, ZnO-TUD-1, ZnO-Ti-TUD-1, TiO_2-Cr-TUD-1 and Cr-TUD-1 (more details are provided in chapter 7). All samples were synthetized by a one-pot hydrothermal procedure based on the sol-gel technique. The process involved aging, drying, hydrothermal treatment and calcination of a mixture (homogeneous) of TEOS (Ttetraethyl orthosilicate), TEA (triethanolamine), TEAOH (tetraethyl ammonium hydroxide), H_2O and the metal precursors in a molar ratio of 1 SiO_2: 1 TEA: 0.5 TEAOH: 11 H_2O: *x* MO.

2.3. WO_3

Tungsten oxide (WO_3) is another semiconductor showing high performance in photocatalytic conversions. WO_3 has a relatively small bandgap around 2.4 eV which means that it can absorb light in the visible region. WO_3 has been used in many applications such as in electrocatalysis, as a gas sensor, and in photcatalysis. However, pure WO_3 has a lower energy conversion efficiency than TiO_2, because the surface is less effective in transferring photo-excited electrons to surface adsorbed reactants. Similar to the solution discussed for TiO_2, deposition of noble metal nano-particles has been successfully applied to promote electron transfer reactions [32]. In this work we will discuss the effect of surface modification of WO_3 by deposition of Pt nanoparticles in more detail.

3. Plasmon absorption mechanism

As stated previously, besides promotion of electron transfer reactions, several metal nanoparticles can also be excited by exposure to visible light. Absorption of light induces so-called plasmon excitation. Two mechanisms by which plasmon excited states promote photocatalytic activity of semiconductors have been proposed: I) Photo-excitation of Au or Ag nanoparticles leads to an 'electron-hole pair', of which the electron can be transferred to the conduction band of TiO_2, and the hole induces oxidation reactions [33-37]. In 2004, Tatsuma's group proposed this charge transfer mechanism to explain their observation that photon to current conversion efficiency (IPCE) of TiO_2 increased upon functionalization with Au or Ag nanoparticles [37]. Several groups used this mechanism to explain the promotion in visible light induced photocatalytic reactions, such as water splitting [38], decomposition of methyl orange [39], and photo oxidation of organic compounds [40]. II) Plasmon excitation results in an energy field (plasmon resonance energy) which positively influences semiconductor excitation. This phenomenon is mostly observed if overlap exists between plasmon and band-gap absorption [41-43]. Both mechanisms are shown in Figures 1a and 1b, respectively.

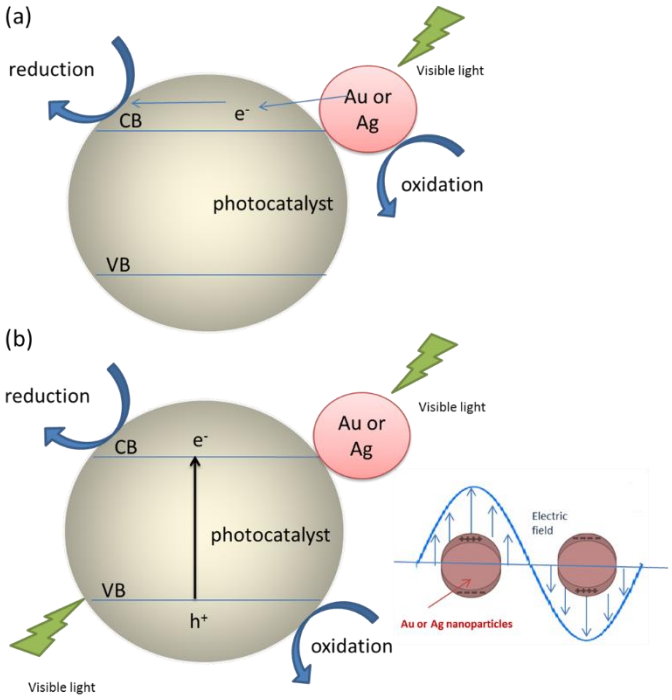

Figure 1: Illustration of the mechanism of 'hot electron transfer' proposed by [37, 38] (a) and the plasmon energy transfer mechanism proposed by [43, 44] (b).

In chapter 4, the activity of Au/TiO_2 will be discussed based on the second model.

4. Photocatalysis applications

The three most significant applications of photocatalysis are solar water splitting [4], purification of air and water [5], and solar light induced conversion of CO_2 and H_2O to useful chemical products [6]. Especially in recent years, research has focused on the usage of photocatalysis for removal of inorganic and organic species from gas or aqueous systems in (industrial) water treatment. Many industrial waste streams can be cleaned by using photo-catalytic processes instead of using traditional methods [1].

Around 20 years ago, products based on photocatalysis by TiO_2 became commercially available in particular in Japan. This industry has developed very fast, and its market reached around 50 billion Japanese yen in Japan in 2004. More than

2000 companies have been identified active in this industry. Table 1 shows some of the most significant applications of TiO_2, based on photocatalysis [45].

Table 1: Selected applications of TiO_2, adapted from [45].

Property	Category	Application
Self-cleaning	Materials for residential and office buildings	Exterior tiles, kitchen and bathroom components, interior furnishings, plastic surfaces, aluminum siding, building stone and curtains, window blinds
	Indoor and outdoor lamps and related systems	Translucent paper for indoor lamp covers, coatings on fluorescent lamps and highway tunnel lamp cover glass
	Materials for roads	Tunnel wall, soundproofed wall, traffic signs and reflectors
	Others	Tent material, spray coatings for cars
Air purification	Indoor air cleaners	Room air cleaner, air conditioner, and interior air cleaner for factories
	Outdoor air purifiers	Concrete for highways, roadways and footpaths, tunnel walls, soundproofed walls, and building walls
Water purification	Drinking water	River water, ground water, lakes and water-storage tanks
	Others	Industrial wastewater, agricultural wastewater, hot spring water, drainage water, pool water, fish feeding tanks,
Self-sterilizing	Hospital	Tiles and coatings to cover the floor, walls and ceiling of operating rooms, silicone rubber for medical catheters, and hospital garments and uniforms
	Others	Public rest rooms, bathrooms, pet-breeding rooms

In this thesis, we focused on three categories of photocatalysis applications.

1) Selective oxidation of reactants to chemical products, with conversion of methylcyclohexane being exemplary.
2) Study of formation of intermediates in ethanol gas phase oxidation to mitigate air pollution.
3) Solar to fuel conversion by studying CO_2 reduction, and more importantly the relevance of the reverse oxidation reactions of the hydrocarbons formed in such process.

5. Thesis outline

In **chapter 1**, a general introduction is presented; i) the principles of photcatalysis are explained, ii) metal oxide photocatalysts used in this thesis are introduced, iii) plasmon absorption mechanisms are illustrated, and iv) the thesis outline is discussed.

In **chapter 2**, several methods are described, which are used in the experimental work of this thesis. First, performing IR spectroscopy with two different accessories, an Attenuated Total Reflection (ATR) or Diffuse Reflectance Infrared Fourier

Transform (DRIFT) accessory, is explained. Further, the photocatalytic reactor systems applying GC (gas chromatography) are illustrated.

Then, in **chapter 3**, we describe, for the first time, the usage of a well-ordered surface Ti^{3+} containing TiO_2 catalyst, which was established to be selective and active in the conversion of methylcyclohexane (MCH) to the formation of methylcyclohexanone, either under illumination with UV (375 nm) or visible light (425 nm). We have characterized the sample by several techniques in detail. The photocatalytic performance of this blue TiO_2 is compared to commercial rutile and P25.

Furthermore, in **chapter 4** we address the effect of Au nanoparticles prepared by deposition–precipitation on the photocatalytic activity of TiO_2 in a liquid phase hydrocarbon oxidation reaction, i.e. again the conversion of methylcyclohexane to methylcyclohexanone. Photocatalytic activity of Au/P25 was evaluated by *in situ* ATR-FTIR spectroscopy. We will demonstrate that of the wavelengths investigated (375, 425 and 525 nm, and combinations thereof), Au nanoparticles were only effective in promoting rates at 375 nm and 425 nm. Furthermore, at these two wavelengths, the performance of the Au nanoparticles will be compared to that of Pt nanoparticles. The plasmonic enhancement of Au will be discussed in detail.

After that, in **chapter 5,** a synergetic effect of Pt nanoparticles and Cr^{6+} in enhancement of the photocatalytic oxidation activity of TiO_2, prepared by a sol gel based procedure, will be addressed. Besides Cr^{6+}, other modifications of the TiO_2 structure investigated include the incorporation of Ag, Cu, V or Pt ions in the TiO_2 crystal structure. The sol-gel synthesized materials were characterized by XRD, BET, TEM, and Raman and UV/Vis spectroscopy.

In **chapter 6**, we report on the effect of Pt addition on the (photo) catalytic activity of WO_3 in selective oxidation of ethanol. Furthermore, the effect of reaction time and presence or absence of UV light on the conversion rates induced by both WO_3 and Pt/WO_3 will be shown. In order to evaluate the gas phase conversion of ethanol, Diffuse Reflectance Infrared spectroscopy (DRIFTS) was used to investigate the formation of surface intermediates in the reactions.

Lastly, in **chapter 7,** the photocatalytic reduction of CO_2 in the presence of H_2O to produce some hydrocarbons such as CH_4 was studied over a series of catalysts consisting of various loading of Ti in TUD-1 (mesoporous silica), either modified by ZnO nanoparticles or isolated Cr-sites. In this chapter, we show three strategies to improve on the current standing of the catalysts on the basis of Ti-sites in

mesoporous silica. We provide new insight in the interaction between ZnO nanoparticles and isolated Ti-sites, as well as on the effects of the simultaneous presence of CrO_x and TiO_x. A schematic outline of the work described in this thesis is presented in Scheme 3.

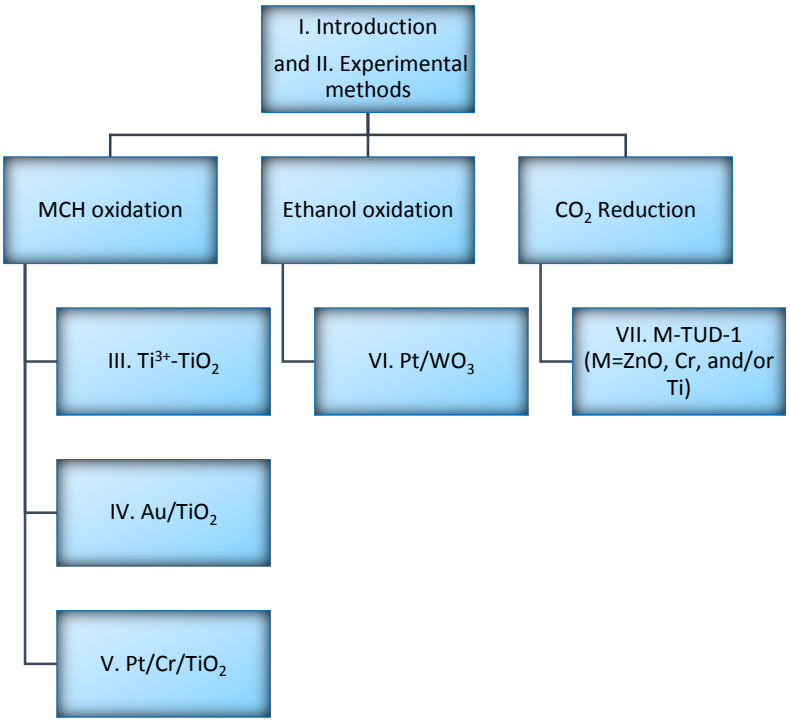

Scheme 3: Schematic outline of the work described in this thesis.

References

[1] A.O. Ibhadon, P. Fitzpatrick, Heterogeneous photocatalysis: Recent advances and applications, Catalysts, 3 (2013) 189-218.

[2] F. He, X.Y. Shen, L.C. Lei, Photochemically enhanced degradation of phenol using heterogeneous Fenton-type catalysts, Journal of Environmental Sciences, 15 (2003) 351-355.

[3] N.D. Shapiro, F.D. Toste, Synthesis and structural characterization of isolable phosphine coinage metal π-complexes, Proceedings of the National Academy of Sciences of the United States of America, 105 (2008) 2779-2782.

[4] M.N. Chong, B. Jin, C.W.K. Chow, C. Saint, Recent developments in photocatalytic water treatment technology: A review, Water Research, 44 (2010) 2997-3027.

[5] J. Zhao, X. Yang, Photocatalytic oxidation for indoor air purification: A literature review, Building and Environment, 38 (2003) 645-654.

[6] G. Palmisano, V. Augugliaro, M. Pagliaro, L. Palmisano, Photocatalysis: A promising route for 21st century organic chemistry, Chemical Communications, (2007) 3425-3437.

[7] M. Ni, M.K.H. Leung, D.Y.C. Leung, K. Sumathy, A review and recent developments in photocatalytic water-splitting using TiO_2 for hydrogen production, Renewable and Sustainable Energy Reviews, 11 (2007) 401-425.

[8] S.N.R. Inturi, T. Boningari, M. Suidan, P.G. Smirniotis, Visible-light-induced photodegradation of gas phase acetonitrile using aerosol-made transition metal (V, Cr, Fe, Co, Mn, Mo, Ni, Cu, Y, Ce, and Zr) doped TiO_2, Applied Catalysis B: Environmental, 144 (2013) 333-342.

[9] J. Choi, H. Park, M.R. Hoffmann, Effects of single metal-ion doping on the visible-light photoreactivity of TiO_2, Journal of Physical Chemistry C, 114 (2010) 783-792.

[10] H. Wang, J.P. Lewis, Second-generation photocatalytic materials: Anion-doped TiO_2, Journal of Physics Condensed Matter, 18 (2006) 421-434.

[11] Z. Zheng, B. Huang, X. Qin, X. Zhang, Y. Dai, M.H. Whangbo, Facile in situ synthesis of visible-light plasmonic photocatalysts M@TiO_2 (M = Au, Pt, Ag) and evaluation of their photocatalytic oxidation of benzene to phenol, Journal of Materials Chemistry, 21 (2011) 9079-9087.

[12] C.B. Almquist, P. Biswas, Role of synthesis method and particle size of nanostructured TiO_2 on its photoactivity, Journal of Catalysis, 212 (2002) 145-156.

[13] W.T. Kim, C.D. Kim, Q.W. Choi, Sub-band-gap photoresponse of TiO_2-x thin-film electrolyte interface, Physical Review B, 30 (1984) 3625-3628.

[14] B. Notari, Synthesis and catalytic properties of titanium containing zeolites, in: Studies in Surface Science and Catalysis, 1988, pp. 413-425.
[15] W.H. Zhang, J. Lu, B. Han, M. Li, J. Xiu, P. Ying, C. Li, Direct synthesis and characterization of titanium-substituted mesoporous molecular sieve SBA-15, Chemistry of Materials, 14 (2002) 3413-3421.
[16] T. Blasco, A. Corma, M.T. Navarro, J.P. Pariente, Synthesis, Characterization, and Catalytic Activity of Ti-MCM-41 Structures, Journal of Catalysis, 156 (1995) 65-74.
[17] Z. Shan, E. Gianotti, J.C. Jansen, J.A. Peters, L. Marchese, T. Maschmeyer, One-step synthesis of a highly active, mesoporous, titanium-containing silica by using bifunctional templating, Chemistry - A European Journal, 7 (2001) 1437-1443.
[18] F. Teng, M. Li, C. Gao, G. Zhang, P. Zhang, Y. Wang, L. Chen, E. Xie, Preparation of black TiO_2 by hydrogen plasma assisted chemical vapor deposition and its photocatalytic activity, Applied Catalysis B: Environmental, 148–149 (2014) 339-343.
[19] A. Teleki, S.E. Pratsinis, Blue nano titania made in diffusion flames, Physical Chemistry Chemical Physics, 11 (2009) 3742-3747.
[20] X. Pan, M.-Q. Yang, X. Fu, N. Zhang, Y.-J. Xu, Defective TiO_2 with oxygen vacancies: synthesis, properties and photocatalytic applications, Nanoscale, 5 (2013) 3601-3614.
[21] M.K. Nowotny, L.R. Sheppard, T. Bak, J. Nowotny, Defect Chemistry of Titanium Dioxide. Application of Defect Engineering in Processing of TiO_2-Based Photocatalysts†, The Journal of Physical Chemistry C, 112 (2008) 5275-5300.
[22] J. Huo, Y. Hu, H. Jiang, C. Li, In situ surface hydrogenation synthesis of Ti^{3+} self-doped TiO_2 with enhanced visible light photoactivity, Nanoscale, 6 (2014) 9078-9084.
[23] H. Maneesuwan, S. Tantisriyanurak, T. Chaisuwan, S. Wongkasemjit, Impressivephenol hydroxylation activity using Fe–Ti-TUD-1 synthesized from silatrane via sol–gel process, Applied Catalysis A: General, 504 (2015) 448-456.
[24] Z.X. Zhang, P. Bai, B. Xu, Z.F. Yan, Synthesis of mesoporous alumina TUD-1 with high thermostability, Journal of Porous Materials, 13 (2006) 245-250.
[25] M.S. Hamdy, Au-TUD-1: A new catalyst for aerobic oxidation of cyclohexene, Microporous and Mesoporous Materials, 220 (2016) 81-87.
[26] M.S. Hamdy, A. Ramanathan, T. Maschmeyer, U. Hanefeld, J.C. Jansen, Co-TUD-1: A ketone-selective catalyst for cyclohexane oxidation, Chemistry - A European Journal, 12 (2006) 1782-1789.

[27] M.S. Hamdy, G. Mul, The effect of active sites' nature on the photo-catalytic performance of Cr-TUD-1 in the oxidation of C1-C3 hydrocarbons, Applied Catalysis B: Environmental, 174-175 (2015) 413-420.
[28] M.S. Hamdy, G. Mul, J.C. Jansen, A. Ebaid, Z. Shan, A.R. Overweg, T. Maschmeyer, Synthesis, characterization, and unique catalytic performance of the mesoporous material Fe-TUD-1 in Friedel-Crafts benzylation of benzene, Catalysis Today, 100 (2005) 255-260.
[29] M.S. Hamdy, G. Mul, Synthesis, characterization and catalytic performance of Mo-TUD-1 catalysts in epoxidation of cyclohexene, Catalysis Science and Technology, 2 (2012) 1894-1900.
[30] G. Imran, M.P. Pachamuthu, R. Maheswari, A. Ramanathan, S.J. Sardhar Basha, Catalytic activity of MnTUD-1 for liquid phase oxidation of ethylbenzene with tert-butyl hydroperoxide, Journal of Porous Materials, 19 (2012) 677-682.
[31] M.S. Hamdy, O. Berg, J.C. Jansen, T. Maschmeyer, J.A. Moulijn, G. Mul, TiO<inf>2</inf> nanoparticles in mesoporous tud-1: synthesis, characterization and photocatalytic performance in propane oxidation, Chem. Eur. J., 12 (2006) 620-628.
[32] Z.-G. Zhao, M. Miyauchi, Nanoporous-Walled Tungsten Oxide Nanotubes as Highly Active Visible-Light-Driven Photocatalysts, Angewandte Chemie International Edition, 47 (2008) 7051-7055.
[33] K. Adachi, K. Ohta, T. Mizuno, Photocatalytic reduction of carbon-dioxide to hydrocarbon using copper-loaded titanium-dioxide, Solar Energy, 53 (1994) 187-190.
[34] Y. Tian, T. Tatsuma, Mechanisms and applications of plasmon-induced charge separation at TiO_2 films loaded with gold nanoparticles, Journal of the American Chemical Society, 127 (2005) 7632-7637.
[35] M.S. Devadas, K. Kwak, J.-W. Park, J.-H. Choi, C.-H. Jun, E. Sinn, G. Ramakrishna, D. Lee, Directional Electron Transfer in Chromophore-Labeled Quantum-Sized Au-25 Clusters: Au-25 as an Electron Donor, Journal of Physical Chemistry Letters, 1 (2010) 1497-1503.
[36] W.-T. Chen, Y.-J. Hsu, P.V. Kamat, Realizing Visible Photoactivity of Metal Nanoparticles: Excited-State Behavior and Electron-Transfer Properties of Silver (Ag-8) Clusters, Journal of Physical Chemistry Letters, 3 (2012) 2493-2499.
[37] Y. Tian, T. Tatsuma, Plasmon-induced photoelectrochemistry at metal nanoparticles supported on nanoporous TiO_2, Chemical Communications, (2004) 1810-1811.
[38] C. Gomes Silva, R. Juarez, T. Marino, R. Molinari, H. Garcia, Influence of Excitation Wavelength (UV or Visible Light) on the Photocatalytic Activity of

Titania Containing Gold Nanoparticles for the Generation of Hydrogen or Oxygen from Water, Journal of the American Chemical Society, 133 (2011) 595-602.
[39] J. Yu, G. Dai, B. Huang, Fabrication and Characterization of Visible-Light-Driven Plasmonic Photocatalyst Ag/AgCl/TiO_2 TiO_2 Nanotube Arrays, Journal of Physical Chemistry C, 113 (2009) 16394-16401.
[40] J. Tang, Interaction between Noble Metal Nanoparticles and Light for Contaminant Decomposition, Chemsuschem, 3 (2010) 800-801.
[41] S.L. Zou, G.C. Schatz, Silver nanoparticle array structures that produce giant enhancements in electromagnetic fields, Chemical Physics Letters, 403 (2005) 62-67.
[42] F. Le, D.W. Brandl, Y.A. Urzhumov, H. Wang, J. Kundu, N.J. Halas, J. Aizpurua, P. Nordlander, Metallic nanoparticle arrays: A common substrate for both surface-enhanced Raman scattering and surface-enhanced infrared absorption, Acs Nano, 2 (2008) 707-718.
[43] S. Linic, P. Christopher, D.B. Ingram, Plasmonic-metal nanostructures for efficient conversion of solar to chemical energy, Nature Materials, 10 (2011) 911-921.
[44] D.B. Ingram, P. Christopher, J.L. Bauer, S. Linic, Predictive Model for the Design of Plasmonic Metal/Semiconductor Composite Photocatalysts, Acs Catalysis, 1 (2011) 1441-1447.
[45] A. Fujishima, X. Zhang, D.A. Tryk, Heterogeneous photocatalysis: From water photolysis to applications in environmental cleanup, International Journal of Hydrogen Energy, 32 (2007) 2664-2672.

Chapter 2

Experimental methods

1. Photocatalytic activity testing

Different techniques used to evaluate the photocatalytic performance of the prepared catalysts will be introduced. First, the analysis of surface chemistry by IR spectroscopy will be explained. Second, a top illuminated batch reactor connected to a gas chromatograph (GC) will be described, and finally the lay-out and use of a home-made multi-cell reactor for screening of photocatalytic activity.

1.1. IR spectroscopy

Infrared absorption (IR) spectroscopy is one of the oldest (more than 50 years) techniques for identifying both inorganic and organic chemicals. In principle, different kinds of groups of atoms (O-H, C-H, N-H, etc…) absorb infrared radiation at different characteristic wavenumbers ((cm^{-1}), the wavenumber being the reciprocal of the wavelength ($1/\lambda$)). Table 1 shows an overview in which spectral region specific molecular entities can be found [4].

Infrared absorption is a powerful tool to study solids, liquids and gas samples. These days, in situ IR spectroscopy is often employed to study chemistry occurring on surfaces of solids, such as metal oxide semiconductors [1].

In the following, two methods for in situ infrared analysis will be explained, i.e. Attenuated Total Reflection Fourier-transform infrared (ATR-FTIR) spectroscopy, and Diffuse Reflectance Infrared Fourier Transformed (DRIFT) spectroscopy.

Table 1: Correlation between infrared absorption and specific molecular groups adapted from [4]

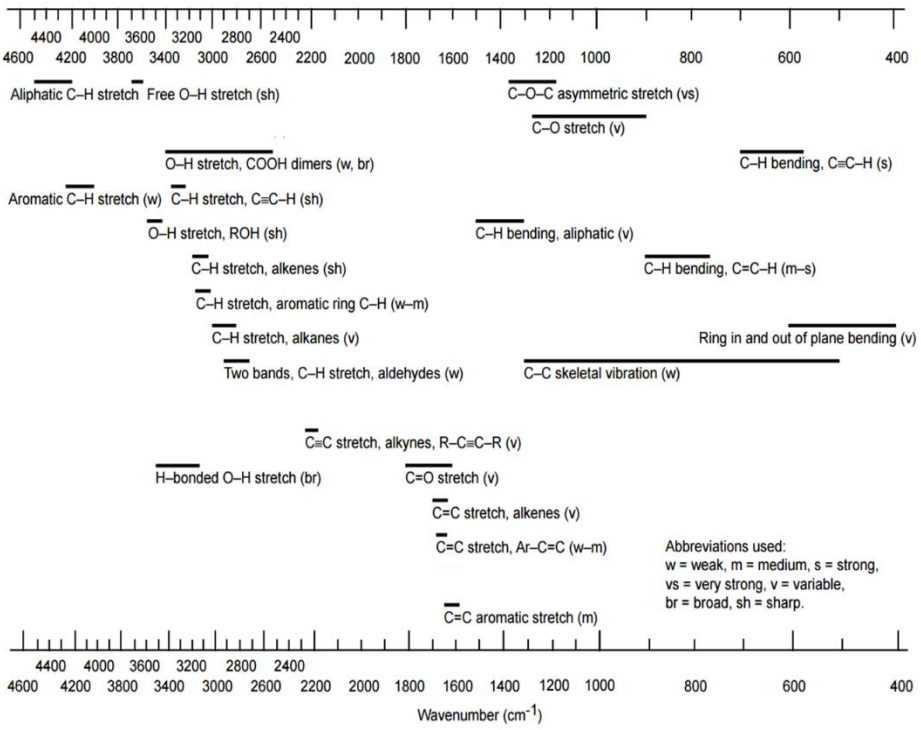

1.1.1.In Situ ATR-FTIR spectroscopy

A Harrick Scientific ATR−setup (included in the compartment of a Bruker Vertex 70 spectrometer) was used to study the solid-liquid interface during photocatalysis in this research. For the preparation of a thin film layer of a catalyst on a ZnSe ATR crystal, a mQ water suspension including a catalyst concentration of 2.92 g L^{-1} was treated for 30 min in a 35 kHz Elmasonic ultrasonic bath. 2 ml of the prepared suspension was drop casted on the ATR crystal, and dried in a dessicator at room temperature in vacuum and dark conditions overnight. Before study photocatalytic activity, 20 mL of Methyl CycloHexane (MCH) was saturated by purging with dry air at 8 mL/min for 30 min. Afterwards, O_2 saturated MCH was carefully deposited on the catalyst thin film, and then enclosed by a top plate containing a quartz window. Before illumination, a spectrum of adsorbed MCH on the catalyst coating

was recorded, and used as background spectrum for during activity measurements. Every 1 min. a spectrum was measured from 700-4000 cm^{-1}, averaged from 64 scans with a resolution of 4 cm^{-1}. To study photocatalytic activity, an assembly of 7 LEDs (375 nm or 425 nm) was used as light source. The ATR–FTIR setup is schematically shown in Figure 1.

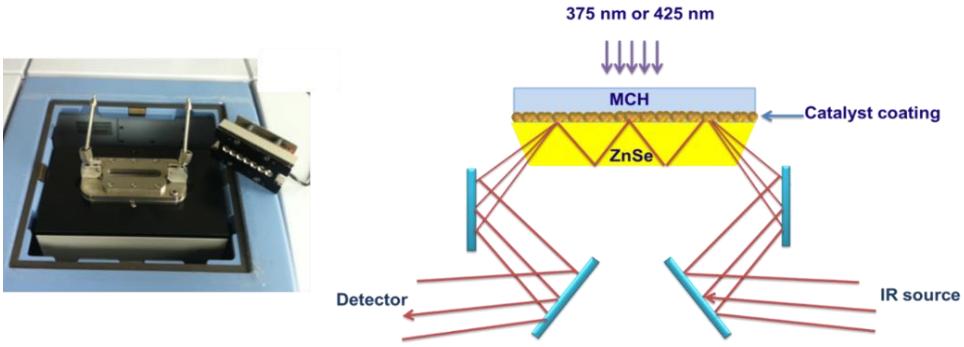

Figure 1: Image and schematic outline of the ATR-FTIR cell used, including the LED assembly of 7 LEDs, allowing emission at wavelengths of 375 nm or 425 nm.

1.1.2.In situ DRIFT spectroscopy

Photocatalytic oxidation of gas-phase compounds was also analyzed by infrared (IR) spectroscopy using the Bruker Vertex 70 spectrometer equipped with a liquid nitrogen cooled MCT detector. A Harrick Praying Mantis diffuse reflectance accessory containing a three-window dome was inserted in the sample compartment of the spectrometer. A quartz window allowed the illumination of the catalyst with UV/Vis light, while two ZnSe or CaF_2 windows provided an optical path for infrared analysis. Prior to the illumination experiments, 30 mg of a catalyst was introduced in the sample cup of the accessory. After enclosure of the catalyst, a flow of 20 mL/min of dry air saturated with a gas compound, such as ethanol was introduced. After exposure of the catalyst to this flow for 10 min, the lines to the cell were closed. A spectrum was recorded of this state of the catalyst after 1 min, to serve as a background for the series recorded during dark reaction or under illumination. In situ DRIFT spectra were recorded every 1 min. from 700-4000 cm^{-1}, averaged from 64 scans with a resolution of 4 cm^{-1}. As illumination source, a 365 nm or 425 nm LED was used with a maximum light intensity of 8 mW/cm^2 at the catalyst surface. For some other experiments, a 100 Watt Hg lamp, λ between 250 to 600 nm) was used

as irradiation source. Figure 2 shows the schematic outline of the DRIFT experimental set-up.

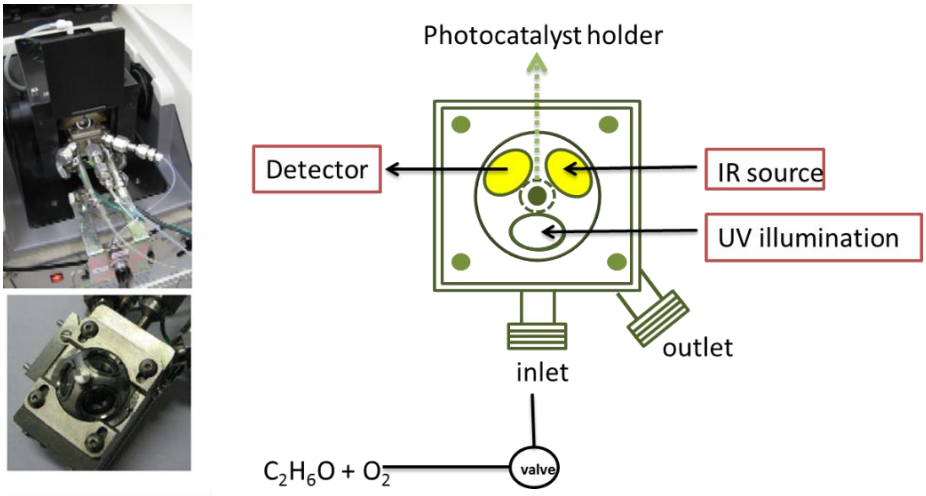

Figure 2: Image and schematic outline of the DRIFT cell used.

1.2. The photocatalytic reactor system

Samples prepared on glass plates were placed at the bottom of a batch reactor (2ml) equipped with a quartz window. As illumination source, a 365 nm LED (Roithner Laser Technik, Austria, APG2C1-375-S) was used with a maximum possible light intensity of 8 mW/cm^2 at the catalyst coating. After a predefined mixture, prepared by ethanol evaporation, was fed to the reactor at 30 ml/min, the reactor was operated in batch mode. Two valves were used to close the reactor during illumination. After various time intervals of illumination (0 to 50 min), the entire gas composition present in the reactor was purged by a He flow onto a Varian CP7584 column coupled to a Methanizer–FID combination for detection of acetaldehyde and CO_2, both present in an Agilent 7820 GC system. For analysis of ethanol oxidation, typically an ethanol feed concentration of 1.7 vol.% was used [2].

Figure 3: Image of the top illuminated batch reactor used.

1.3. Multi-cell reactor

The photocatalytic reduction of CO_2 with H_2O vapor was assessed in a homemade multi-cell photocatalytic setup. The setup contains 12 equally sized cylinder-shaped reactors (volume 50 mL), which are connected to a sample valve for selection of the reactor to be analyzed. The functional light source is a 120W high-pressure mercury lamp with a spectrum ranging from 280 to 650 nm. The reaction was performed using a ratio of 0.5 of CO_2 (38 µmol) over H_2O (76 µmol). All reactors were operated in batch mode and illuminated for 8 h. The production of hydrocarbons was determined by use of a compact gas chromatograph equipped with Molsieve 5A and capillary Porabond Q columns connected to a TCD detector (used for separation of H_2, O_2, N_2, CO and CH_4). A second Porabond Q column linked to an FID detector was used for separation and detection of C_1-C_4 alkanes and alkenes. Concentrations were analyzed with an accuracy of ±0.5 ppm. In evaluating the reaction, 100 mg of the catalyst was distributed evenly at the bottom of the reactor to create a uniform layer with a thickness of approximately 1-2 mm. The reactors were evacuated down to 3 mbar and then the CO_2/He mixture saturated with water vapor was introduced. The evacuation/filling cycles were repeated three times, followed by initiation of the reaction by illumination [3].

References

[1] J. Ryczkowski, IR spectroscopy in catalysis, Catalysis Today, 68 (2001) 263-381.

[2] B.D. Fraters, R. Amrollahi, G. Mul, How Pt nanoparticles affect TiO2-induced gas-phase photocatalytic oxidation reactions, Journal of Catalysis, 324 (2015) 119-126.

[3] M.S. Hamdy, R. Amrollahi, I. Sinev, B. Mei, G. Mul, Strategies to design efficient silica-supported photocatalysts for reduction of CO_2, Journal of the American Chemical Society, 136 (2014) 594-597.

[4] B. FAUST, Modern Chemical Techniques : An Essential Reference for Students and Teachers, Royal Society of Chemistry, 1997.

Chapter 3

Surface Ti^{3+} containing (blue) titania: A unique photocatalyst with high activity and selectivity in visible light stimulated selective oxidation

A one step synthesis procedure at elevated temperature was used to prepare Ti^{3+} containing blue titania. The prepared material was characterized by X-ray powder diffraction (XRD), UV-Vis and Raman spectroscopy, X-ray photoelectron spectroscopy (XPS), as well as by N_2 adsorption and desorption measurements. The blue titania sample was found to be crystalline, with a surface area of 22 m^2/g. Its phase composition consists of 85% rutile and 15% anatase with a multitude of defect surface V_O-Ti^{3+} sites. The blue titania showed an absorption red-shifted as compared to P25, with a calculated bandgap of 2.93 eV. The photocatalytic performance of the blue titania was evaluated in the liquid phase selective photo-oxidation of methylcyclohexane (MCH) by illumination at 375 ± 10 nm (UV), and 425 ± 10 nm (visible light), respectively. The activity was monitored by ATR-FTIR. A high activity was observed for blue TiO_2, remarkably of equal magnitude at both investigated wavelengths. Not only the activity of the blue titania surpassed the activity of other commercial titania catalysts (rutile and P25), in particular at 425 nm, but also the obtained selectivity towards ketones.

Keywords: Self-doped TiO_2, blue titania, Ti^{3+}, photocatalysis, selective photooxidation

This chapter is based on: M. S. Hamdy, R. Amrollahi, G. Mul; Title; "Surface Ti^{3+} Containing (blue) Titania: A Unique Photocatalyst with High Activity and Selectivity in Visible Light-Stimulated Selective Oxidation'', ACS Catalysis, 2012, 2 (12), pp 2641-2647.

1. Introduction

Titanium dioxide (TiO_2) has been studied extensively in the field of photocatalysis. It attracts interest due to its nontoxicity, low cost, chemical inertness and availability. It has great ability to decompose undesired compounds present in air/water, and is of interest for splitting water into oxygen and hydrogen. However, due to its wide bandgap (i.e. 3.05 eV for Rutile and 3.2 eV for Anatase) TiO_2 exhibits high activity only under ultraviolet (UV) exposure, which limits its applicability in practice. Hence, the use of photocatalysis as a synthetic tool is not economically feasible despite the success of photocatalysis in organic conversions into industrially relevant compounds or intermediates.

Several studies have been reported in which the absorption of TiO_2 was shifted towards the visible light region by doping titana with metal (e.g. V [1], Cr [2], Fe[3], etc) or non-metal ions (e.g. N [4]), or by dye sensitization [5]. Another approach was the creation of surface defects in TiO_2 crystals. Surface defects in TiO_2 crystals can be introduced by changing the titanium/oxygen ratio (i.e. creating oxygen vacancies, or titanium vacancies) or by incorporating higher- and lower-valence ions to form donors and acceptors, respectively.

Recently, reduced titania (TiO_{2-x}) which contains oxygen vacancies (V_O)-Ti^{3+} has been reported to exhibit significant photocatalytic activity in the visible light region [6]. Earlier work of Liu et al [7] demonstrated that the activity of stoichiometric TiO_2 surfaces in decomposition of water contaminants (sulfosalicylic acid and phenol) differs markedly from surfaces containing Ti^{3+} prepared by hydrogen treatment, although visible light activity was not specifically addressed. It has also been discussed [8] that the quantity of surface defects associated with Ti^{3+} increases with increasing crystallite size. This enhances the activity in photocatalytic combustion of ethylene in air, although again visible light activity was not specifically discussed. Several techniques were reported to produce reduced TiO_2 containing Ti^{3+} such as thermal treatment under vacuum [9], thermal annealing to high temperatures(> 500 K) [10], thermal treatment in reducing conditions, using e.g. C [11] and H_2 [7], laser treatment [12], or bombardment with high-energy particles (e.g. neutrons [13], or γ-rays [14]). Recently, a novel one-step synthesis of self-doped Ti^{3+} was reported [15]. The as prepared blue material was found effective in water splitting when used with a co-catalyst (Pt).
Here we report for the first time the use of an unpromoted, surface Ti^{3+} containing TiO_2 composition in the conversion of methyl cyclohexane (MCH) to form

methylcyclohexanone, as a model reaction for many interesting conversions in synthetic chemistry. Methylcyclohexane has a relatively low vapour pressure, which simplifies spectroscopic analysis of the reaction. Furthermore, methylcyclohexanone is used i) as a solvent in making lacquers, varnishes, and plastics; ii) in the leather industry; and iii) as a rust remover. The photocatalytic study was carried out under the illumination of UV (375 nm), or visible light (425 nm). Remarkably, the activity and selectivity was very similar at both wavelengths, and significantly higher as compared to commercial rutile and P25. We have characterized the prepared sample by several techniques in detail. We conclude that surface Ti^{3+} sites provide the unique activity and selectivity in the target reactions at relatively high wavelengths, and that the phase composition has a minor effect.

2. Experimental

MCH (99%) and rutile (nanopowder, 99.5%) were obtained from Sigma-Aldrich, and P-25 was obtained from Evonik, Germany. MCH, rutile, and P-25 were used as received without any further modification. Reduced (blue) titania was prepared as reported by Feng et al. [15], a solution of 10 g ethanol (99.5, Sigma Aldrich), 2.5 g of hydrochloric acid (37%, Aldrich), 2 g of titanium (IV) isopropoxide (98%, Sigma) and 1.8 g of 2-ethylimidazole (98%, Sigma) was introduced in a porcelain crucible to a preheated oven at 773K. The evaporation and combustion of the solution in air for a period of 5h produced a blueish, greyish powder.

The crystal structure of the material was determined in air by powder X-ray diffraction (XRD) using a Philips PW2050 (X'Pert-APD) diffractometer with Cu K_α radiation ($\lambda = 0.15406$ nm). Data were collected varying 2θ between 20° and 80° with a step size of 0.005° and a step time of 1 s. The anatase to rutile ratio was calculated from the following equation:

$$X_R = 1.26\ I_R/(I_A+1.26\ I_R)$$

X_R is the rutile fraction and I_R and I_A are the strongest intensities of the rutile (110) and anatase (101) diffraction angles, respectively. Nitrogen physisorption measurements were carried out at −196°C with a Micromeritics Tristar system (ASAP 2400) to determine the textural properties. Prior to the adsorption measurements the samples were degassed at 300 °C and 10^{-3} Pa for 24 h. The specific surface areas were calculated according to the Brunauer–Emmet–Teller (BET) method. Raman spectra were taken with a Bruker Senterra Raman

Spectrometer equipped with a cooled CCD detector (-60°C). A green (λ = 532 nm) laser with intensity of 2 mW was used for excitation. Spectra were acquired at a resolution of 9-15 cm^{-1} and 10 scans were accumulated for each spectrum. X-ray photoelectron spectroscopy (XPS) was carried out using a Quantera SXM spectrometer made by Physical Electronics. The Al K_α (1486.6 eV) source was operated at a 25 W emission power and at 15 kV acceleration voltage. Diffuse reflectance UV-Vis spectra were collected at ambient temperature on an EVOLUTION 600 (ThermoScientific) spectrometer, using $BaSO_4$ as reference. Spectra were recorded in the wavelength range of 200–600 nm. The bandgap is calculated by the following equation:

$$E = h*C/\lambda$$

Where h is the Plank constant (6.626 x 10^{-34} Joules sec), C is the speed of light (3.0 x 10^8 meter/sec) and λ is the cut off wavelength.

The photocatalytic study was determined using an ATR-FTIR setup [16]. The setup consists of a Harrick Horizon multiple internal reflections accessory, containing a ZnSe crystal, enclosed by a top plate containing a quartz window, such that a 4 mL flow-through cell is obtained. The Fourier transform infrared measurements were performed on a Bruker Vertex spectrometer equipped with a nitrogen cooled MCT detector. An assembly of 7 LEDs (Roithner Lasertechnik) fitting on the top of the cell provided for illumination of the reaction mixture through the quartz window. Two different LED types were applied with two different wavelengths; 375 ± 10 nm and 425 nm ± 10 nm. The light intensity of the LED's was fine tuned to be equal at 1.5 mW/cm^2. Catalyst layers were prepared on the ATR crystal (ZnSe) as follows. A suspension of the photocatalyst (0.146 g/50mL) in water was ultrasonicated for 30 min in a 35 kHz Elmasonic ultrasonic bath; 2 mL of this suspension was spread on the ZnSe crystal and dried in vacuum overnight. Methylcyclohexane was saturated with O_2 by bubbling dry air at 7.65 mL/min flow through the liquid. 1 mL of the oxygen-saturated methylcyclohexane was introduced to the catalyst layer on the ZnSe crystal. The cell was carefully closed to prevent evaporation. Background spectra were collected before illumination. Start of illumination was considered to be zero time of reaction, after which spectra were recorded at fixed time intervals from 4000-700 cm^{-1} by collecting 64 scans with a resolution of 4 cm^{-1}.

3. Results

The textural structure of the reduced titania sample was examined by nitrogen physisorption. The nitrogen adsorption–desorption isotherms and Barret–Joyner–Halenda (BJH) pore size distribution curves of the prepared sample and a commercial rutile sample are compared in Figure 1. The reduced titania showed a type IV adsorption–desorption isotherm with a H_2 hysteresis loop (which appears at $0.65 < P/Po < 1$), which is typical for materials containing mesoporisity. The presence of mesopores is most likely the result of the aggregation of primary nanoparticles. The BET surface area derived from the isotherm is 22 m^2/g. The corresponding BJH pore size distribution of the sample is centered at 9 nm.

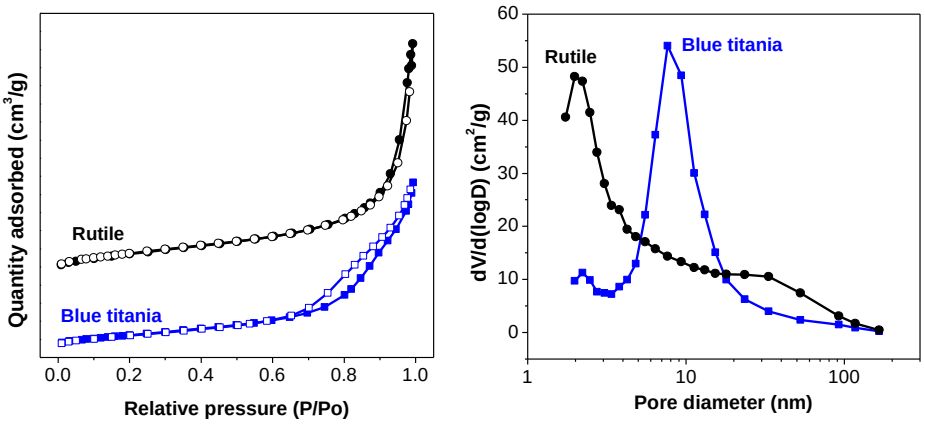

Figure 1. Left panel: N_2 adsorption/desorption isotherms of blue titania compared to the isotherms of a commercial rutile sample. Right panel: the corresponding pore diameter distribution

The XRD pattern of the blue titania is shown in Figure 2-A. The pattern exhibits strong diffraction lines at 27°, 36° and 55° indicating the presence of TiO_2 in the rutile phase. On the other hand, the pattern exhibits strong diffraction peaks at 25° and 48° indicating the presence of TiO_2 in the anatase phase. XRD thus indicates the co-existence of rutile and anatase phases in the prepared sample. The calculated anatase:rutile ratio in the reduced titania sample is 15%:85%.

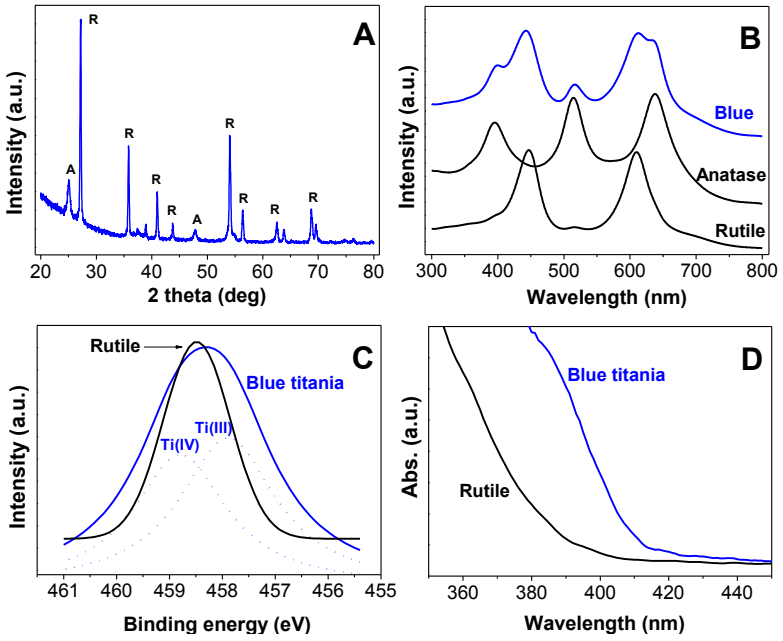

Figure 2. A: The XRD pattern of the blue titania sample. (R) is referring to the characteristic peaks of the rutile phase while (A) is referring to anatase. B: *In-situ* Raman spectrum of the blue titania sample compared to anatase and rutile samples. C: The XPS Ti2p 458.1 eV band of blue titania as compared to that of a rutile sample (solid line), the dotted lines are the deconvoluted signals of the blue titania band. D: The UV-Vis spectrum of the blue titania as compared to the rutile sample.

The Raman spectrum of the reduced titana, compared to the spectra of rutile and anatase, is presented in Figure 2-B. The presence of the bands at 391, 443, 511, 605, and 633 cm^{-1} confirms the presence of rutile and anatase phases in the reduced titania. XPS analysis was carried out to investigate the surface state of titanium. The standard binding energy of $Ti2p_{3/2}$ in a reference rutile sample shows a narrow band located around 459.3 eV assigned to Ti^{4+} (Figure 2-C). However, a broad intensity profile, centered at 458.1 eV, was observed for the blue titania sample. The broadness of the peak in the reduced titania sample indicates multiple oxidation states are present on the surface. After deconvolution, a signal at 457.7 eV can be attributed to the presence of Ti^{3+} [17], [18]. The relative content of Ti^{3+} in the surface of reduced TiO_2 was obtained by comparing the XPS peak areas and thus roughly estimated to be 50%. The UV-Vis spectrum of reduced titania is compared to the spectrum of rutile in Figure 2-D. The spectrum of the reduced titania shows a red shift as compared to

neat rutile. The calculated bandgap of the reduced titania is 2.93 eV which is smaller than that of rutile (3.08 eV) [19].

To conclude, the prepared sample is a mesoporous titania with blueish grey colour. The surface area of the sample is 22 cm^2/g and the pore diameter is 9 nm. The sample consists of 85% rutile and 15% anatase with the presence of surface Ti^{3+} in an estimated amount of 50% of all surface sites. The sample showed a red-shifted UV/Vis absorption profile, with a calculated bandgap of 2.93 eV.

The spectrum of MCH, and the spectra of the expected products are presented in Figure 4. The spectra of the photocatalyst surface after being exposed to MCH and illumination at 425 nm for 100 minutes, are presented in Figure 4, left panel.

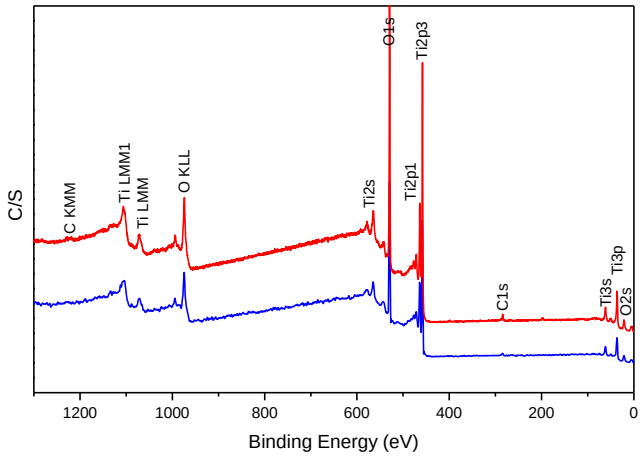

Figure 3. The XPS survey of blue titania (blue) compared to Rutile (red).

In general, MCH exhibits bands around 2919, 2852, 1448, 1375, 1365, 1263 and 1247 cm^{-1}. The bands at high wavenumbers (i.e. 2919 and 2852 cm^{-1}) correspond to the symmetric and anti-symmetric (C–H) stretching modes. The bands at 1448, 1375 and 1375 cm^{-1} are assigned to C–H bending modes of the methyl group. The band appearing at 1263 cm^{-1} can be assigned to the stretching vibration of the C–C bond.

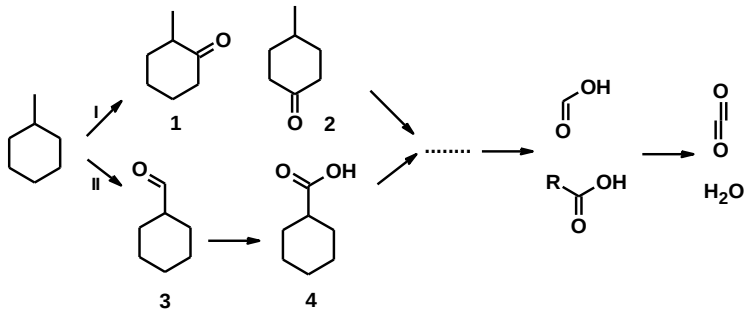

Scheme 1. The predicted pathways of the photocatalytic oxidation of MCH in the liquid phase.

Different reference experiments were carried out to prove the synergy between light and the catalyst to promote the reaction. No photolytic products were observed after 30 minutes of illuminating MCH under the two applied wavelengths. On the other hand, TiO_2 (blue and commercial) did not induce MCH oxidation in the absence of light. Furthermore, as reported by our group earlier [20], the synthesized catalyst might contain very small amounts of remaining carbon from the synthesis step, and hence might contribute to spectral changes. Therefore, a reference experiment was carried out in which only the coated layer of the catalyst was subjected to light for 2h and the products formed monitored by FTIR. Only minor changes in spectral intensity were observed, which is in agreement with the small amount of carbon detected by XPS. These observations indicate that the surface of the catalyst is relatively clean.

After illuminating MCH interacting with the blue titania sample, a broad range of infrared absorptions develop in time between 1800 and 1000 cm^{-1}, an indication for the formation of several products. The photocatalytic oxidation of MCH can take place *via* two possible routes (scheme 1); the first is the oxidation of the cyclic ring (I) with the formation of *o*-methylcyclohexanone (**1**) and/or *p*-methyl cyclohexanone (**2**) as primary products. Over-oxidation can take place opening the ring and forming several carboxylate species as reported for cyclohexane [16]. The second oxidation route is the oxidation of the methyl group (II), with the formation of formylcyclohexane (**3**) as a primary product. Subsequent oxidation might form cyclohexanecarboxylic acid (**4**). The spectra of **1** and **2** show intensive bands at 1708 and 1714 cm^{-1} respectively (Figure 4-Right panel). While the spectra of **3** and **4** exhibit a dominant band at 1724 and 1706 cm^{-1} respectively. The bands at 1596, 1579 and 1564 cm^{-1} can be assigned to the ν_{as} (COO) mode of acetate and formate species

and the band at 1403 cm^{-1} could correspond to the ν (C=O) mode of carbonate. Lastly, the bands at 1776, 1752 and 1569 cm^{-1} could be assigned to formic acid. The band assignments are summarized in Table 1.

Table 1. The peak assignments as adapted from [21] and references therein.

Peak(s) location (cm^{-1})	**Assignment**
1453, 1380 and 1363 cm^{-1}	methyl group
1461 cm^{-1}	(C–H) mode of CH_2 groups.
1597 and 1563 cm^{-1}	acetate and formate
1689 cm^{-1}	(C=O) mode of a carbonyl compound
1720–1740 cm^{-1}	aldehyde (formylcyclohexane) and/or a ketone (methylcyclohexanone)
1596, 1570, 1540 and 1521 cm^{-1}	carboxylate (e.g. acetates)
1751 cm^{-1}	formic acid
1692 cm^{-1}	methylcyclohexanone
1702 cm^{-1}	ketone, weakly adsorbed
1452 cm^{-1}	ν_s (COO) mode of formic acid
1567, 1369 cm^{-1}	ν_{as} (COO) and ν_s (COO) modes of formate
1452 cm^{-1}	ν_s (COO) mode of formic acid
1735 cm^{-1}	formylcyclohexane

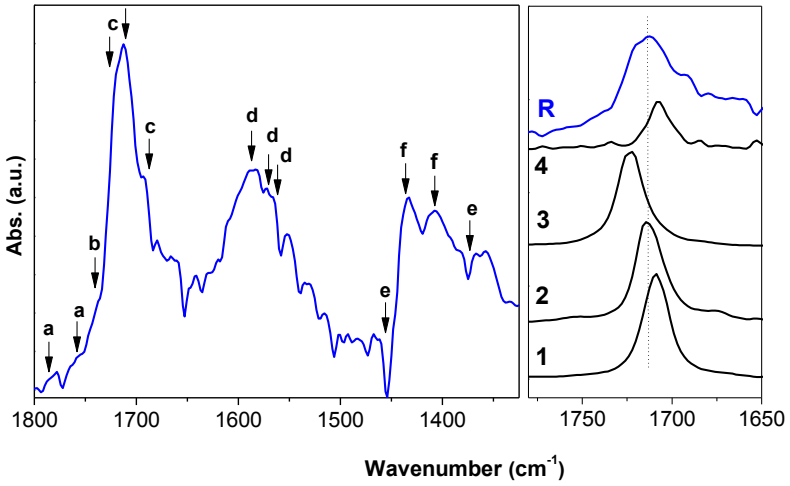

Figure 4. Left panel: The FTIR spectrum of MCH after 200 minutes of illumination at 425 nm, a) formic acid, b) formylcyclohexane, c) methylcyclohexanone, adsorbed (1712 cm^{-1}) and dissolved (1685 cm^{-1}) d) acetate or formate, e) MCH and carbonate species. Right panel: The spectrum of MCH after reaction (R) as compared to reference spectra of **1**, **2**, **3**, and **4**.

To identify the products of the photocatalytic oxidation of MCH, a comparison between the band locations in the area between 1650 and 1800 cm^{-1} with the reference spectra was carried out (Figure 4, right panel). The comparison suggests the formation of **1** and **2** as major primary products with a minor formation of **3** (Figure 4). **4** was difficult to identify because of the interference with **1** band**,** however since **4** is the over-oxidation product of **3,** and **3** is minor, we propose route I as the main route for this reaction. Unfortunately, this result is in disagreement with the results reported by Alonso et al. [22] in which **3** was reported to be the main product. However, Mul et al. [16] reported a difference in the peak location between dissolved ketone (1685 cm^{-1}) and adsorbed ketone (1712 cm^{-1}), which might complicate the interpretation.

The IR spectra of MCH after 200 minutes of reaction over blue titania under 375 and 425 nm illumination are compared to those of rutile and P-25 in Figure 5. It is clear that wavelength has an effect on performance of Degussa P25 and even more so on the rutile sample; the blue titania sample is photocatalytically more active at both wavelengths, despite the higher surface area of the commercial samples (table 2).

Remarkably, the photocatalytic activity of blue TiO_2 is very similar at both wavelengths of illumination. Moreover, the product distribution seems to be almost the same, which is an indication that the reaction follows the same mechanism for the two different wavelengths. There is a significant difference in the product distribution between the blue titania sample and both the P-25 and rutile catalysts (Figure 5). The ketone bands are more intense than the bands of carboxylates in the case of blue titania, while carboxylate contributions dominate in the spectra of P-25 and rutile, respectively.

Table 2. The textural properties of blue titania compared with commercial rutile and Degussa P25

Sample	Textural properties		
	BET surface area (m^2/g)	Pore volume (cm^3/g)	Pore size (nm)
Blue titania	22	0.11	9
Rutile	31	0.09	2
P25	50 ± 15	0.25	17

Table 3. The amount of ketone (methyl cyclohexanone) in μmole produced after 100 minutes under different illumination sources.

Sample	Amount of ketone (μmole)	
	375 nm	425 nm
Blue titania	6.2	5.9
P25	2.7	2.1
Rutile	0.8	0.7

An indication of the quantity of ketones produced after reaction for 100 min under the two applied wavelengths is presented in Table3. The amounts were determined

on the basis of calibration of the band intensity in the range of 1650−1750 cm^{-1}, as a function of concentration. The amounts allow calculation of a rate of approximately 3.8 µmol/h for blue titania at 375 nm, and a conversion of MCH (1 mL amounts to 8 mmol) to the ketones of approximately 0.05% after reaction for 1 h. Furthermore, given the used light intensity, a photonic efficiency to the ketones, defined as the number of moles produced per hour, divided by the number of photons entering the reactor per hour (8.5×10^{-5} Einstein/h for 375 nm and 9.7×10^{-5} Einstein/h for 425 nm) of 5% can be calculated, which is an order of magnitude lower for the rutile sample (0.6%). These are values on the same order of magnitude as typically observed in selective photocatalytic transformations using catalyst coatings, obviously largely influenced by the rate of deactivation of the various catalysts and applied reactor configuration.

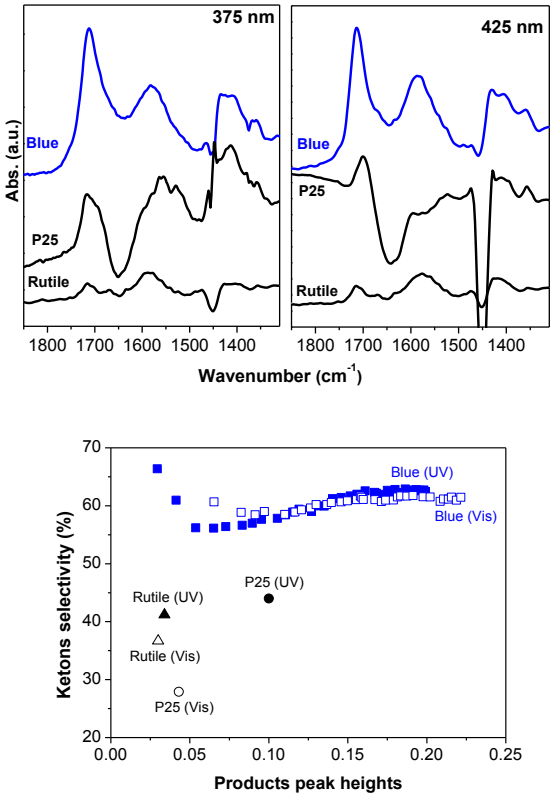

Figure 5. Top: The collected spectra of MCH photo-oxidation catalyzed by blue titania, P-25 and rutile under the illumination of 375 nm (Left) and 425 nm (right).

Bottom: The ketone selectivity plotted against the peak height of the products of MCH conversion.

Additional information on the ketone selectivity was obtained by analysing the time-dependent evolution of the height of the ketone band at 1716 cm^{-1} relative to that of carboxylate band at 1579 cm^{-1}. The development of these 2 bands is demonstrated in Figure 6 (see for the corresponding spectra Figure A1). Figure 6 proves -again- the high similarity in the product formation at 375 nm and 425 nm illumination. The products formed on the surface of blue titania seem to increase by the same rate, the product distribution at the different applied wavelengths (UV and visible illumination) also being very similar. The selectivity of ketones slightly improves (i.e. 55-60%) at extended reaction times, either under UV or visible light illumination. Lower selectivity towards ketones was obtained in the case of either rutile or P-25 after 200 minutes of reaction. Furthermore, the ratio between the adsorbed and dissolved ketones seems higher in the case of P25 than for the blue titania sample, by analysis of the bands in the ketone range in detail.

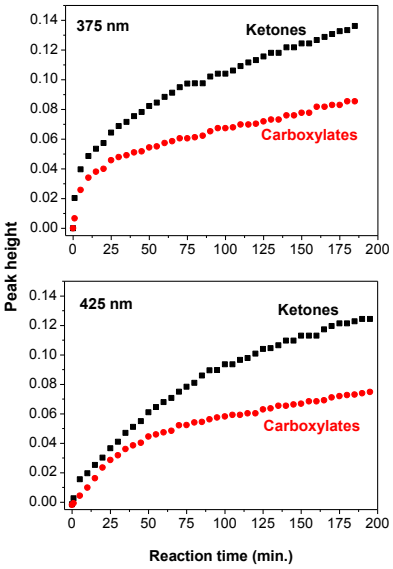

Figure 6. The time dependent evaluation of the peak height of the ketone (1712 cm^{-1}) and carboxylate (1586 cm^{-1}) bands, induced by photocatalytic oxidation of MCH over blue titania by illumination at 375 nm (top) and at 425 nm (bottom), respectively. The spectra are shown in Figure A1.

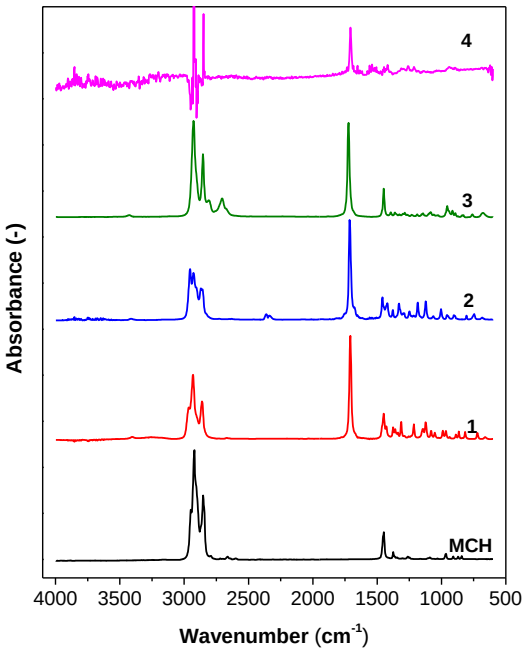

Figure 7. The ATR - FTIR spectra (on a ZnSe crystal) of MCH and the expected products; (**1**) o-methyl cyclohexanone, (**2**) p-methyl cycloehxanone, (**3**) formylcyclohexane, and (**4**) cyclohexane carboxylic acid.

4. Discussion

Generally, three main differences were found between the catalysts used in this study (i.e. blue TiO_2, P-25 and rutile TiO_2). First, the textural properties, second, the phase composition, and third, the presence or absence of (surface) defects. These three aspects are relevant to explain the differences in photocatalytic activity and in product selectivity in the photo-oxidation of MCH.

First, a correlation between the surface area and the photocatalytic activity of the three titania catalysts was not found: the surface areas of P-25 and rutile are significantly higher than that of the blue titania (Table 1), whereas the latter shows the highest activity.

The phase composition of the three samples is an interesting issue to discuss. The relationship between phase composition and the photocatalytic activity of TiO_2 was recently discussed by Li et al. [23] TiO_2 in the rutile form has often been

demonstrated to be less photo-active than TiO_2 in the anatase form [24]. This is in agreement with the presently obtained results, where rutile hardly activates the photo-oxidation of MCH when exposed to the two applied wavelengths, even though rutile has a smaller bandgap (3.05eV) compared to anatase (3.2eV), and hence shows a small red-shift in the absorption spectrum. The co-existence of rutile and anatase in P-25 (23% rutile and 77% anatase) has often been reported to be responsible for the enhanced activity of this catalyst as compared to anatase and rutile, explained by more effective charge separation (i.e. the antenna theory) [25]. To identify if the phase composition of the Ti^{3+} containing catalyst is a dominating factor in determining the activity, an experiment was performed in which we prepared a physical mixture of commercial rutile and anatase with the same ratio as in the blue titania sample (i.e. 15% anatase and 85% anatase). A negligible synergy was found under UV illumination, which is in a good agreement with the studies of Mul [26] and Besenbacher [27]. Hence, the co-existence of rutile and anatase phases is not the main reason for the higher photocatalytic activity of the neat Ti^{3+} containing catalyst.

A high photocatalytic activity of reduced TiO_2 under visible light illumination was reported previously. Mao et al. [6] reported a high photocatalytic activity of a black titania (hydrogenated titania) in the water splitting reaction, as well as in methylene blue degradation. Feng et al[15] also reported a blue, reduced, titania form, doped with Pt as an active catalyst for water splitting. Hashimoto et al. [28] reported Cu doped reduced titania as an active catalyst for the decomposition of 2-propanol. The reason of the high activity of the reduced titania was explained by the generation of sub-levels in the bandgap as a result of the presence of Ti^{3+}, of somewhat lower energy than the conduction band minimum of stoichiometric (Ti^{4+}) TiO_2 [6]. Under UV illumination, a TiO_2 photocatalyst will absorb light when of high enough energy, upon which an electron-hole pair is formed (equation 1), representing the photon-excited state. The energy of the photon-excited electron is dependent on being associated with the conduction band energy levels, or with the generated sub-level (both represented by Ti^{3+} (e^-) in equation 1). The electron will react with O_2 to form a super oxide anion (2) which will contribute to oxidation of MCH to form compound **1**, **2**, or **3** (3). Consecutive oxidation processes will open the ring to form carboxylate compounds (4). The holes will react with surface OH-groups (5) or with water (6) to form strongly oxidizing OH radicals. The hydroxyl radicals are necessary for the primary activation of the hydrocarbon, but also –most likely– will contribute to the degradation of MCH to carboxylates, and eventually to CO_2 and H_2O (7).

Under visible light illumination, globally the same elementary steps will occur for blue TiO_2, with the exception that now the majority of the excited state electrons will reside on the bulk and surface defect (Ti^{3+}) sites. However, these electrons, and the similar energetic state of the holes, will lead to the same redox reactions, and thus to the same catalytic selectivity. The absence of a significant enhancement in rate by increasing the energy of the photons to 375 nm, suggests that the Ti^{3+} centres are also dominating catalysis at this higher energetic radiation, possibly because these are the sites favouring O_2 adsorption. The excess energy of the 375 nm radiation is apparently lost by recombination of conduction band electrons and holes, or by relaxation of the conduction band electron to the state of the defect site, either radiatively or non-radiatively.

$$Ti^{4+}\text{—}O_2^{2-} + h\nu \rightarrow Ti^{3+}(e^-)\text{—}O_2^- (h^+) \quad (1)$$
$$e^- + O_2 \rightarrow O_2^{-\bullet} \quad (2)$$
$$O_2^{-\bullet} + R \rightarrow R{=}O \quad (3)$$
$$O_2^{-\bullet} + R{=}O \rightarrow O\text{-}C{=}O + C{=}O \quad (4)$$
$$h^+ + OH \rightarrow OH^{+\bullet} \quad (5)$$
$$h^+ + H_2O \rightarrow OH^\bullet + H \quad (6)$$
$$OH^\bullet + R \rightarrow \text{oxidized product} \quad (7)$$

The above given arguments suggest that the presence of the defect V_O Ti^{3+}-sites induces the high activity either upon UV or upon visible light illumination. Another separate experiment was carried out to confirm this concept: a new batch of the blue titania was prepared with only three quarters of the amount of reducing agents (i.e. ethanol and ethylimidazole). The aim was to produce less reducing gases and to create less V_O Ti^{3+}-sites. After 200 min reaction under illumination at 375 nm, it was clear that the photocatalytic activity of this catalyst was significantly smaller than of the catalyst containing a higher concentration of V_O Ti^{3+}-sites (see Figure A2). A remaining issue concerns the location of the surface defect sites, whether these are predominantly present in the Rutile or Anatase phase. Given the very low performance of the commercial Rutile phase and literature data[6], intuitively we favour the hypothesis that these are located on the Anatase phase, but this requires further investigation.

The difference in ketone selectivity between the various catalysts can most likely be explained by the nature of the catalyst surface and its affinity towards water. Water promotes the generation of hydroxyl radicals (equation 6), which likely leads to

higher rates in carboxylate production. To study the affinity of the blue titania towards water as compared to the commercial titania catalysts, the surface of each catalyst was kept at 120°C in helium environment for two hours, followed by collection of IR spectra in DRIFT mode. The spectra showed a greater affinity of P-25 towards water as compared to blue titania, in agreement with the differences in selectivity. The collected FTIR spectra of the MCH after the reaction clearly showed a higher ratio of desorbed species over adsorbed species in the case of P-25 than in the case of the blue titania sample (Figure 5), which is in agreement with the state of hydration of the catalyst [29].

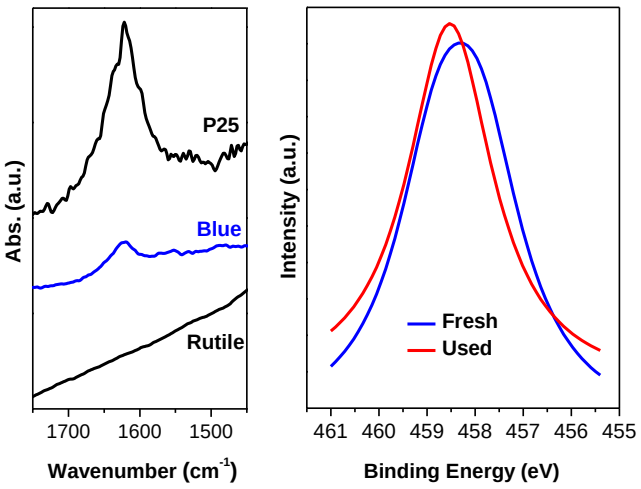

Figure 8. Left panel: The IR spectra of blue titania as compared to P-25 and Rutile. Right panel: The XPS Ti2p 458.1 eV band of the blue titania sample before the reaction (fresh) and after the reaction (used).

Although the blue titania catalyst showed better photo-activity and higher ketone selectivity than the commercial titania catalysts, this catalyst could not maintain such activity for long periods of time, and largely deactivated after the first run (not shown). The high photo-activity of the blue titania was attributed to the presence of Ti^{3+} (above), thus, besides the commonly observed detrimental effects of the adsorbed carboxylates and carbonates, a reduction in the amount of Ti^{3+} might contribute to catalyst deactivation. The XPS spectrum for the used blue titania was collected after the reaction, and compared with that of the fresh blue tiania sample (Figure 8, right panel). It is obvious that the area representing the reduced Ti^{3+} sites was smaller as compared to the fresh sample. This is an indication that the

concentration of Ti^{3+} decreases during the reaction. The reason for the deactivation might be explained by the reaction proposed earlier by Takeuchi et al. [30] and also by Harima et al. [31] in which Ti^{3+} in the presence of oxygen may undergo oxidation to Ti^{4+} as follows:

$$Ti^{3+}— —Ti^{3+} + O_2 \rightarrow Ti^{4+}—O_2^{2-}—Ti^{4+} \quad (8)$$

5. Conclusion

To conclude, blue titania is a more active photocatalyst than either P25 or commercial rutile titania, when applied in the oxidation of MCH, in particular at 425 nm. Blue titania also shows higher selectivity for the production of ketones. These phenomena are mostly related to a high concentration of surface defect sites (Ti^{3+}) and a relatively low but still significant affinity for water. The catalyst unfortunately showed deactivation as a result of photoinduced oxidation of Ti^{3+} to Ti^{4+} by molecular oxygen. The promotion of electron and oxygen transfer reactions by including (noble) metal particles with the reduced catalyst is currently under investigation, to determine if this is beneficial for catalyst stability and performance in general.

References

[1] S. Klosek, D. Raftery, Visible Light Driven V-Doped TiO_2 Photocatalyst and Its Photooxidation of Ethanol, The Journal of Physical Chemistry B, 105 (2001) 2815-2819.

[2] S. Zhang, Y. Chen, Y. Yu, H. Wu, S. Wang, B. Zhu, W. Huang, S. Wu, Synthesis, characterization of Cr-doped TiO₂ nanotubes with high photocatalytic activity, Journal of Nanoparticle Research, 10 (2008) 871-875.

[3] H. Yu, H. Irie, Y. Shimodaira, Y. Hosogi, Y. Kuroda, M. Miyauchi, K. Hashimoto, An Efficient Visible-Light-Sensitive Fe(III)-Grafted TiO_2 Photocatalyst, The Journal of Physical Chemistry C, 114 (2010) 16481-16487.

[4] Y. Cong, J. Zhang, F. Chen, M. Anpo, Synthesis and Characterization of Nitrogen-Doped TiO_2 Nanophotocatalyst with High Visible Light Activity, The Journal of Physical Chemistry C, 111 (2007) 6976-6982.

[5] F. Chen, W. Zou, W. Qu, J. Zhang, Photocatalytic performance of a visible light TiO_2 photocatalyst prepared by a surface chemical modification process, Catalysis Communications, 10 (2009) 1510-1513.

[6] X. Chen, L. Liu, P.Y. Yu, S.S. Mao, Increasing Solar Absorption for Photocatalysis with Black Hydrogenated Titanium Dioxide Nanocrystals, Science, 331 (2011) 746-750.

[7] H. Liu, H.T. Ma, X.Z. Li, W.Z. Li, M. Wu, X.H. Bao, The enhancement of TiO_2 photocatalytic activity by hydrogen thermal treatment, Chemosphere, 50 (2003) 39-46.

[8] A. Sirisuk, E. Klansorn, P. Praserthdam, Effects of reaction medium and crystallite size on Ti^{3+} surface defects in titanium dioxide nanoparticles prepared by solvothermal method, Catalysis Communications, 9 (2008) 1810-1814.

[9] V.E. Henrich, R.L. Kurtz, Surface electronic structure of TiO_2: Atomic geometry, ligand coordination, and the effect of adsorbed hydrogen, Physical Review B, 23 (1981) 6280-6287.

[10] G. Lu, A. Linsebigler, J.T. Yates, Ti^{3+} Defect Sites on TiO_2 (110): Production and Chemical Detection of Active Sites, The Journal of Physical Chemistry, 98 (1994) 11733-11738.

[11] Y. Li, X. Li, J. Li, J. Yin, TiO_2-coated active carbon composites with increased photocatalytic activity prepared by a properly controlled sol–gel method, Materials Letters, 59 (2005) 2659-2663.

[12] T. Le Mercier, J.M. Mariot, P. Parent, M.F. Fontaine, C.F. Hague, M. Quarton, Formation of Ti^{3+} ions at the surface of laser-irradiated rutile, Applied Surface Science, 86 (1995) 382-386.

[13] T.-C. Lu, L.-B. Lin, S.-Y. Wu, C.-P. Zhao, X.-C. Xu, Y.-F. Tian, Reduction effects in rutile induced by neutron irradiation, Nuclear Instruments and Methods in Physics Research Section B: Beam Interactions with Materials and Atoms, 191 (2002) 291-295.
[14] S. Dohshi, M. Anpo, S. Okuda, T. Kojima, Effect of gamma-ray Irradiation on the Wettability of TiO_2 Single Crystals, Topics in Catalysis, 35 (2005) 327-330.
[15] F. Zuo, L. Wang, T. Wu, Z. Zhang, D. Borchardt, P. Feng, Self-Doped Ti^{3+} Enhanced Photocatalyst for Hydrogen Production under Visible Light, Journal of the American Chemical Society, 132 (2010) 11856-11857.
[16] A.R. Almeida, J.A. Moulijn, G. Mul, In Situ ATR-FTIR Study on the Selective Photo-oxidation of Cyclohexane over Anatase TiO_2, The Journal of Physical Chemistry C, 112 (2008) 1552-1561.
[17] R. Li, H. Kobayashi, J. Guo, J. Fan, Visible-light-driven surface reconstruction of mesoporous TiO_2: toward visible-light absorption and enhanced photocatalytic activities, Chemical Communications, 47 (2011) 8584-8586.
[18] Y.C. Lee, Y.P. Hong, H.Y. Lee, H. Kim, Y.J. Jung, K.H. Ko, H.S. Jung, K.S. Hong, Photocatalysis and hydrophilicity of doped TiO_2 thin films, Journal of Colloid and Interface Science, 267 (2003) 127-131.
[19] S. Livraghi, S. Maurelli, M.C. Paganini, M. Chiesa, E. Giamello, Probing the Local Environment of Ti^{3+} Ions in TiO_2 (Rutile) by 17O HYSCORE, Angewandte Chemie International Edition, 50 (2011) 8038-8040.
[20] C.-C. Yang, Y.-H. Yu, B. van der Linden, J.C.S. Wu, G. Mul, Artificial Photosynthesis over Crystalline TiO_2-Based Catalysts: Fact or Fiction?, Journal of the American Chemical Society, 132 (2010) 8398-8406.
[21] M.D. Hernández-Alonso, I. Tejedor-Tejedor, J.M. Coronado, M.A. Anderson, Operando FTIR study of the photocatalytic oxidation of methylcyclohexane and toluene in air over TiO_2-ZrO_2 thin films: Influence of the aromaticity of the target molecule on deactivation, Applied Catalysis B: Environmental, 101 (2011) 283-293.
[22] M.D. Hernández-Alonso, I. Tejedor-Tejedor, J.M. Coronado, M.A. Anderson, Operando FTIR study of the photocatalytic oxidation of methylcyclohexane and toluene in air over TiO_2–ZrO_2 thin films: Influence of the aromaticity of the target molecule on deactivation, Applied Catalysis B: Environmental, 101 (2011) 283-293.
[23] J. Zhang, Q. Xu, Z. Feng, M. Li, C. Li, Importance of the Relationship between Surface Phases and Photocatalytic Activity of TiO_2, Angewandte Chemie, 120 (2008) 1790-1793.
[24] M. Addamo, M. Bellardita, A. Di Paola, L. Palmisano, Preparation and photoactivity of nanostructured anatase, rutile and brookite TiO_2 thin films, Chemical Communications, (2006) 4943-4945.

[25] D.C. Hurum, A.G. Agrios, K.A. Gray, T. Rajh, M.C. Thurnauer, Explaining the Enhanced Photocatalytic Activity of Degussa P25 Mixed-Phase TiO_2 Using EPR, The Journal of Physical Chemistry B, 107 (2003) 4545-4549.
[26] J.T. Carneiro, T.J. Savenije, J.A. Moulijn, G. Mul, How Phase Composition Influences Optoelectronic and Photocatalytic Properties of TiO_2, The Journal of Physical Chemistry C, 115 (2011) 2211-2217.
[27] R. Su, R. Bechstein, L. Sø, R.T. Vang, M. Sillassen, B. Esbjörnsson, A. Palmqvist, F. Besenbacher, How the Anatase-to-Rutile Ratio Influences the Photoreactivity of TiO_2, The Journal of Physical Chemistry C, 115 (2011) 24287-24292.
[28] J. Pan, X. Wu, L. Wang, G. Liu, G.Q. Lu, H.M. Cheng, Synthesis of anatase TiO_2 rods with dominant reactive {010} facets for the photoreduction of CO_2 to CH4 and use in dye-sensitized solar cells, Chemical Communications, 47 (2011) 8361-8363.
[29] T.J.A. Renckens, A.R. Almeida, M.R. Damen, M.T. Kreutzer, G. Mul, Product desorption limitations in selective photocatalytic oxidation, Catalysis Today, 155 (2010) 302-310.
[30] M. Takeuchi, G. Martra, S. Coluccia, M. Anpo, Verification of the Photoadsorption of H_2O Molecules on TiO_2 Semiconductor Surfaces by Vibrational Absorption Spectroscopy, The Journal of Physical Chemistry C, 111 (2007) 9811-9817.
[31] K. Komaguchi, T. Maruoka, H. Nakano, I. Imae, Y. Ooyama, Y. Harima, Electron-Transfer Reaction of Oxygen Species on TiO_2 Nanoparticles Induced by Sub-band-gap Illumination, The Journal of Physical Chemistry C, 114 (2009) 1240-1245.

Appendix

Figure A1

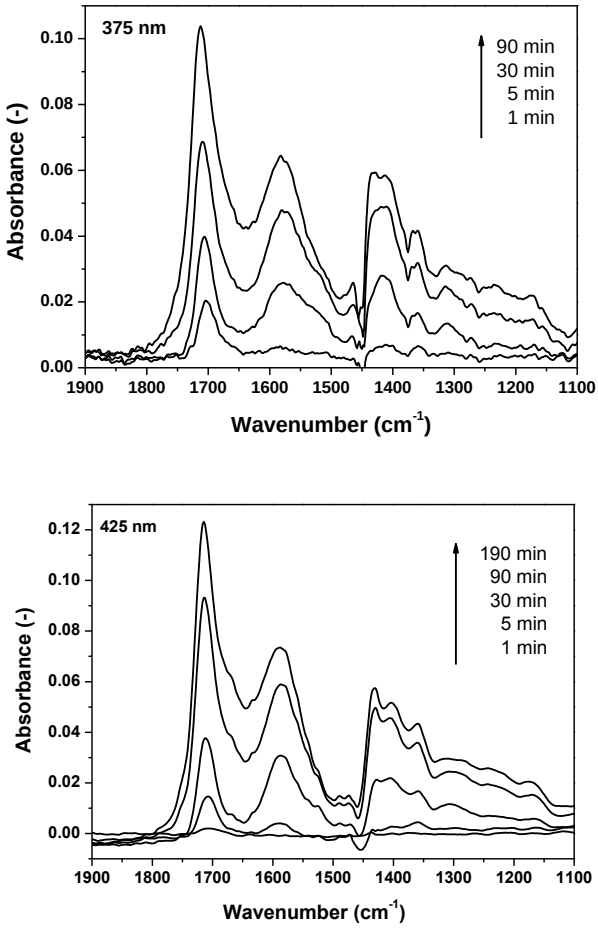

Figure A1. FTIR spectra of ketone and carboxylate bands arising from MCH oxidation over blue titania under illumination at 375 nm (top) and at 425 nm (bottom).

Figure A2

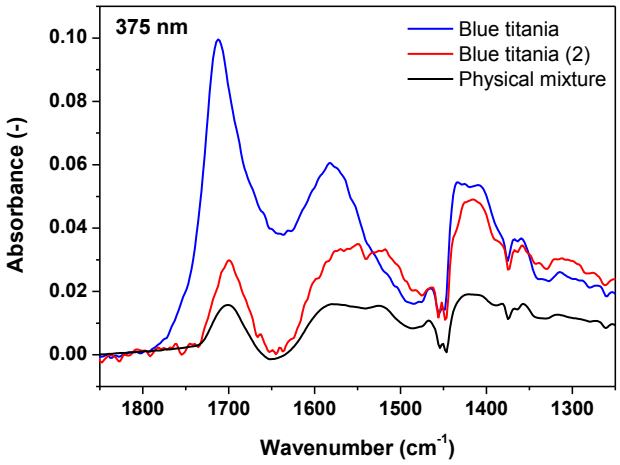

Figure A2. FTIR spectra of ketone and carboxylate bands arising after 90 minutes of 375 nm illumination from MCH oxidation over blue titania, blue titania (2) and a physical mixture of rutile and anatase. The blue titania (2) was prepared by using the same synthesis procedure of the blue titania sample, however only three quarters of the amount of ethanol and ethylimidazole were used. The physical mixture consists of 15% commercial anatase and 85% commercial rutile.

Chapter 4

Understanding promotion of photocatalytic activity of TiO_2 by Au nanoparticles

Au nanoparticles prepared by deposition–precipitation were evaluated in promoting photocatalytic activity of TiO_2 (P25) in the oxidation of methylcyclohexane. At 375 and in particular at 425 nm, Au was found to significantly enhance the rate induced by P25. Illumination of Au-promoted P25 at 525 nm did not result in any measureable activity. To validate whether the enhancement at 425 nm is purely catalytic, or if plasmonic effects are relevant, we compared the rates of Au/TiO_2 with Pt-promoted TiO_2 at 375 and 425 nm. At 375 nm, Pt nanoparticles induced larger catalytic effects than Au nanoparticles, whereas the rate enhancement induced by Pt was much lower than of Au at 425 nm. We assign the thus demonstrated Au based plasmonic phenomena at 425 nm to so-called plasmon resonance energy transfer, rather than to hot electron transfer, given the absence of activity at 525 nm.

Keywords: Au, TiO_2, photocatalysis, selective oxidation, wavelength, plasmon resonance energy transfer (PRET)

This chapter is based on: R. Amrollahi, M. S. Hamdy, G. Mul; "Understanding promotion of photocatalytic activity of TiO_2 by Au nanoparticles", Journal of Catalysis, 2014, 319, pp 194–199.

1. Introduction

TiO_2 is by far the most studied metal oxide photocatalyst, and many ways of manipulating the bulk and surface composition have been reported in the literature to enhance the activity [1-5]. Modifications are generally aimed at improving light absorption over a large range of (visible) wavelengths, as well as promoting electron-hole separation and transfer efficiency by e.g. annealing and addition of metal-, and/or metal oxide nanoparticles [6, 7]. Recently, very intriguing studies have been reported on an additional method to promote activity of (doped) TiO_2, i.e. the use of plasmon absorption properties of metal nanoparticles of typically Ag or Au [8-10]. Enhanced activity by incorporation of plasmonic particles in photocatalytically active layers has been reported for various reactions, including (gas phase) oxidation reactions of organic molecules [11] and (liquid phase) water splitting [12-14]. Two phenomena have been proposed in explaining the rate enhancement by plasmonic (nano) particles. i) Photo-excitation of Au nanoparticles leads to an electron-hole pair, of which the electron can be transferred to the conduction band of TiO_2, and the hole induces oxidation reactions [15-19], and ii) plasmon excitation results in an energy field (plasmon resonance energy) which positively influences TiO_2 excitation. This phenomenon is predominantly observed if overlap exists between plasmon and band-gap absorption [9, 20-23].

In this study, we address the possible plasmonic effect of Au nanoparticles prepared by deposition–precipitation on the photocatalytic activity of TiO_2 in a liquid phase hydrocarbon oxidation reaction, i.e. the conversion of methylcyclohexane to methylcyclohexanone. Photocatalytic activity of Au/P25 was evaluated by *in situ* ATR-FTIR spectroscopy. We will demonstrate that of the wavelengths investigated (375, 425 and 525 nm, and combinations thereof), Au nanoparticles are only effective in promoting rates at 375 nm and 425 nm. Furthermore, by comparing at these two wavelengths the promotion in rate induced by Au nanoparticles to Pt nanoparticles, we demonstrate that besides a catalytic effect, a plasmonic enhancement induced by Au is apparent, which is most likely associated with plasmon resonance energy transfer, rather than electron transfer.

2. Experimental section

2.1. Catalysts and chemicals

P25 was obtained from Evonik, while $HAuCl_4$ and Methylcyclohexane (MCH) were purchased from Sigma-Aldrich. P25, $HAuCl_4$ and MCH were used as received

without further purification. The Pt promoted P25 catalyst was prepared by Atomic Layer Deposition and kindly provided by the Delft University of Technology. Details of the methodology of atomic layer deposition and the morphology and characteristics of the Pt catalyst can be found in [24].

2.2. Preparation of the Au/P25 catalyst

Gold was deposited on the P25 surface at 0.2 wt% loading by deposition-precipitation. In this procedure 0.3 g of TiO_2 P25 was added to an aqueous solution of $HAuCl_4$ (0.1 M) previously adjusted to pH 9 by drop-wise addition of NaOH (0.1 M). The slurry was maintained at room temperature, and vigorously stirred overnight. Subsequently, the sample was filtered, washed with deionized water to remove chlorides, and then dried at 80 °C for 4 h in a furnace (static air). Finally the obtained purple powder was calcined at 450 °C (heating rate 10 K/min) in static air for 5 h. To exclude the influence of preparative conditions on the behavior of P25 in the photocatalytic reaction [25], all preparative steps were performed for P25 in the absence of the Au solution (0.1 M HCl was used instead), and this sample is denoted as calcined P25 throughout this chapter. To allow ATR analysis of methylcyclohexane oxidation, the catalysts were suspended in water at a concentration of 3 g/L. These suspensions were treated for 30 min in a 35 kHz Elmasonic ultrasonic bath; 2 mL of the resulting mixture was spread on a ZnSe crystal, followed by drying in vacuum overnight.

2.3. Material Characterization

The crystal structure of the material was determined by powder X-ray diffraction (XRD), using a Philips PW2050 (X'Pert-APD) diffractometer with Cu Kα radiation ($\lambda = 0.15406$ nm). Measurements were recorded in steps of 0.005° with a count time of 1 s in the 2θ range of 20° and 80°. Raman spectroscopy was performed at room temperature using a Raman spectrometer (Bruker Senterra) with a green laser 532 nm (2 mW). Spectra were acquired at a resolution of ~15 cm^{-1}, and 10 scans were accumulated for each spectrum. The BET area was measured by nitrogen adsorption at liquid nitrogen temperature in a Micrometrics ASAP 2400 apparatus. Before analysis, the samples were degassed for 24 h at 300 °C in vacuum. Diffuse reflectance UV-vis spectra (DRS) of the powders were recorded at ambient pressure and temperature on a Thermo Scientific Evolution 600 spectrophotometer, equipped with a diffuse reflectance accessory of Harrick, using $BaSO_4$ as reference. Spectra were recorded in the wavelength range of 350-800 nm. TEM imaging was carried

out using a Philips CM300ST-FEG microscope equipped with a Kevex EDX detector. Samples for TEM were prepared by deposition of a dispersion in ethanol onto a carbon coated TEM grid.

2.4. Photo-oxidation of Methylcyclohexane

The photocatalytic activity was determined using an attenuated total reflectance−Fourier transform infrared (ATR−FTIR) setup. The ZnSe crystal coated with the catalyst formulation was inserted in the sampling compartment of the spectrometer. 20 mL of MCH was saturated with O_2 by bubbling dry air at 8 mL/min for 30 min. Subsequently, O_2 saturated MCH was added to the catalyst layer, and the composition enclosed by a top plate containing a quartz window. Prior to the photocatalytic oxidation experiments, adsorption of MCH on the catalyst coating was monitored for 100 min. Then, a spectrum of adsorbed MCH on the coating was collected, and used as background spectrum for photocatalysis experiments. To study the effect of multiple wavelengths on photocatalytic activity, an assembly of 7 LEDs was used as light source. We used two different LED arrays. Both have 3 LEDs emitting at 525 nm, one alternating with four 375 nm LEDs, and another alternating with four 425 nm LEDs. The LEDs of different wavelengths could be switched on and off independently. The light intensity of the LEDs was fine-tuned to be equal at 1.5 mW/cm^2. A scheme of the ATR-FTIR setup is shown in scheme 1. Upon illumination, each spectrum was recorded at fixed time intervals (typically 1 min) from 4000 to 700 cm^{-1} by collecting 64 scans with a resolution of 1.5 cm^{-1}.

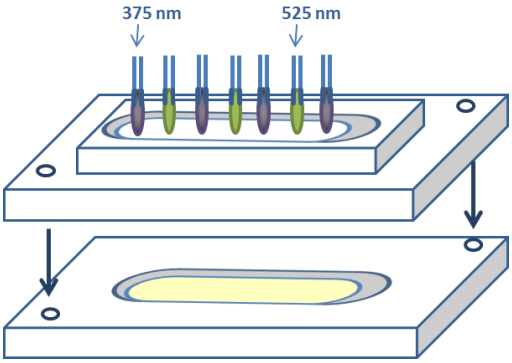

Scheme 1: Scheme of the applied ATR-FTIR cell, including the LED assembly (7 LED lamps with two different wavelengths of emission (375 nm and 525 nm)).

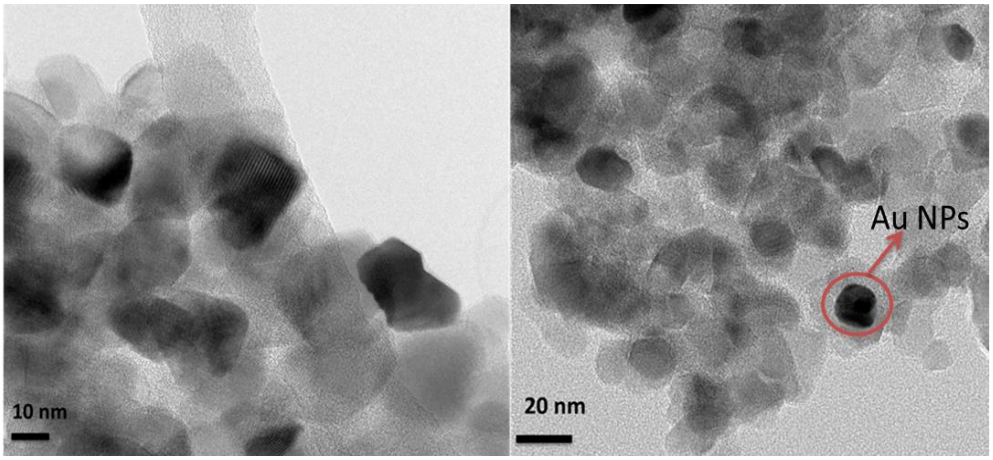

Figure 1: Transmission electron microscopy (TEM) images of Au/P25 (0.2%).

3. Results

3.1. Characterization

Figure 1 shows TEM images of the Au/TiO_2 sample prepared by the deposition–precipitation method (DP). Based on these images and energy-dispersive X-ray (EDX) analysis, Au nanoparticles are clearly identified ranging in size between 10-20 nm. Further, these results indicate that the DP method did not induce changes in TiO_2 morphology, of which the mean primary particle size is estimated to be around 15 nm. XRD and Raman analysis confirm the absence of dramatic changes in crystallinity and size of P25 TiO_2, potentially induced by the solutions used for Au deposition, and/or calcination (Figures 2 and 3). The lower intensities of the Raman features of P25 after Au deposition are likely the result of absorption of the laser light by the Au particles used for analysis (532 nm), reducing the scattering efficiency.

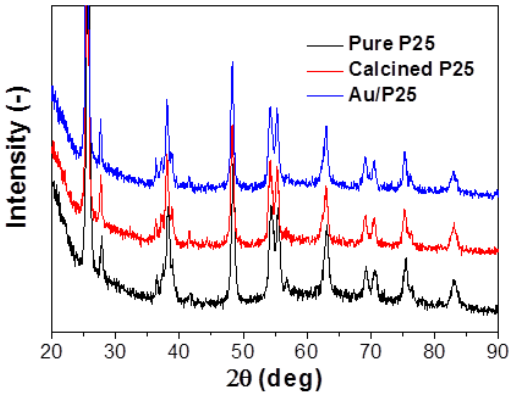

Figure 2: XRD pattern of Au/P25 compared with those of P25 pure and calcined.

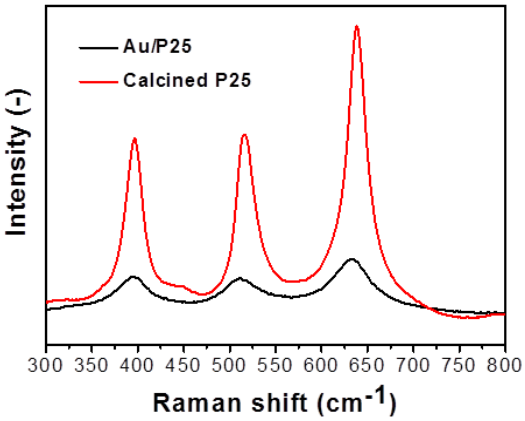

Figure 3: Raman spectrum of Au/P25, compared to the Raman spectrum of calcined P25. The spectrum is dominated by the Raman intensities expected for the anatase phase, with a slight shoulder at 450 cm^{-1} being indicative for the presence of Rutile.

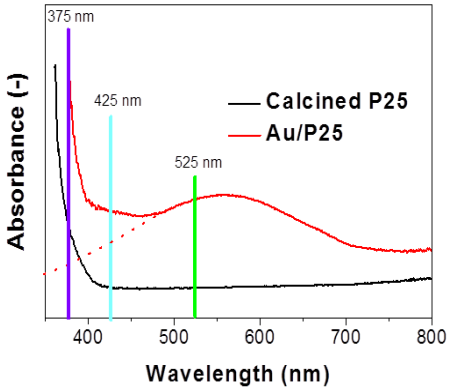

Figure 4: UV-vis diffuse reflectance spectra of Au/P25 and P25 both calcined at 450 ºC for 5 hours. The vertical lines indicate the wavelengths of the LED sources used in the photocatalysis experiments.

The UV-Vis diffuse reflectance spectra of TiO_2 and Au/P25 were recorded in the range of 350–800 nm, and the results are shown in Figure 4. P25 has no significant absorptions in the visible region (band edge at around 400 nm), while the surface plasmon absorption of gold nanoparticles can be observed maximizing around 560 nm.

3.2. Photoactivity of Au/P25 as a function of wavelength of excitation

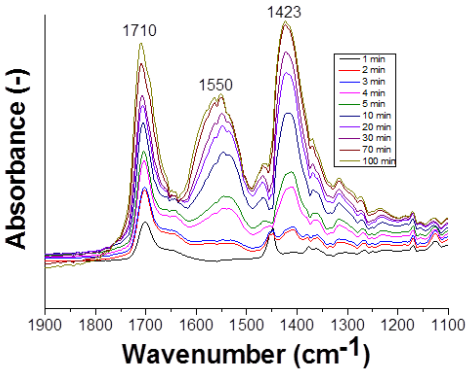

Figure 5: ATR-FTIR spectra of MCH on Au/P25 after illumination at 375 nm recorded from 1 min to 100 min.

The spectra of MCH oxidation on Au/P25 at 375 nm for 100 min are presented in Figure 5. Upon illumination, a broad range of infrared absorptions develop in time between 1800 cm^{-1} and 1200 cm^{-1}. As described in a previous study [26], photocatalytic oxidation of MCH takes place via formation of o-methylcyclohexanone and/or p- methylcyclohexanone by the oxidation of the aromatic ring. Subsequently, ring opening and formation of several carboxylate species is apparent, in agreement with a study reported by Alonas et al. [27]. To validate the rate of reaction induced by the various catalytic formulations, we show the rate of development of the intensity of the ketone band at 1710 cm^{-1} as a function time (Figure 6), particularly focusing on the initial growth rate: consecutive oxidation leads to irreversibly adsorbed carbonates and carboxylates, which influences the catalytic performance (as can be clearly observed in all the curves, as *per* the leveling off to a more or less constant value). Figure 6 shows the curves derived from the spectral data for P25 at 425 nm and 375 nm, in the absence or presence of Au nanoparticles.

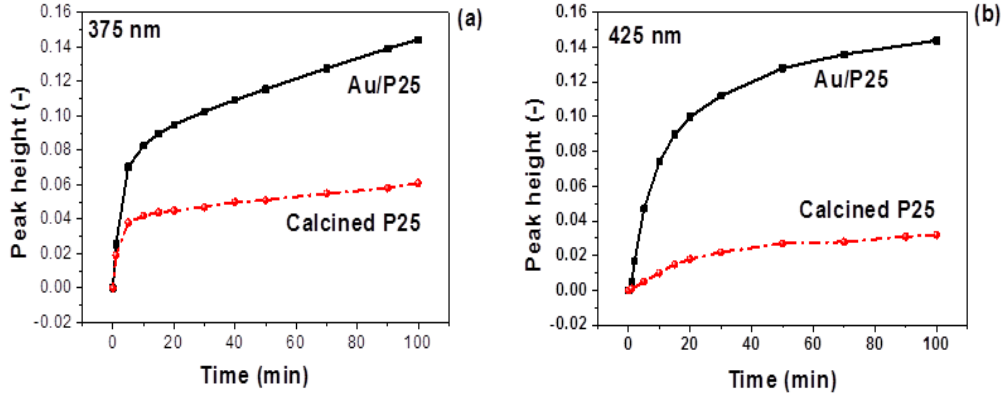

Figure 6: The time evaluation of the peak height of the Ketone vibrations (1710 cm-1) for both calcined P25 and Au/P25, respectively, induced by photocatalytic oxidation of MCH at 375 nm (a) and 425 nm (b).

At 375 nm (Figure 6a) both catalysts show a similar initial rate, while the growth of the ketone band continues for a longer period of time for the Au containing catalyst. This can be explained on the basis of Scheme 2: the rate of decomposition of carboxylates and carbonates to gas phase CO_2 (k_3) is likely higher in the presence of Au, causing the surface to be less quickly saturated with these species, thus

maintaining high photocatalytic MCH oxidation activity (scheme 2). This explanation is corroborated by literature data [28], showing smaller intensities of carboxylate and carbonate bands in the presence of Au, and the observation of large positive bands in the IR spectra of the Au containing catalyst in the present study in the region of spectral features of (adsorbed) water, the co-product of total oxidation of MCH to CO_2. In addition, in the Figure A1, we show ATR–FTIR spectra obtained after oxidation of MCH at 375 nm for 100 min for Au/P25 and P25, respectively. The absorption intensity of (dissolved) CO_2 is significantly higher for the Au containing catalyst, confirming a larger degree of complete oxidation induced by the presence of Au.

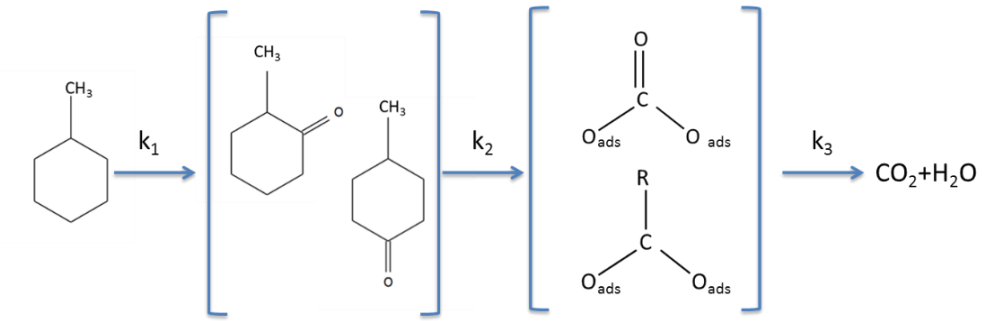

Scheme 2: Pathways of photocatalytic oxidation of MCH in the liquid phase. The rate of ketone formation (k_1), the rate of consecutive oxidation (k_2), and the rate of decomposition of carboxylates and carbonates to gas phase CO_2 (k_3) is demonstrated.

The comparison of the rates of ketone formation at 425 nm in the absence or presence of Au is shown in Figure 6b. Now the difference in initial rate is significant as compared to illumination at 375 nm. The initial rate for calcined P25 is 8 times smaller than for Au/P25 under the same reaction conditions. At the two wavelengths of excitation, the steady state (surface) composition of the Au containing catalyst is similar, showing higher quantity of ketone as compared to P25.

When both catalysts were excited at 525 nm (Figure 7), no appreciable rate of reaction was observed. This result is in agreement with earlier studies, which also did not show any activity in the conversion of cyclohexane over Au promoted TiO_2 when illuminated at 525 nm [28].

3.3. Multiple wavelength excitation

Various experiments were conducted at multiple wavelength excitation (see scheme Figure 7). In Figure 7, experiment number 1 and 4 are showing the previously discussed results of illumination by 375 nm and 525 nm independently. When the Au containing samples were illuminated with 375 nm (UV light) and 525 nm simultaneously (either with a delay (experiment 2), or without a delay (experiment 3)), no appreciable enhancement of the rate in methylcyclohexanone formation (again derived from spectral growth at 1710 cm^{-1}) was observed. On the contrary, co-excitation of Au nanoparticles at 525 nm slightly reduces the activity, while also the maximum attainable ketone concentration seems to be lowered. The absence of a positive effect in rate by co-excitation with 525 nm light, suggests heating of the Au particles is not contributing to enhancing the rate of P25 at 375 nm [29].

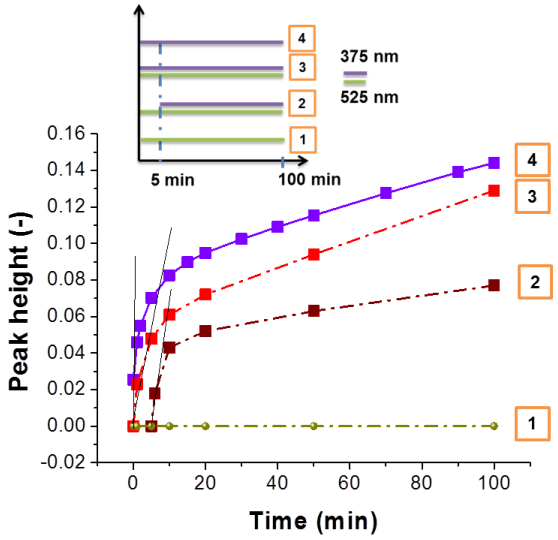

Figure 7: The time evaluation of the peak height of the ketone (1712 cm^{-1}) vibration for Au/P25, induced by photocatalytic oxidation of MCH. (1) Just 525 nm (2) 375 nm and 5 min afterwards 525 nm (3) Both 375 nm and 525 nm at the same time, and (4) 375 nm only.

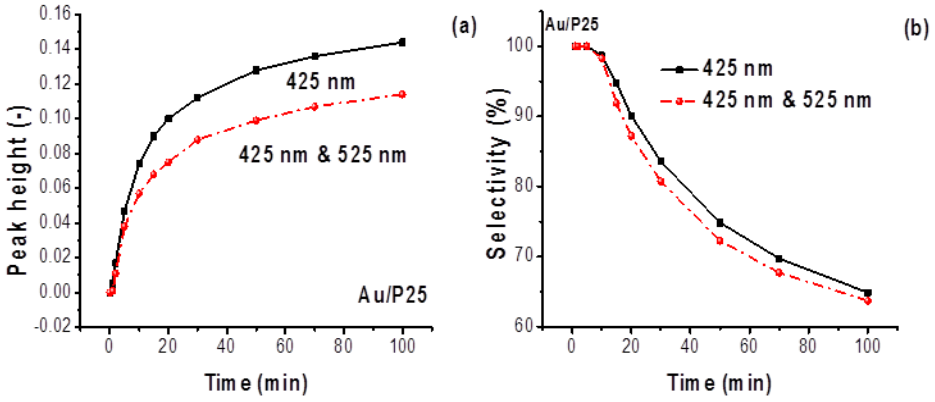

Figure 8: Catalytic rates (a) and selectivity changes (b) observed at 425 nm as compared to illumination with 425 nm and 525 nm simultaneously.

The photo oxidation of methylcyclohexanone over Au/P25 was also measured for a combination of 425 nm and 525 nm (Figure 8). Again addition of light energy at 525 nm, exciting the Au NPs, does not help to increase activity. In Figure 8-b the selectivity, determined by dividing the peak height at 1710 cm^{-1} (ketone) over 1552 cm^{-1} (carboxylate) during the reaction, is displayed. As expected, the selectivity decreases as a function of time of reaction. The rate at which selectivity decreases is similar in the absence or presence of 525 nm light.

3.4. Comparison of Au and Pt nanoparticles

To validate whether the enhancement at 425 nm is purely catalytic, or if plasmonic effects are relevant, we compared the rates of Au/TiO_2 with Pt-promoted TiO_2 at 375 and 425 nm (Figure 9). At 375 nm Pt nanoparticles induced a similar initial rate of reaction as compared to Au nanoparticles, but the time at which leveling off in the growth of the ketone band is observed is significantly longer. This can be explained by the high catalytic efficiency of Pt in the oxygen reduction reaction; an essential half reaction in converting alkanes over photo-excited TiO_2 either to selective products and/or CO_2. We suggest the latter is relevant for maintaining the observed catalytic activity over an extended period of time. Surprisingly, the effect of Pt nanoparticles was much less significant than of the Au nanoparticles in the reaction performed at 425 nm, both in terms of initial rate, as well as in maximized attainable (surface) ketone quantity. Figure 9b also shows a comparison between commercial P25, calcined P25 at 450 ^{o}C, and calcined P25 following the liquid exposures

relevant for the applied deposition–precipitation method. The spectral data show different treatments of P25 do not have a significant effect on photocatalytic activity in the oxidation of methyl cyclohexane, and therefore likely do not contribute to the identified changes related to metal deposition. At the same time, these data show that P25 is active at this relatively long wavelength, indicating light absorption is feasible. The comparison of reaction rates strongly suggests the effect of Au at 425 nm is not only catalytic, but also plasmonic, of which the mechanism is discussed in the following.

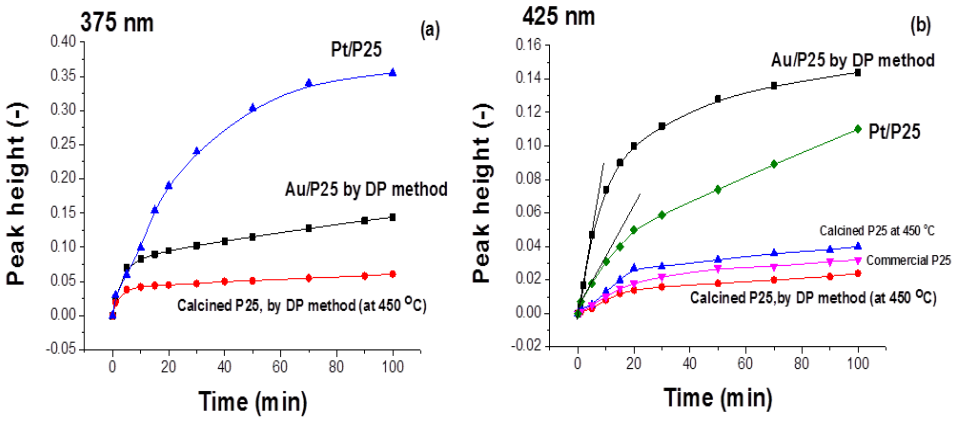

Figure 9: The time evaluation of the peak height of the Ketone (1710 cm^{-1}) vibration for calcined P25 prepared by the DP method, Au/P25 and Pt/P25, respectively, induced by photocatalytic oxidation of MCH at 375 nm (a) and calcined P25 at 450 ^{O}C, commercial P25, calcined P25 by DP method, Au/P25 and Pt/P25, respectively, at 425 nm (b).

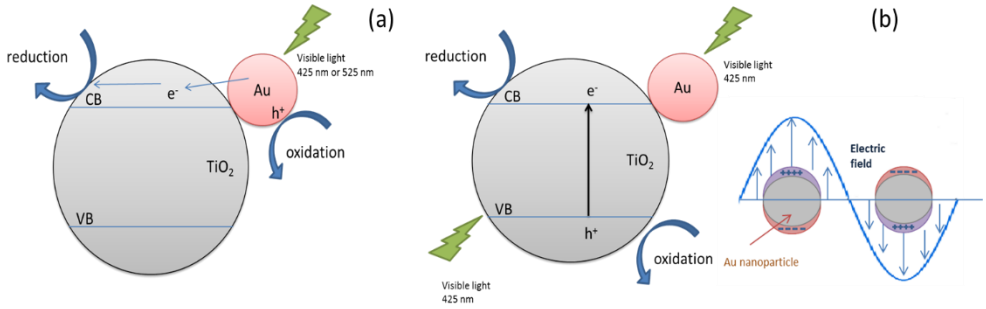

Figure 10: Illustration of the mechanism of 'hot electron transfer' proposed by [10, 19] (a) and the plasmon energy transfer mechanism proposed by [9, 20] (b).

4. Discussion

Before discussion of the data of activation at 425 nm, the observed effects at 375 nm need to be addressed. Principally, the improvement in catalytic behavior imposed by the Au and Pt nanoparticles at these wavelengths can be explained by the commonly advocated mechanism in which electron transfer from TiO_2 to the metallic NPs occurs, which has been demonstrated to be energetically favorable [29]. Further, the NPs catalyze oxygen reduction, (Pt more efficiently than Au), hence explaining the observed phenomena in Figure 9. On the other hand, the promoting effect of Au NPs at 425 nm is likely not purely catalytic, since compared to Pt (an excellent oxygen reduction catalyst) the effect of Au is much more significant, whereas the better catalytic properties of Pt are apparent at 375 nm. In order to explain the data obtained by illumination at 425 nm, we summarize the two plasmon absorption related mechanisms that have been reported in the literature: i) Photo-excitation of Au nanoparticles leads to an electron-hole pair, of which the electron can be transferred to the conduction band of TiO_2, and the hole induces oxidation reactions [15-19]. In 2004, Tatsuma's group proposed this charge transfer mechanism to explain their observation of photon to current conversion efficiency (IPCE) of TiO_2 increasing upon functionalization with Au or Ag [19]. Several groups used this mechanism to explain the effect of Au or Ag nanoparticles in promoting visible light induced photocatalytic reactions, such as water splitting [10], decomposition of methyl orange [29], and photo oxidation of organic compounds [30]. ii) Plasmon excitation results in an energy field (plasmon resonance energy) which positively influences TiO_2 excitation. This phenomenon is predominantly observed if overlap exists between plasmon and band-gap absorption [9,22 , 23]. Both mechanisms are illustrated in Figures 10a and 10b, respectively. The results of the present study

support the second explanation of the promoting effect of Au, since excitation of Au nanoparticles at 525 nm did not result in any observable rate in catalysis of alkane activation. Apparently charge transfer of the electrons to the conduction band of TiO_2 is not feasible under our reaction conditions. This might be related to the relatively large particle size (~10 nm) of the Au particles in the present study: the mean free path of electrons in metal particles is in the order of 1-2 nm, and hence photoexcited electrons have a low probability to 'escape' a 10 nm sized particle. A recent study by Chakarov et al. confirms the absence of catalytic conversion of TiO_2 functionalized with relatively large Au particles by excitation at 525 nm [29]. Overlap between the absorption of P25 and Au nanoparticles is apparently necessary to induce a synergistic effect, and present at 425 nm (Figure 4, light absorption of P25 at 425 nm demonstrated affective for photocatalysis by data in Figure 9), although admittedly relatively small. The observed activity in the present study is in agreement with recent studies advocating Plasmon Resonance Energy Transfer as an important phenomenon for plasmon induced photocatalysis, which provide significant additional physical background [9, 29].

5. Conclusions

We performed selective oxidation of MCH over P25 in the presence or absence of Au nanoparticles, and demonstrate for the first time that 10 nm Au particles have a strong positive effect on the photocatalytic rate in selective alkane oxidation of P25 upon illumination (with a 20 nm band width centered) at 425 nm: a wavelength allowing simultaneous photoexcitation of the P25 catalyst and Au nanoparticles. The effect is corroborated by the much stronger positive effect of Au at 425 nm, as compared to induced by Pt nanoparticles, excluding catalytic effects to be dominant. Since excitation at 525 nm does not lead to any activity for the studied reaction, we assign the plasmonic effect to the so-called plasmon energy transfer mechanism, requiring spectral overlap of band gap and plasmon absorption, rather than to the 'hot electron injection' theory.

References

[1] I. Paramasivam, J.M. Macak, P. Schmuki, Photocatalytic activity of TiO_2 nanotube layers loaded with Ag and Au nanoparticles, Electrochemistry Communications, 10 (2008) 71-75.

[2] H. Zhang, X. Lv, Y. Li, Y. Wang, J. Li, P25-graphene composite as a high performance photocatalyst, ACS Nano, 4 (2010) 380-386.

[3] J. Yu, Q. Xiang, M. Zhou, Preparation, characterization and visible-light-driven photocatalytic activity of Fe-doped titania nanorods and first-principles study for electronic structures, Applied Catalysis B: Environmental, 90 (2009) 595-602.

[4] S.G. Kumar, L.G. Devi, Review on modified TiO_2 photocatalysis under UV/visible light: Selected results and related mechanisms on interfacial charge carrier transfer dynamics, J Phys Chem A, 115 (2011) 13211-13241.

[5] M.A. Henderson, A surface science perspective on TiO_2 photocatalysis, Surface Science Reports, 66 (2011) 185-297.

[6] A. Primo, A. Corma, H. Garcia, Titania supported gold nanoparticles as photocatalyst, Physical Chemistry Chemical Physics, 13 (2011) 886-910.

[7] J.Y. Lan, X.M. Zhou, G. Liu, J.G. Yu, J.C. Zhang, L.J. Zhi, G.J. Nie, Enhancing photocatalytic activity of one-dimensional $KNbO_3$ nanowires by Au nanoparticles under ultraviolet and visible-light, Nanoscale, 3 (2011) 5161-5167.

[8] B.Z. Tian, J.L. Zhang, T.Z. Tong, F. Chen, Preparation of Au/ TiO_2 catalysts from Au(I)-thiosulfate complex and study of their photocatalytic activity for the degradation of methyl orange, Appl Catal B-Environ, 79 (2008) 394-401.

[9] S. Linic, P. Christopher, D.B. Ingram, Plasmonic-metal nanostructures for efficient conversion of solar to chemical energy, Nature Materials, 10 (2011) 911-921.

[10] C. Gomes Silva, R. Juarez, T. Marino, R. Molinari, H. Garcia, Influence of Excitation Wavelength (UV or Visible Light) on the Photocatalytic Activity of Titania Containing Gold Nanoparticles for the Generation of Hydrogen or Oxygen from Water, Journal of the American Chemical Society, 133 (2011) 595-602.

[11] D. Tsukamoto, Y. Shiraishi, Y. Sugano, S. Ichikawa, S. Tanaka, T. Hirai, Gold nanoparticles located at the interface of anatase/rutile TiO_2 particles as active plasmonic photocatalysts for aerobic oxidation, J Am Chem Soc, 134 (2012) 6309-6315.

[12] R. Abe, Recent progress on photocatalytic and photoelectrochemical water splitting under visible light irradiation, Journal of Photochemistry and Photobiology C: Photochemistry Reviews, 11 (2010) 179-209.

[13] O. Rosseler, M.V. Shankar, M.K.L. Du, L. Schmidlin, N. Keller, V. Keller, Solar light photocatalytic hydrogen production from water over Pt and

Au/TiO_2(anatase/rutile) photocatalysts: Influence of noble metal and porogen promotion, J Catal, 269 (2010) 179-190.
[14] J.J. Chen, J.C.S. Wu, P.C. Wu, D.P. Tsai, Plasmonic photocatalyst for H_2 evolution in photocatalytic water splitting, J Phys Chem C, 115 (2011) 210-216.
[15] W.-T. Chen, Y.-J. Hsu, P.V. Kamat, Realizing Visible Photoactivity of Metal Nanoparticles: Excited-State Behavior and Electron-Transfer Properties of Silver (Ag-8) Clusters, Journal of Physical Chemistry Letters, 3 (2012) 2493-2499.
[16] K. Adachi, K. Ohta, T. Mizuno, Photocatalytic reduction of carbon-dioxide to hydrocarbon using copper-loaded titanium-dioxide, Solar Energy, 53 (1994) 187-190.
[17] Y. Tian, T. Tatsuma, Mechanisms and applications of plasmon-induced charge separation at TiO_2 films loaded with gold nanoparticles, Journal of the American Chemical Society, 127 (2005) 7632-7637.
[18] M.S. Devadas, K. Kwak, J.-W. Park, J.-H. Choi, C.-H. Jun, E. Sinn, G. Ramakrishna, D. Lee, Directional Electron Transfer in Chromophore-Labeled Quantum-Sized Au-25 Clusters: Au-25 as an Electron Donor, Journal of Physical Chemistry Letters, 1 (2010) 1497-1503.
[19] Y. Tian, T. Tatsuma, Plasmon-induced photoelectrochemistry at metal nanoparticles supported on nanoporous TiO_2, Chemical Communications, (2004) 1810-1811.
[20] D.B. Ingram, P. Christopher, J.L. Bauer, S. Linic, Predictive Model for the Design of Plasmonic Metal/Semiconductor Composite Photocatalysts, Acs Catalysis, 1 (2011) 1441-1447.
[21] Y. Lu, H.T. Yu, S. Chen, X. Quan, H.M. Zhao, Integrating Plasmonic Nanoparticles with TiO_2 Photonic Crystal for Enhancement of Visible-Light-Driven Photocatalysis, Environ Sci Technol, 46 (2012) 1724-1730.
[22] S.L. Zou, G.C. Schatz, Silver nanoparticle array structures that produce giant enhancements in electromagnetic fields, Chemical Physics Letters, 403 (2005) 62-67.
[23] F. Le, D.W. Brandl, Y.A. Urzhumov, H. Wang, J. Kundu, N.J. Halas, J. Aizpurua, P. Nordlander, Metallic nanoparticle arrays: A common substrate for both surface-enhanced Raman scattering and surface-enhanced infrared absorption, Acs Nano, 2 (2008) 707-718.
[24] A. Goulas, J.R. van Ommen, Atomic layer deposition of platinum clusters on titania nanoparticles at atmospheric pressure, J Mater Chem A, 1 (2013) 4647-4650.
[25] J.T. Carneiro, C.C. Yang, J.A. Moma, J.A. Moulijn, G. Mul, How Gold Deposition Affects Anatase Performance in the Photo-catalytic Oxidation of Cyclohexane, Catal Lett, 129 (2009) 12-19.

[26] M.S. Hamdy, R. Amrollahi, G. Mul, Surface Ti^{3+}-containing (blue) titania: A unique photocatalyst with high activity and selectivity in visible light-stimulated selective oxidation, ACS Catalysis, 2 (2012) 2641-2647.
[27] M.D. Hernandez-Alonso, I. Tejedor-Tejedor, J.M. Coronado, M.A. Anderson, Operando FTIR study of the photocatalytic oxidation of methylcyclohexane and toluene in air over TiO_2-ZrO_2 thin films: Influence of the aromaticity of the target molecule on deactivation, Appl Catal B-Environ, 101 (2011) 283-293.
[28] J.T. Carneiro, T.J. Savenije, J.A. Moulijn, G. Mul, The effect of Au on TiO_2 catalyzed selective photocatalytic oxidation of cyclohexane, J Photoch Photobio A, 217 (2011) 326-332.
[29] J. Yu, G. Dai, B. Huang, Fabrication and Characterization of Visible-Light-Driven Plasmonic Photocatalyst Ag/AgCl/TiO_2 Nanotube Arrays, Journal of Physical Chemistry C, 113 (2009) 16394-16401.
[30] J. Tang, Interaction between Noble Metal Nanoparticles and Light for Contaminant Decomposition, Chemsuschem, 3 (2010) 800-801.

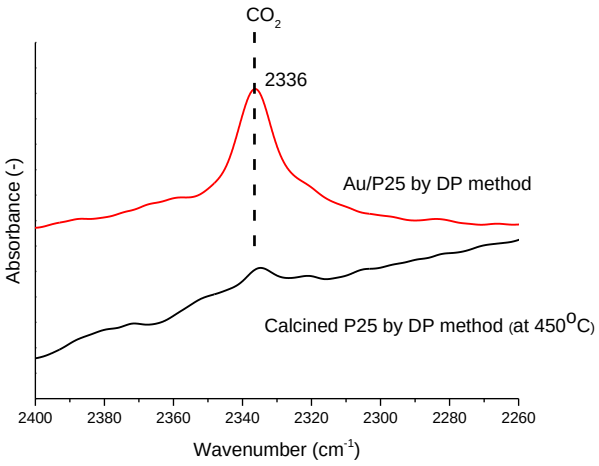

Figure A1: ATR-FTIR spectra obtained after oxidation of MCH at 375 nm for 100 min. over Au/P25 and P25, respectively. The absorption intensity of (dissolved) CO_2 is significantly higher for the Au containing catalyst, confirming a larger degree of complete oxidation induced by the presence of Au.

Table A1: Composition (Au in wt %) and Surface Area of the applied catalysts. The Au deposition procedure does not alter the surface area of P25, in agreement with the lack of morphological changes as derived from the XRD and Raman data.

Sample	XRF result	BET Surface Area
Calcined P25	0	58 ± 1 m^2/g
Au/P25 (0.2%)	0.1%	58 ± 1 m^2/g

Chapter 5

Synergy between Pt nanoparticles and Cr^{6+} in the photocatalytic performance of sol-gel derived TiO_2

In this study, titanium dioxide (TiO_2) containing 1 wt% of various elements (Ag, Cr, Cu, V, or Pt) was synthesized by a one-pot sol-gel method. The produced materials were extensively characterized by means of X-ray diffraction (XRD), BET surface-area measurements, Raman spectroscopy, UV-Vis spectroscopy and Transmission electron microscopy (TEM). UV-Vis spectroscopy demonstrated a clear shift in the absorbance of modified TiO_2 towards the visible light region. The photocatalytic performance of the prepared materials was evaluated in the photooxidation of methylcyclohexane (MCH) under the illumination of UV or Visible light. The performance was monitored by in situ ATR-FTIR. The best catalytic performance was obtained when Cr/TiO_2 was applied. The photocatalytic activity under visible light illumination could be further enhanced by photodeposition of Pt nanoparticles (0.06 wt % Pt) on the surface of Cr/TiO_2. The origin of the synergetic effect of Cr^{6+} and Pt nanoparticles will be discussed.

Keywords: Pt, Cr, TiO_2, doping, photodeposition, photocatalysis, selective oxidation, nanoparticles, methylcyclohexane

This chapter is based on: R. Amrollahi, M. S. Hamdy, G. Mul; Title; "Synergy between Pt nanoparticles and Cr^{6+} in the photocatalytic performance of sol-gel derived TiO_2'' to be submitted.

1. Introduction

Photocatalysis has been reported to be a feasible method to synthesize various products of hydrocarbon oxidation. Among many photocatalysts, TiO_2 is the most promising for practical use, because it has the most efficient activity, the highest stability, and the lowest cost [1]. Unfortunately, TiO_2 is only effective under ultraviolet irradiation (<387 nm) which accounts for only 4% of the solar energy, and hence, improving the photocatalytic activity of TiO_2 when excited by light of the visible region is a major focus of the research community investigating TiO_2 based photocatalysis [2].

Various approaches have been studied to induce photocatalytic activity of TiO_2 when exposed to visible light, including doping with metal ions (e.g. V, Cr, Fe, Co, Mn, Mo, Ni, Cu, Y, Ce, and Zr) [3] or nonmetallic elements (e.g., S, C, N) [4]. Furthermore, combinations of metal and nonmetal doping of TiO_2 (Mo-C [5] and, Cl-Br [6], N-Fe [7]) have also been investigated. Finally, some studies discuss co-doping of TiO_2 with two metal ions, such as $Pt^{(II)}/V^{(V)}/TiO_2$ [8], or $Mo^{(VI)}/V^{(V)}/TiO_2$ [9]. It should be noted that a combination of doping (incorporation of foreign ions in the lattice of TiO_2), and functionalization of the surface by deposition of metal nanoparticles, has not received as much attention. Furthermore, the effect of doping of TiO_2 on photocatalytic performance has been mainly investigated in the overall water splitting reaction [10], or oxidation of contaminants in aqueous waste streams [11]. The effect of dopants on performance in the selective oxidation of hydrocarbons has been reported less frequently.

In this study, we address the visible light induced possible synergetic effect of $Pt/Cr/TiO_2$. First of all photocatalytic performance of M/TiO_2 (M=Cr, V, Cu, Ag, or Pt), prepared by a one-step sol-gel method, in the selective oxidation of methylcyclohexane (MCH). The photocatalytic activity was assessed by *in situ* ATR-FTIR spectroscopy. Cr/TiO_2 was found to be the most active catalyst. Interestingly, functionalization of Cr/TiO_2 with Pt nanoparticles prepared by photodeposition, further enhanced the performance. A possible mechanism is proposed to explain the synergy between Cr^{6+} ions and Pt nanoparticles.

2. Experimental section

2.1. M/TiO_2 catalysts and chemicals

TiO_2 nanoparticles (NPs) were prepared by a standard sol-gel method reported by Choi and co-workers [12, 13]. In a typical synthesis, 5.0 mL of titanium tetra-isopropoxide (TTIP, Sigma-Aldrich) was dissolved in 50 mL of ethanol (>99.8%, Sigma-Aldrich) followed by drop-wise addition of 50 mL of mQ water while stirring at room temperature. Finally, the pH was adjusted to 1.5 by dropwise addition of HNO_3 (0.1 M). After one day, the suspension was filtered, washed with excessive aliquots mQ water, and dried in a stove (80 ^oC) for a period of 8 hours. The obtained powders were calcined at 400 ^oC (10 K/min.) for 1 hour in air atmosphere. Doped TiO_2 samples (M/TiO_2) were prepared by adding the following metal precursors to the mQ water prior to the TTIP, equivalent to a doping level of 1 wt %: Platinic acid (H_2PtCl_6), chromium nitrate (Cr (NO_3)$_3$), Vanadium chloride **(**VCl_3), silver nitrate ($AgNO_3$) and copper nitrate ($Cu(NO_3)_2$), used as received from Aldrich.[13]

2.2. Preparation of Pt/Cr/TiO_2

The platinum co-catalyst was deposited on Cr/TiO_2 by suspending 0.5 g powder of Cr/TiO_2 in 13 mL of a 0.5 g/L H_2PtCl_6 solution, diluted with 12 mL of methanol and 40 mL of mQ water. Then UV illumination using a 50 W HBO mercury lamp (Zeiss, 46 80 32 – 9902) was applied for 3-hours. Afterwards the solution was filtered and washed three times with demineralized water, and dried at 80^0C for 8 h.

2.3. Characterization of the photocatalysts

The photocatalysts were characterized by X-ray diffraction (XRD), using a Bruker D2 phaser (Cu kα source) Diffractometer. Measurements were recorded in steps of 0.005° with a count time of 1 s in the 2θ range of 20° to 80°. Particle sizes were determined by transmission electron microscopy (TEM, Philips CM300ST-FEG), and the presence of Pt particles determined by Energy Dispersive X-ray spectroscopy (EDX, Noran System Six). Raman spectroscopy was performed using a Raman spectrometer (Bruker Senterra) with a green laser 532 nm (2 mW). Spectra were acquired at a resolution of ~15 cm^{-1}, and 10 scans were accumulated for each spectrum. Specific BET surface area was determined using a Micromeritics Tristar 3000 measuring apparatus. Samples were degassed at 300°C for 24 hours prior to the BET measurements. UV-vis spectra of the powders were measured on a Thermo

Scientific Evolution 600 spectrophotometer, equipped with a diffuse reflectance accessory of Harrick, using $BaSO_4$ as reference. Spectra were collected in the wavelength range of 350-800 nm.

2.4. In Situ ATR-FTIR spectroscopy

A Bruker Vertex 70 spectrometer, equipped with a Harrick Scientific ATR accessory, was used to evaluate photocatalytic performance as described in detail elsewhere [14]. For the preparation of a thin film layer of a catalyst on a ZnSe ATR crystal, mQ water suspension including a powder concentration of 2.92 g L^{-1} was treated for 30 min in a 35 kHz Elmasonic ultrasonic bath. 2 ml of a prepared suspension was carefully drop casted on the ATR crystal, and dried in a desiccator at room temperature in vacuum overnight. To determine photocatalytic activity, 20 mL of MCH was purged with dry air using a flow of 8 mL/min for a period of 60 min. Afterwards, the O_2 saturated MCH was added to the catalyst coating, and then enclosed by a top plate containing a quartz window. Before experiment, a spectrum of adsorbed MCH on the catalyst coating was recorded, and used as background spectrum for other measurements. Every 1 min, a spectrum was measured from 700-4000 cm^{-1}, averaged from 64 scans with a resolution of 4 cm^{-1}. To initiate photocatalytic activity, an assembly of 7 LEDs (375 nm or 425 nm) was used as a light source, of which the intensity was equivalent to 1.5 mW/cm^2.

2.4.1.*Calculation of product concentrations*

To build a calibration model allowing (rough) estimation of the apparent quantum efficiency, solutions of potential products were prepared, such as 2-methylcyclohexanone in methyl cyclohexane, and ATR spectra recorded using crystals with pristine P25 coatings. A relation between peak height and concentration of products could thus be established.

3. Results and discussion

3.1. Characterization and photocatalytic properties of single metal doped TiO_2 (M/TiO_2)

UV-Vis spectroscopy was employed to investigate absorption characteristics of the metal doped TiO_2 photocatalysts. The UV-vis absorption spectra are presented in Figure 1. The UV–vis spectrum of sol-gel TiO_2 is also shown for comparison. As expected, the absorption edge of TiO_2 is located at approximately 395 nm.

By adding metal ions (Ag^{+}, Pt^{2+}, Cu^{2+}, Cr^{6+}, or V^{5+}), the absorption edge extends to longer wavelengths, with the most significant absorption in the visible induced by V^{5+} and Cr^{6+}.

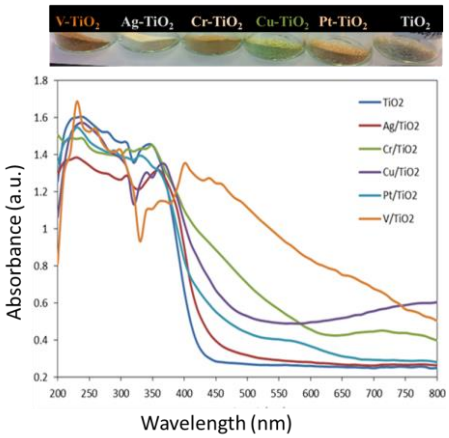

Figure 1: Top: Indication of the color of the prepared materials. Bottom: The UV-vis spectra of M/TiO_2 (M=Cr, V, Cu, Pt, or Ag) as compared to non-doped TiO_2.

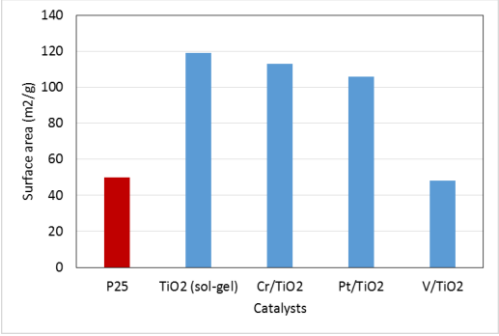

Figure 2: The BET surface area of the prepared materials compared to that of commercially available TiO_2 (P25)

Figure 2 shows the BET surface areas of the as-prepared samples in comparison to P25. The BET area was determined to be 119 m^2/g for TiO_2, 113 m^2/g for Cr/ TiO_2, and 106 m^2/g for Pt/ TiO_2, respectively, while the surface area of P25 TiO_2 is around 50 cm^2/g. The surface area of these samples is considerably higher than of P25. However, the surface area of V/ TiO_2 (48 m^2/g), was lower than those of the other M/TiO_2 samples and similar to P25.

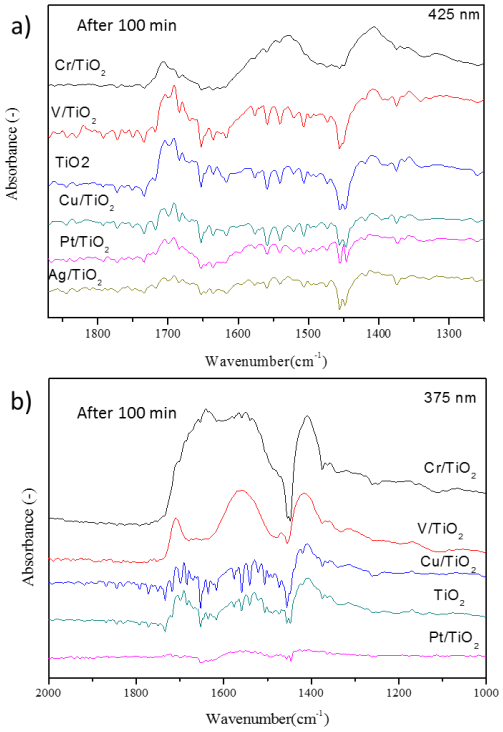

Figure 3: The collected spectra of photo oxidation of MCH catalyzed by M/TiO_2 (M=Cr, V, Cu, Pt or Ag) and TiO_2. Illumination at 425 nm (a) or 375 nm (b) was applied. Spectra were measured in ATR mode after 100 min of reaction time.

The IR spectra of the products formed by MCH oxidation after photoexcitation at 425 nm or 375 nm of M/TiO_2 (M=Cr, V, Cu, Pt and Ag) for a period of 100 minutes, are compared in Figures 3a and 3b, respectively. The assignment of the several bands observed in the spectra has been discussed in our previous work [15]. Briefly, the band at 1702 cm^{-1} is assigned to ketones. The bands in the region of 1550-1600 cm^{-1} are indicative of the formation of carboxylates, such as formate and acetate. Carbonates can be recognized at 1440 cm^{-1}. Also the band of absorbed water can be identified by a broad band at around 1615 cm^{-1}, overlapping with the 1560 cm^{-1} band of carboxylates. Clearly, the Cr/TiO_2 sample is photocatalytically more active than others at both conditions (illumination at 375 or 425 nm), although the selectivity to the ketones is significantly smaller, in view of the large carboxylate and carbonate signatures in the spectrum of Cr/TiO_2 induced MCH oxidation. The photocatalytic

activity and selectivity induced by the other M/TiO_2 catalysts and TiO_2 is very comparable when illumination at 425 nm is applied (Figure 3-a). This suggests a similar oxidation mechanism is operative for M/TiO_2 at 425 nm, and the dopants have very little effect on selectivity. For TiO_2, Cu/TiO_2, and Pt/TiO_2 differences in the activity and selectivity when photo-excited at 375 nm (Figure 3-b) are not very significant. On the other hand, the Cr/TiO_2 and V/TiO_2 samples show much more significant conversion at 375 nm as compared to at 425 nm. The broad features in the spectrum of the Cr/TiO_2 catalyst can be assigned to excessive formation of water. The selectivity of the V/TiO_2 sample towards ketones is significantly smaller at 375 nm as compared to 425 nm, as evident from the strong absorptions in the carboxylate and carbonate region of the spectrum.

3.2. Characterization and photocatalytic properties of TiO_2 and Cr/TiO_2 after photo-deposition of Pt nanoparticles.

Noble metal nanoparticles have been frequently reported to enhance photocatalytic efficiency of semiconductors in reducing oxygen, thereby promoting oxidation of hydrocarbons. In this study, Pt nanoparticles were prepared by photodeposition, and in this paragraph TiO_2, Pt/TiO_2, Cr/TiO_2 and $Pt/Cr/TiO_2$ (0.06%) samples are compared for activity. Figure 4-a shows the XRD spectra of these samples. The XRD spectra indicate the samples consist of the anatase crystal phase of TiO_2, while diffraction peaks related to Pt nanoparticles or Cr-oxides were absent. This shows that the incorporation of Cr or Pt in the lattice structure of TiO_2 (Cr/TiO_2 or Pt/TiO_2) did not induce the formation of new phases, and the Pt particles prepared by photodeposition ($Pt/Cr/TiO_2$ (0.06%)) are likely small. This is also in agreement with literature [12]. Only a small peak related to the rutile phase is detected in the XRD patterns of the doped samples (Figure 3-a, indicated by ‘R’).

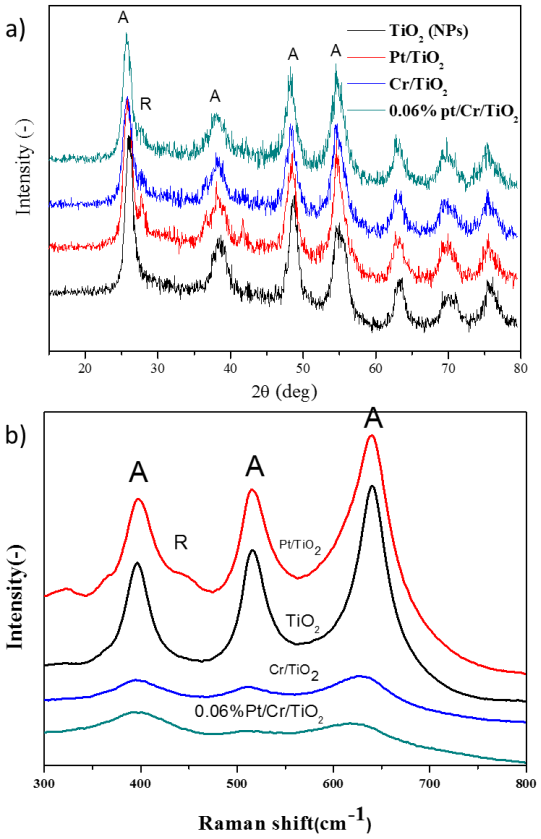

Figure 4: a) The XRD patterns of TiO_2, Pt/TiO_2, Cr/TiO_2 and $Pt/Cr/TiO_2$ (0.06%). (R) refers to the typical lines of the rutile phase, whereas (A) refers to anatase. b) Raman spectra of the same samples.

Raman spectra of TiO_2, Pt/TiO_2, Cr/TiO_2 and $Pt/Cr/TiO_2$ (0.06%) are shown in Figure 4-b. Three fundamental Raman active features of anatase (397, 515 and 642 cm^{-1} are observed in all samples. For the doped Pt/TiO_2 sample, rutile can be identified by the Raman band at 442 cm^{-1}. The Raman spectra confirm the conclusions derived on the basis of the XRD patterns. New phases have not been detected, and only some rutile might have formed when Pt or Cr ions are present in the sol gel mixture used for preparation of the samples.

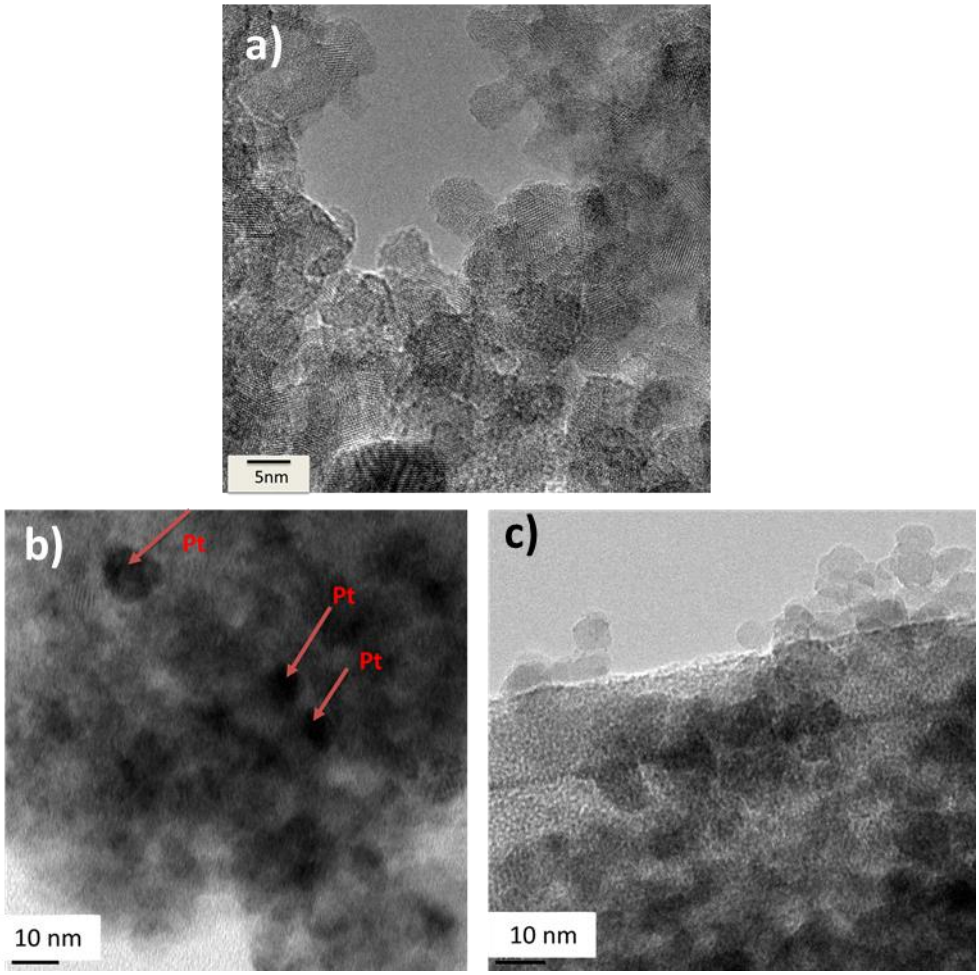

Figure 5: Transmission electron microscopy (HR-TEM) micrographs of the $Pt/Cr/TiO_2$ (0.06%) sample

Figure 5 shows HR-TEM micrographs of $Pt/Cr/TiO_2$ (0.06%). The obtained Cr/TiO_2 is composed of small, agglomerated particles, in the size range of 5-10 nm. Generally Pt nanoparticles were very hard to identify in the sample, due to the low loading of Pt. Figure 5-b shows areas with strong contrast, which might be indicative of the presence of Pt nanoparticles. The average nanoparticle size of Pt is then in the same order of magnitude as of the Cr/TiO_2, and about 5 nm.

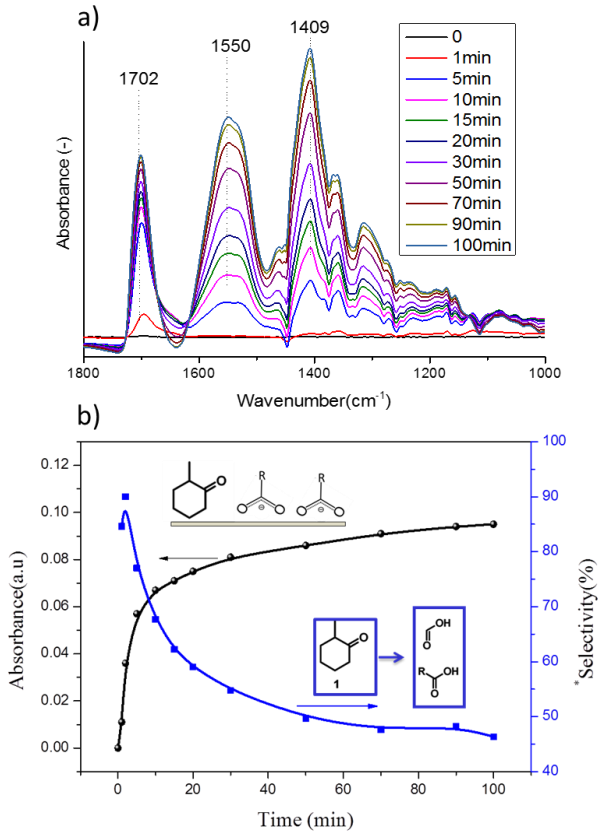

Figure 6: a) ATR-FTIR spectra of MCH oxidation using Pt/Cr/TiO_2 (0.06%) and illumination at 425 nm (visible light), recorded from 0 min to 100 min. b) The time evaluation of the peak height of the ketone vibrations (1702 cm^{-1}) and selectivity (determined by division of the peak height at 1702 cm^{-1} over 1552 cm^{-1}), obtained from figure 5-a.

The spectra of MCH oxidation using Pt/Cr/TiO_2 (0.06%) and illumination at 425 nm (visible light) are presented in Figure 6-a. A wide range of IR absorptions, similar to observed in Figure 3, grow as a function of time. The interpretation is similar as to previously discussed [16]. The growth of the intensity of the absorbance due to formation of ketones at 1702 cm^{-1} as a function time is shown in Figure 6-b (black curve). In Figure 6-b (blue curve), the selectivity, determined by dividing the peak height at 1702 cm^{-1} over 1552 cm^{-1} (ketones over carboxylate), is presented. The selectivity of ketones declines as a function of time of reaction.

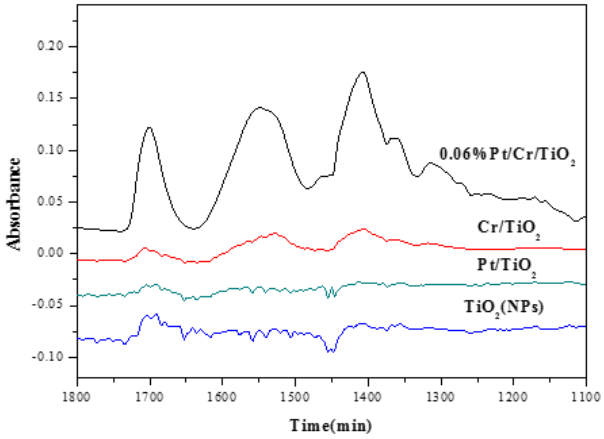

Figure 7: The visible light photocatalytic activity of $Pt/Cr/TiO_2$ (0.06%), Cr/TiO_2, Pt/TiO_2 and TiO_2 for Methylcyclohexane (MCH) oxidation. In situ ATR-FTIR spectra obtained by excitation at 425 nm after 100 min.

A comparison of the visible light photocatalytic activity of $Pt/Cr/TiO_2$ (0.06%), Cr/TiO_2, Pt/TiO_2 and TiO_2 for MCH oxidation is shown in Figure 7. Clearly, the activity of $Pt/Cr/TiO_2$ (0.06%) is much more significant as compared to the other samples. In case of the $Pt/Cr/TiO_2$ (0.06%) sample, the peak intensity at 1702 cm^{-1} is about 10 times larger than for the other samples under the same reaction conditions.

Using calibration data, the growth of the ketone band can be calculated to indicate a rate of formation of about 3.4 µmol/h for $Pt/Cr/TiO_2$ (0.06%) at 425 nm. Conversion of MCH to ketones (0.90 mL amounts to 8 mmol) after reaction for 100 min then equals nearly 0.045%. Moreover, for the used light intensity, an apparent quantum efficiency to the ketones, defined as the amount of moles produced, divided by the amount of photons sent into the reactor, (8.71×10^{-5} Einstein/h at 425 nm) of 4.5% can obtained. This is of a similar order of magnitude reported in selective photocatalytic conversion using effective catalyst layers [15].

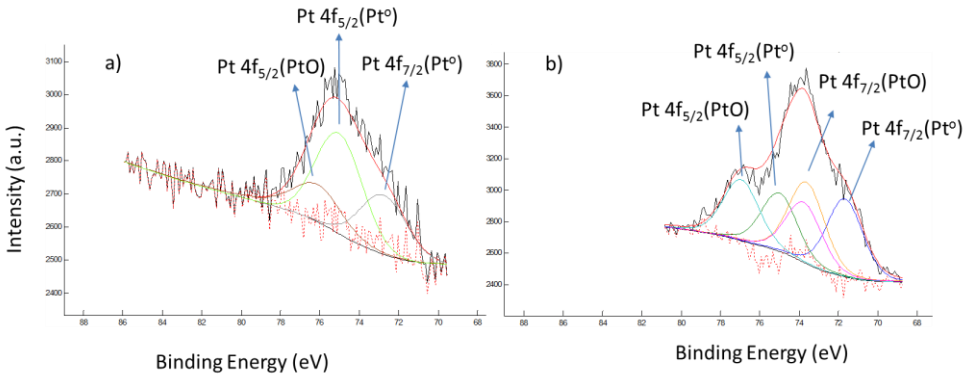

Figure 8: Deconvoluted XPS spectra of the Pt 4f region for a) Pt/Cr/TiO_2 (0.06%) and b) Pt/Cr/TiO_2 (0.25%).

To identify the cause of the very high activity of the Pt/Cr/TiO_2 (0.06%) sample, XPS measurements were carried out to identify the Cr and Pt surface oxidation states. For comparison, a separately prepared sample with higher Pt loading was also analyzed. The surface atomic weight percentage of Pt was estimated to be around 0.06% (Figure 8-a), and 0.25% (Figure 8-b) for the sample of higher loading. In Figure 8-a the spectrum in the Pt 4f region can be deconvoluted by 3 peaks. The Pt $4f_{7/2}$ peak at 72.8 eV, and Pt $4f_{5/2}$peak at 75.01 eV are assigned to metallic platinum, whereas the Pt $4f_{5/2}$ peak at 76.11 eV might indicate the presence of some PtO. In Figure 2A-a, the spectrum of Cr in the 2p region is shown to be composed of 2 peaks. The Cr $2p_{3/2}$ peak at 577.47eV, and the Cr $2p_{1/2}$ peak at 586.67 eV are assigned to Cr^{6+}. In Figure 8-b the spectrum of the sample with a higher Pt loading shows 4 peaks in the Pt 4f region. The Pt $4f_{7/2}$peak at 73.54 eV, and Pt $4f_{5/2}$peak at 77.22 eV can be assigned to PtO, while the Pt $4f_{5/2}$ peak at 74.98 eV and Pt $4f_{7/2}$peak at 71.62 eV can be assigned to metallic platinum [17]. The spectra in the Cr-region are very similar to the first sample (compare Figure 2A-a and Figure 2A-b), showing a Cr $2p_{3/2}$ peak at 578.54 eV, and Cr $2p_{1/2}$ peak at 587.78 eV [18].

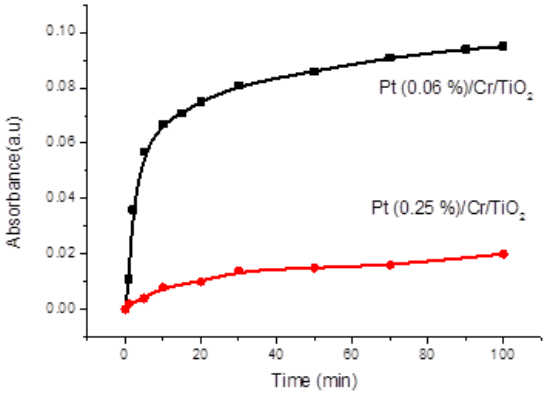

Figure 9: The time evaluation of the peak height of the ketone vibrations (1702 cm^{-1}), comparing $Pt/Cr/TiO_2$ (0.06%) and $Pt/Cr/TiO_2$ **(**0.25%**)**

Figure 9 shows the time dependent evolution of the peak height of the ketone absorptions (1702 cm^{-1}) for the samples containing Pt amounts of 0.06 wt % or 0.25 wt %. Comparison of the spectra shows that ketone growth rate is significantly higher for the $Pt/Cr/TiO_2$ (0.06%) sample as compared to the $Pt/Cr/TiO_2$ **(**0.25%**)** sample. Although this difference is not straightforward to explain, this result suggests that similar to observed previously [19], metallic Pt is much more effective for promotion of activity of photocatalytic materials, than oxidic Pt.

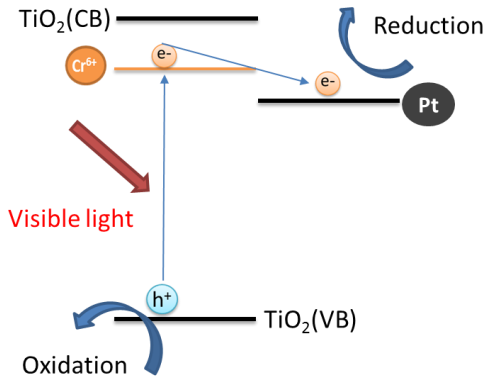

Figure 10: Schematic illustration of the processes occurring upon light activation of $Pt/Cr/TiO_2$.

Figure 10 shows the electron transfer steps possibly occurring upon activation of $Pt/Cr/TiO_2$ (0.06%). The presence of Cr^{6+} creates an intra-band energy level slightly below the conduction band of TiO_2. The Fermi level of metallic Pt (nanoparticles), is well known to be lower in energy than the conduction band (CB) minimum of TiO_2. Visible light excitation, likely excites an electron (e^-) from the conduction band of TiO_2 to the Cr-associated intra band level. This electron will be transferred to the Pt nanoparticles, effectively reducing oxygen. Cr ions thus induce visible light activity, while Pt nanoparticles enhance the photocatalytic efficacy of the Cr/TiO_2 catalyst towards reduction of oxygen. Besides the presence of oxidic Pt, the significantly lower performance of $Pt/Cr/TiO_2$ (0.25%) might be due to unfavorable rapid recombination of electron-hole pairs, which has been previously reported to become dominant at high loadings of Pt nanoparticles.

4. Conclusions

In conclusion, of the dopants investigated (Cu, Pt, V, Cr), Cr is most effective in promoting visible light activity of TiO_2 in the oxidation of MCH, although the selectivity to the ketones is relatively low. The performance of Cr/TiO_2 can be further improved by photodeposition of Pt nanoparticles of 5-10 nm in size, which are likely present in the metallic state. The Apparent Quantum Efficiency (AQE) of the most effective catalyst amounts to 4.5%.

References

[1] K. Hashimoto, H. Irie, A. Fujishima, TiO_2 photocatalysis: A historical overview and future prospects, Jpn J Appl Phys 1, 44 (2005) 8269-8285.
[2] M.A. Henderson, A surface science perspective on TiO_2 photocatalysis, Surface Science Reports, 66 (2011) 185-297.
[3] S.N.R. Inturi, T. Boningari, M. Suidan, P.G. Smirniotis, Visible-light-induced photodegradation of gas phase acetonitrile using aerosol-made transition metal (V, Cr, Fe, Co, Mn, Mo, Ni, Cu, Y, Ce, and Zr) doped TiO_2, Applied Catalysis B: Environmental, 144 (2013) 333-342.
[4] X. Chen, C. Burda, The electronic origin of the visible-light absorption properties of C-, N- and S-doped TiO_2 nanomaterials, Journal of the American Chemical Society, 130 (2008) 5018-5019.
[5] J. Zhang, C. Pan, P. Fang, J. Wei, R. Xiong, Mo^{+} C codoped TiO_2 using thermal oxidation for enhancing photocatalytic activity, ACS Applied Materials and Interfaces, 2 (2010) 1173-1176.
[6] H. Luo, T. Takata, Y. Lee, J. Zhao, K. Domen, Y. Yan, Photocatalytic Activity Enhancing for Titanium Dioxide by Co-doping with Bromine and Chlorine, Chemistry of Materials, 16 (2004) 846-849.
[7] Y. Cong, J. Zhang, F. Chen, M. Anpo, D. He, Preparation, photocatalytic activity, and mechanism of nano-TiO_2 Co-doped with nitrogen and iron (III), Journal of Physical Chemistry C, 111 (2007) 10618-10623.
[8] H.J. Choi, J.S. Kim, M. Kang, Photodecomposition of concentrated ammonia over nanometer-sized TiO_2, V-TiO_2, and Pt/V-TiO_2 photocatalysts, Bulletin of the Korean Chemical Society, 28 (2007) 581-588.
[9] H. Khan, D. Berk, Characterization and mechanistic study of Mo^{+6} and V^{+5} codoped TiO_2 as a photocatalyst, Journal of Photochemistry and Photobiology A: Chemistry, 294 (2014) 96-109.
[10] K. Maeda, Rhodium-doped barium titanate perovskite as a Stable p-type semiconductor photocatalyst for hydrogen evolution under visible light, ACS Applied Materials and Interfaces, 6 (2014) 2167-2173.
[11] P.D. Vaidya, V.V. Mahajani, Studies in hydrotreatment as a unit process to destroy 4-chlorophenol in aqueous stream over Ru-Pd/TiO_2 catalyst, Appl Catal B-Environ, 51 (2004) 21-31.
[12] J. Choi, H. Park, M.R. Hoffmann, Combinatorial doping of TiO_2 with platinum (Pt), chromium (Cr), vanadium (V), and nickel (Ni) to achieve enhanced photocatalytic activity with visible light irradiation, J Mater Res, 25 (2010) 149-158.

[13] J. Choi, H. Park, M.R. Hoffmann, Effects of Single Metal-Ion Doping on the Visible-Light Photoreactivity of TiO_2, Journal of Physical Chemistry C, 114 (2010) 783-792.
[14] A.R. Almeida, M. Calatayud, F. Tielens, J.A. Moulijn, G. Mul, Combined ATR-FTIR and DFT study of cyclohexanone adsorption on hydrated TiO_2 anatase surfaces, Journal of Physical Chemistry C, 115 (2011) 14164-14172.
[15] M.S. Hamdy, R. Amrollahi, G. Mul, Surface Ti^{3+}-Containing (blue) Titania: A Unique Photocatalyst with High Activity and Selectivity in Visible Light-Stimulated Selective Oxidation, ACS Catalysis, 2 (2012) 2641-2647.
[16] R. Amrollahi, M.S. Hamdy, G. Mul, Understanding promotion of photocatalytic activity of TiO_2 by Au nanoparticles, Journal of Catalysis, 319 (2014) 194-199.
[17] Y. Ding, Y. Wang, L. Zhang, H. Zhang, C.M. Li, Y. Lei, Preparation of TiO_2-Pt hybrid nanofibers and their application for sensitive hydrazine detection, Nanoscale, 3 (2011) 1149-1157.
[18] L. Davydov, E.P. Reddy, P. France, P.G. Smirniotis, Transition-metal-substituted titania-loaded MCM-41 as photocatalysts for the degradation of aqueous organics in visible light, Journal of Catalysis, 203 (2001) 157-167.
[19] J.H. Pazmino, M. Shekhar, W.D. Williams, M.C. Akatay, J.T. Miller, W.N. Delgass, F.H. Ribeiro, Metallic Pt as active sites for the water-gas shift reaction on alkali-promoted supported catalysts, Journal of Catalysis, 286 (2012) 279-286.

Appendix

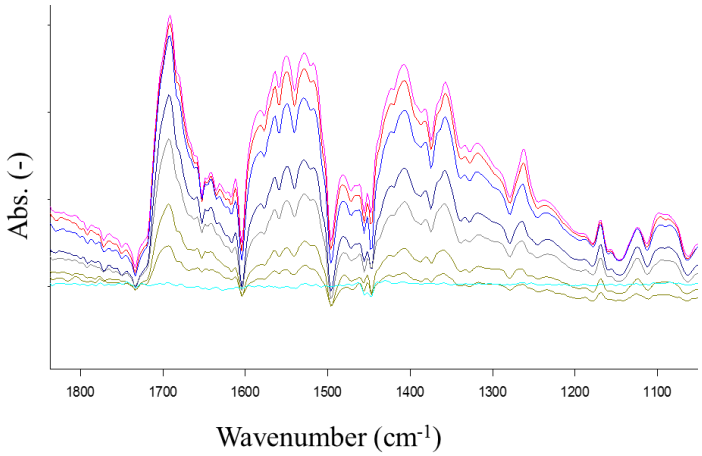

Figure A1: ATR-FTIR spectra of MCH oxidation using Pt/Cr/TiO_2 (0.25%) and illumination at 425 nm (visible light), recorded from 0 min to 100 min.

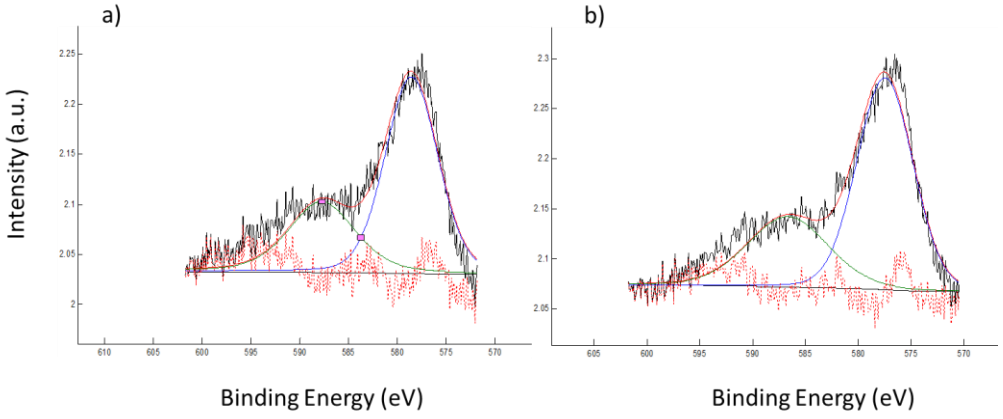

Figure A2: Deconvoluted XPS spectra of the Cr 2p peak for a) Pt/Cr/TiO_2 (0.06%) and b) Pt/Cr/TiO_2 (0.25%)

Chapter 6

Room temperature selective (photo) catalytic oxidation of ethanol to acetaldehyde over Pt/WO_3

Pt/WO_3 catalysts show activity in oxidative dehydrogenation of ethanol at room temperature in the absence or presence of UV light, as determined by gas phase analysis and DRIFT spectroscopy. The nature of the active phase was determined by variations in catalyst preparation methodology, and characterization by Raman and X-ray photoelectron spectroscopy (XPS), before and after reaction. Raman spectroscopy revealed that significant changes in crystal structure and oxidation state of WO_3, potentially induced by the reaction, were absent. XPS data showed that Pt^0 rather than PtO is necessary to induce the selective oxidation of ethanol to acetaldehyde and H_2O. Since Pt on TiO_2 catalysts, and WO_3 were inactive in the experimental conditions, we propose the activity is related to sites at the interface between metallic Pt and WO_3. To the best of our knowledge this is the first time 'dark' catalytic activity of Pt nanoparticles was observed at room temperature.

Keywords: Tungsten oxide, platinum, ethanol oxidation, IR spectroscopy, photocatalysis

This chapter is based on: R. Amrollahi, K. Wenderich, G. Mul; "Room temperature selective (photo) catalytic oxidation of ethanol to acetaldehyde over Pt/WO_3" submitted to ACS Applied Materials and Interfaces.

1. Introduction

WO_3 has interesting properties for use in many applications, including photocatalysis aimed at the decomposition of organic pollutants [1-3], such as alcohol [4] and other gases [5]; or photocatalysis as a technology for storage of solar energy by CO_2 reduction [6], or water splitting [7]. WO_3 has an outstanding stability, good electron transport properties and a high photon induced catalytic activity [8]. Besides in photocatalysis, WO_3 is used in electrochromic displays [9], gas sensors [10, 11], solar energy devices [12] and field-emission devices [13]. Several methods, including thermal evaporation [14], electrochemical techniques [15], spray pyrolysis approaches [16], sol-gel processes [17] and hydrothermal reactions [18] have been reported for synthesis of WO_3 (nano)particles. To enhance performance of WO_3, in particular in sensing and photocatalytic applications, functionalizing of the material with noble metals such as Pt, Au, and Pd has been demonstrated to be effective [19, 20]. However, in both sensing of alcohol concentrations in aerobic conditions, as well as in gas phase photocatalytic oxidation of alcohols, little is known in relation to the oxidation state of the most active Pt particles, and the molecular transformations of ethanol upon interaction with the catalyst surface.

Here we report such insight on the origin of the promotional effect of Pt nanoparticles on the activity of WO_3 in the conversion of ethanol. The relative rates in the presence or absence of light induced by both WO_3 and Pt/WO_3 are shown. Furthermore, by means of Diffuse Reflectance Infrared spectroscopy (DRIFTS), we have analyzed the formation rate of surface intermediates for WO_3 or Pt/WO_3. The structure and oxidation state of highly effective Pt, as well as the surface chemistry involved in the oxidation of ethanol will be discussed.

2. Experimental Section

2.1. Catalyst preparation

All chemicals of analytical grades were purchased at Sigma-Aldrich. For the impregnation of Pt on commercial WO_3 particles (Aldrich), we refer to earlier published work [21]. In short, to perform impregnation of 2 wt% Pt on WO_3, 30 mL of an aqueous solution containing 0.5 M $H_2PtCl_6 \cdot 6H_2O$ was prepared, followed by addition of 200 mg of WO_3 and 20 mL of water (mQ). The suspension was stirred on a heating plate, which was used to evaporate the solution at a temperature of around 70 ^oC. The remaining gel was collected and treated at 500 ^oC (heating rate

10 K/min) for 3 hours in static air. Then, the sample was allowed to cool down to room temperature. The powder was washed with mQ water and was dried at a temperature of 80 ^oC in static air. The sample obtained this way was labeled Pt/WO_3 (imp).

For the synthesis of a coating of either WO_3 or Pt/WO_3 on glass plates, the obtained material (150 mg) was suspended in 3 mL mQ water and adjusted to a pH of 2 by drop-wise addition of HCl (0.1 M). Then the suspension was stirred for 30 min. The suspension (0.75 ml) was drop-casted on the glass substrates and water was removed overnight under vacuum in a desiccator containing silica gel. Each glass substrate contained approximately 37.5 mg of catalyst.

2.2. Preparation of PtO/WO_3 (labeled PD) by photo deposition

PtO/WO_3 (PD) (aimed at 10 wt %) was synthesized by a photo deposition (PD) method. For this synthesis, an aqueous suspension of commercial WO_3 (50 g L^{-1}) in chloroplatinic acid (H_2PtCl_6, 0.5 g L^{-1}) was stirred for 30 minutes in the dark. The suspension was subsequently illuminated at an intensity of 3.2 mW cm^{-2} at 375 nm for 5 hours. The powder was obtained by centrifugation, and washed three times with mQ water. Finally the powder was dried at 80 ^oC overnight. The sample obtained this way was labeled PtO/WO_3 (PD).

2.3. Catalyst characterization

TEM imaging of the Pt/WO_3 (imp) sample was performed using a Philips CM300ST-FEG microscope equipped with a Kevex EDX detector. Samples for TEM analysis were prepared by making a dispersion in ethanol, and deposition onto a carbon coated TEM grid.

X-ray photoelectron spectroscopy (XPS) was conducted using a Quantera SXM spectrometer made by Physical Electronics. The radiation was provided by a monochromatized Al Kα (1486.6 eV) X-ray source, operated at a 25 W emission power and a 15 kV acceleration voltage.

The samples prepared on the glass plate were analyzed by Raman spectroscopy before and after reaction. Raman spectroscopy was performed at room temperature using a Bruker Senterra spectrometer by exposure of the sample to light of 532 nm (20 mW). Spectra were acquired at a resolution of ~15 cm^{-1} and 10 scans were accumulated to obtain each spectrum.

2.4. *The photocatalytic reactor*

The prepared samples on glass plates were placed at the bottom of a batch reactor (2ml) equipped with a quartz window. As illumination source, a 365 nm LED (Roithner Laser Technik, Austria, APG2C1-375-S) was used with a maximum possible light intensity of 8 mW/cm^2 at the catalyst coating. The reactor was operated in batch mode, after 30 ml/min of a predefined mixture was fed, prepared by a combination of N_2 flow and ethanol evaporation. Subsequently two valves were used to close the reactor, and illumination was initiated. Typically an ethanol concentration of 1.73 vol. % was used. After various time intervals of illumination (0 to 50 min), the entire gas composition present in the reactor was purged by He flow onto a Varian CP7584 column coupled to a Methanizer–FID combination for detection of acetaldehyde and CO_2, both present in an Agilent 7820 GC system [22].

The reaction rate was calculated from the concentration of acetaldehyde (Acd) as a product determined after 50 minutes of exposure to light.

$$r = \frac{P_{tot} \cdot X_{Acd} \cdot V}{R \cdot T} \cdot \frac{1}{m} \cdot \frac{60}{t} \qquad (1)$$

$$X_{Acd} = \frac{Acd - Acd_{(dark)}}{10^6} \qquad (2)$$

The reaction rate, r (mmol/g/hr) of the thin film was calculated by equation number 1. P_{tot} is the pressure in the reactor (10^5 Pa) and V is the volume of the bath reactor (2×10^{-6} m^3). R is the gas constant (8.314 m^3 Pa/mol K), m is the catalyst mass (37.5 mg) and t is the reaction time (50 min). X_{Acd} is the quantity of produced acetaldehyde in the gas composition after 50 minutes, and was obtained by equation number 2. Acetaldehyde (Acd) and Acd $_{(dark)}$ were measured concentrations in ppm [22].

2.5. In situ DRIFT spectroscopy

Photocatalytic ethanol oxidation was analyzed by infrared (IR) spectroscopy using a Bruker Vertex 70 spectrometer equipped with a liquid N_2-cooled MCT detector, and a Harrick Praying Mantis diffuse reflectance accessory containing a high temperature cell equipped with a three-window dome. One window (quartz) allowed the illumination of the catalyst with UV/Vis light, while two CaF_2 windows provided

an optical path for infrared analysis. Prior to the illumination experiments, 30 mg of the WO_3 or Pt/WO_3 catalyst was introduced in the sample cup of the accessory. After enclosure of the catalyst in the sample cup by the dome, a flow of 20 mL/min of dry air saturated with ethanol was introduced. After exposure of the catalyst to this flow for 10 min, the lines to the cell were closed. A spectrum was recorded of this state of the catalyst after 1 min, to serve as a background for the series recorded during dark reaction or under illumination. In situ DRIFT spectra were recorded between 0 and 50 min in the absence or presence of irradiation. As illumination source, a 365 nm LED was used with a maximum light intensity of 8 mW/cm^2 at the catalyst surface.

2.6. Hydrogen treatment

Some experiments were also performed using pre-reduction of the Pt catalyst. In scheme 1 the experimental process of the hydrogenation of Pt/WO_3 (H-Pt/WO_3 (imp)) is shown, before *in situ* DRIFT spectra of ethanol adsorption and reaction were recorded. First purging took place with 20 mL/min of He to remove O_2 from the DRIFT cell. Afterwards the samples were reduced at 250 °C (10 K/min) in H_2 (5% H_2/95% He) for 30 min. Then He was used to flush out H_2, and the temperature was decreased to room temperature in He. The sample obtained this way was labeled H-Pt/WO_3 (imp). Subsequently 20 mL/min of air and ethanol were introduced in the cell. During this step, first a background spectrum was measured. Next, the IR spectra were collected without the use of illumination as a function of time. Afterwards, a second background was measured and then IR spectra were recorded during illumination.

For XPS measurement of thermally reduced Pt/WO_3 (imp), this material was introduced in a tube oven, and heated to 250°C (10 K/min) overnight in a 5% H_2/95% N_2 atmosphere.

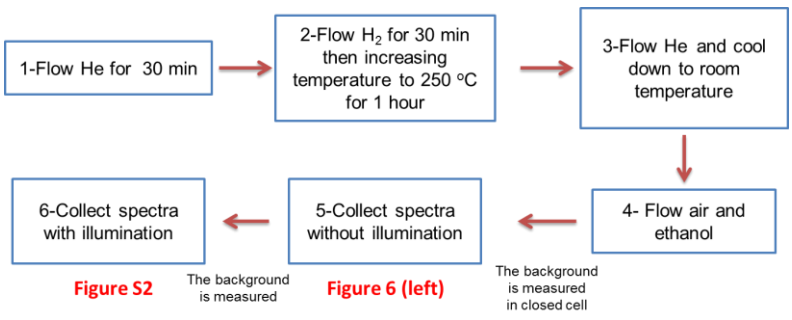

Scheme 1: The experimental procedure of the hydrogenation of Pt/WO_3 (H-Pt/WO_3 (imp)).

3. Results

Figure 1 illustrates TEM images of Pt/WO_3 (imp). Pt nanoparticles are present with an average size of 2.66 nm, with the smallest particles being 1.14 nm, and the largest approximately 4.69 nm. The images show that Pt nanoparticles exist as hemispherical deposits. Furthermore, clusters of Pt particles can be identified on specific domains of WO_3.

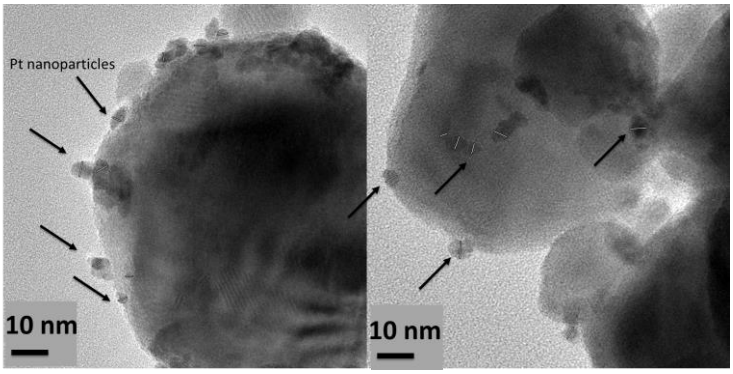

Figure 1: TEM images of Pt/WO_3 (imp)

It also appears that isolated Pt particles are present in other domains of the WO_3 particles. Figure A4 shows other TEM images from the same sample, corroborating the size of the particles, and the domains of clustered and isolated Pt particles.

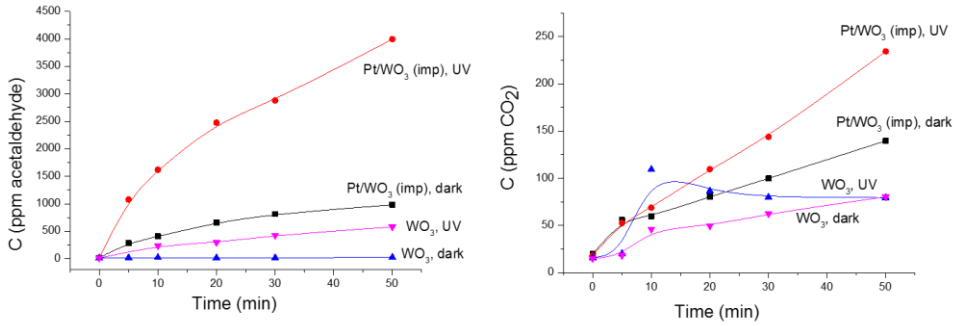

Figure 2: Concentration of products vs reaction time for ethanol oxidation over Pt/WO_3 (imp) and WO_3 in the absence or presence of illumination by a 365 nm LED source. (Left) acetaldehyde and (Right) CO_2. The product composition was measured by GC analysis.

3.1. Ethanol oxidation reaction

The obtained product distributions of the oxidation of ethanol as a function of time (reaction in dark or illumination) are shown in Figure 2. Oxidation of ethanol catalyzed by Pt/WO_3 yields a significant gas phase concentration of acetaldehyde. A very small amount of CO_2 was formed as detected by the GC analysis.
Remarkably, the quantities of acetaldehyde and CO_2 produced by WO_3 were significantly smaller than in the case of Pt/WO_3. The addition of Pt thus results in both a higher acetaldehyde production rate, and a significantly higher rate in formation of CO_2. Surprisingly, for Pt/WO_3, acetaldehyde formation was observed as well without any illumination. This phenomenon was not observed for WO_3.

The acetaldehyde amounts observed, allow for calculation of a rate of around 0.01 mmol/g/hr over Pt/WO_3 (imp) at 365 nm, using equation 1. Also, given the used light intensity, an apparent quantum efficiency of 1.25% to acetaldehyde can be calculated, defined as the amount of moles produced (per hour), divided by the amount of photons which entered the reactor (8×10^{-5} einsteins/h at 365 nm). These

values are in the same order of magnitude as normally observed in photocatalytic conversion using catalyst coatings based on TiO_2 [23].

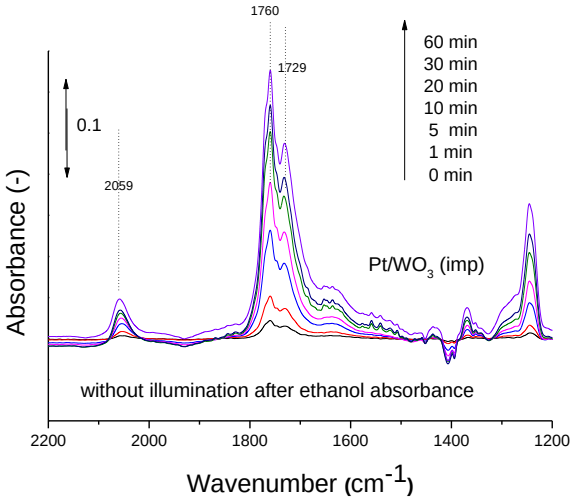

Figure 3: Time resolved DRIFT spectra in the 2200–1200 cm^{-1} region obtained during oxidation of ethanol over Pt/WO_3 (imp) in the dark.

3.2. Surface chemistry

The analysis of the surface chemistry occurring during the oxidation of ethanol over Pt/WO_3 is shown in Figure 3 as a function of reaction time (from 0 to 60 min). The *in situ* DRIFTS spectra were obtained in the absence of illumination. Two strong bands grow in at 1760 and 1729 cm^{-1}. The 1729 cm^{-1} band is assigned to the ν (C=O) vibration of acetaldehyde [22, 24]. The 1760 cm^{-1} is likely the result of ester formation, by consecutive reaction of the intermediate formate with ethanol (formyl acetate) [22]. This also might explain why the oxidation of ethanol over Pt/WO_3 does not result in the formation of significant amounts of carboxylate or carbonate species (intensities of peaks between 1550 and 1400 cm^{-1} are very low). At 1650 cm^{-1}, a broad feature is observed, which might be assigned to water (the bending mode). Moreover, CO adsorbed on Pt is formed, explaining the band at 2059 cm^{-1}, which is growing as a function of increasing time of reaction [25].

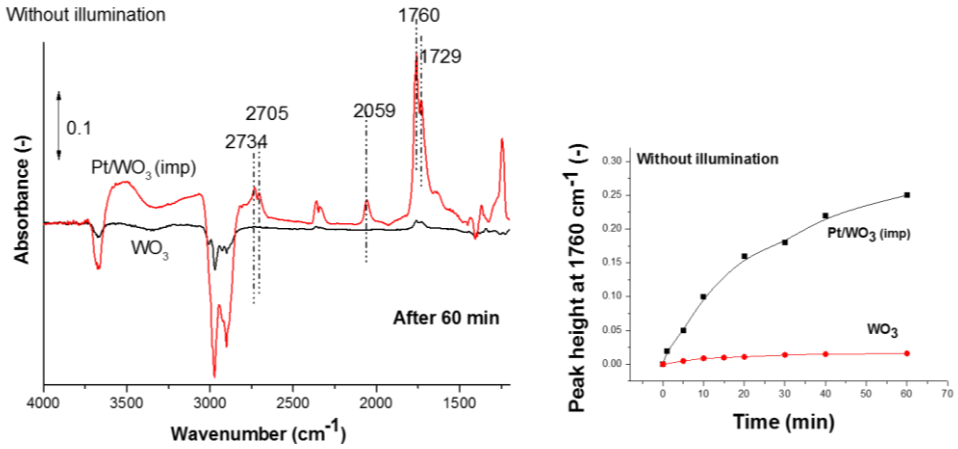

Figure 4: (Left) DRIFT spectra obtained after 60 minutes of oxidation of ethanol without illumination over Pt/WO_3 (imp) and WO_3. (Right) Development of peak height at 1760 cm^{-1} as a function of time for the same experiments.

The spectra obtained after 60 minutes of catalytic oxidation of ethanol over Pt/WO_3 (imp) and WO_3 are compared in Figure 4. The observed peaks at 2734 and 2705 cm^{-1} are again indicative of the formation of acetaldehyde [24].

Comparison of the spectra shows that the activity is significantly increased by adding Pt to WO_3, in agreement with the gas phase results shown in Figure 2. Comparison of the peak heights as a function of time (Figure 4 (right)) is also in agreement with the difference in activity observed between the two samples.

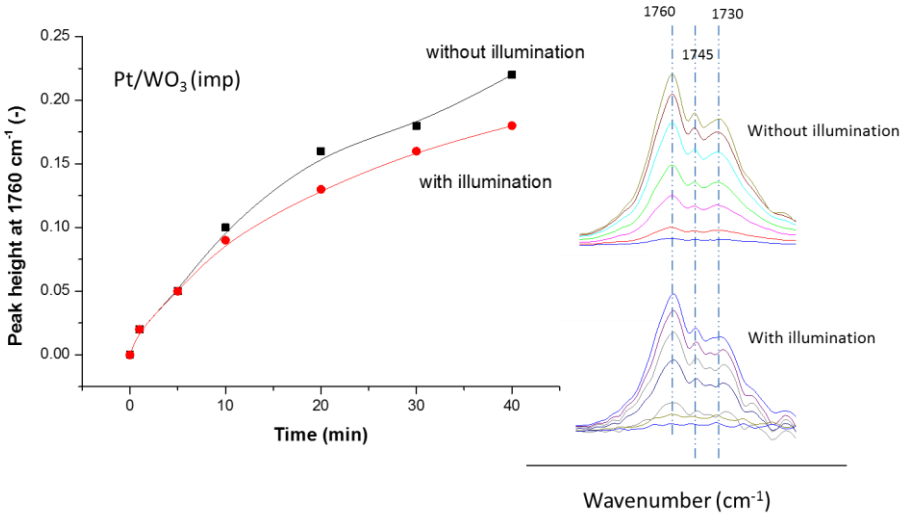

Figure 5: (Left) Peak height at 1760 cm^{-1} as a function of time over Pt/WO_3 (imp) with and without UV illumination for oxidation of ethanol (Right) DRIFT spectra.

To validate the different surface reaction rates induced by either UV illumination or in the dark for Pt/WO_3, we show the rate of development of the intensity of the formyl acetate band at 1760 cm^{-1} as a function of time in Figure 5. We also show in this figure the spectral data. Both reaction conditions initially result in a similar growth rate of the main acetaldehyde peak, but without illumination the surface concentration of acetaldehyde becomes slightly higher beyond a reaction time of 10 minutes.

To determine which oxidation state of Pt is responsible for enhancement of the rate, in situ hydrogenation of the impregnated sample was performed. Afterwards the activity was again determined in oxidation of ethanol. The experiment of H-Pt/WO_3 (imp) (presumably containing 100% of Pt^0) is compared to the sample obtained after the impregnation procedure (Pt/WO_3 (imp)) in Figure 6.

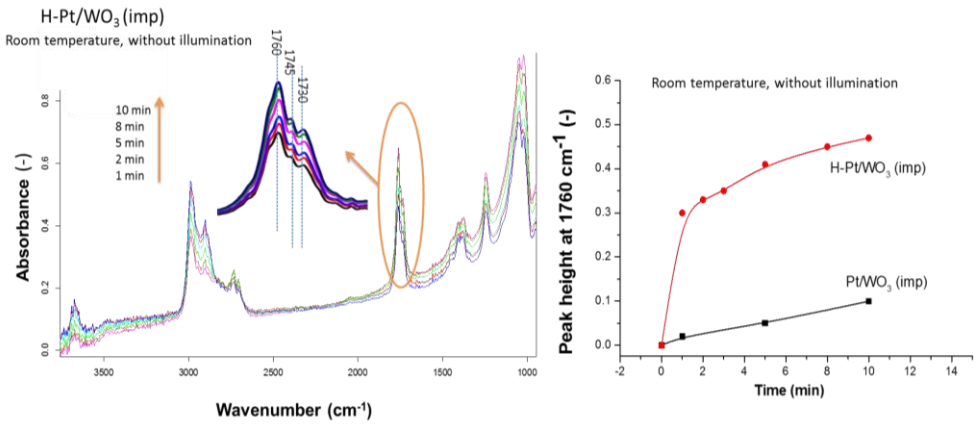

Figure 6: (Left) In situ DRIFT spectra obtained from 0 to 10 min during oxidation of ethanol without illumination over H-Pt/WO_3 (imp) (Right) Peak height at 1760 cm^{-1} as a function of time for the same experiments, now compared to Pt/WO_3 (imp).

Figure 6 (left) shows DRIFT spectra for H-Pt/WO_3 (imp) from 0 to 10 min during ethanol oxidation in the dark. Similar to Figure 4, acetaldehyde formation was observed. Bands located at the 1760, 1745 and 1730 cm^{-1} appear already after 1 min and progressively grow in intensity. Figure 6 (right) shows the development of the peak height at 1760 cm^{-1} for the hydrogenated sample, in comparison to the sample obtained after impregnation. The amount of products formed by oxidation is 4 times higher after hydrogenation of the catalyst, suggesting the metallic state of Pt is essential for the observed reactivity.

In situ DRIFT spectra measured from 0 to 50 min during illumination (the last spectrum of Figure 6 (left) was used as the background) are shown in Figure A2. Only negative features can be observed in the spectra, assigned to light induced desorption of acetaldehyde, of which the rate is apparently larger than the formation of species induced by further oxidation of ethanol.

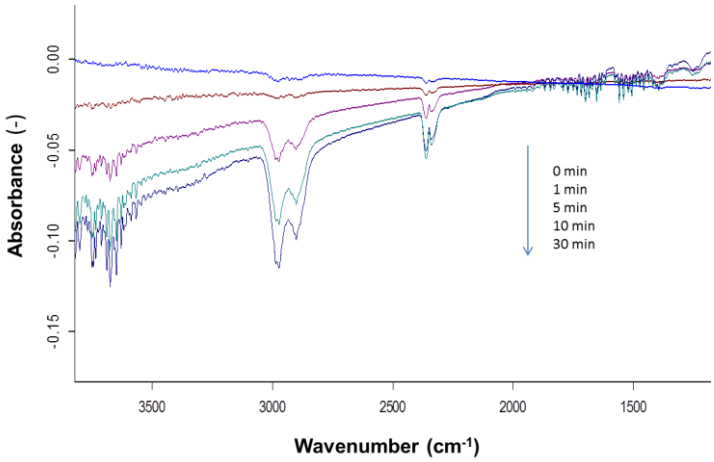

Figure 7: *In situ* DRIFT spectra obtained from 0 to 30 min during exposure of PtO/WO_3 (PD) to ethanol for 30 minutes. The catalyst was synthesized by the photo deposition method in the absence of methanol.

Figure 7 shows in situ DRIFT spectra obtained from 0 to 30 min during oxidation of ethanol with UV illumination over PtO/WO_3 (PD), synthesized by photo deposition in the absence of methanol (PD), which is known to result in the formation of predominantly PtO on the WO_3 surface. Dark activity was completely absent, and illumination only resulted in desorption of ethanol from surface. This experiment confirms the necessity of the presence of metallic Pt to induce the observed oxidation reactions.

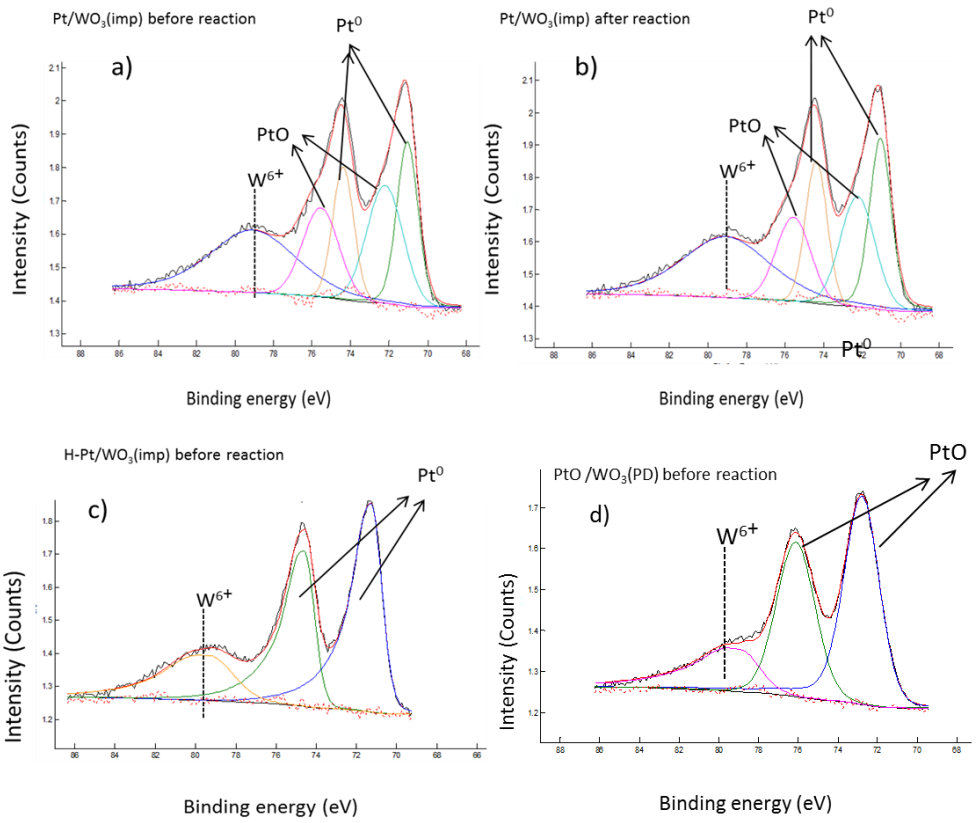

Figure 8: The platinum Pt4f XPS spectral region of Pt/WO_3 (imp) samples, before (a) and after (b) ethanol oxidation with illumination; and H-Pt/WO_3 (imp) before reaction (c); and PtO/WO_3 (PD) before reaction (d)

XPS spectra were recorded to determine the oxidation state of the Pt before and after reaction for Pt/WO_3 (imp). The results are shown in Figure 8-a and 8-b for the Pt4f region (70–79 eV). Figure 8-c and 8-d show XPS spectra of H-Pt/WO_3 (imp) and PtO/WO_3 (PD), respectively, for comparison and both measured before reaction. Figure 8-a and 8-b demonstrate two doublets located at 71.05 and 74.38 eV, which are attributed to metallic Pt^0, and at 72.22 eV and 75.55 eV, corresponding to an oxidation state of Pt^{2+} [26]. The Pt^{2+} species could exist or coexist in the form of PtO or $PtCl_2$. Since a Cl signal was not observed in the XPS spectra, the presence of Pt^{2+} is most likely related to PtO. The ration of oxidized platinum *vs* metallic platinum was found to be approximately unity. The broad XPS peak at 79.05 eV corresponds to W^{6+}, showing changes in oxidation state of W^{6+} during synthesis or

reaction are not very likely. H-Pt/WO_3 (imp) only shows the Pt^0 state (Figure 8-c), and in case of PtO/WO_3 (PD), only PtO without significant amounts of metallic Pt (Figure 8-d) are detected.

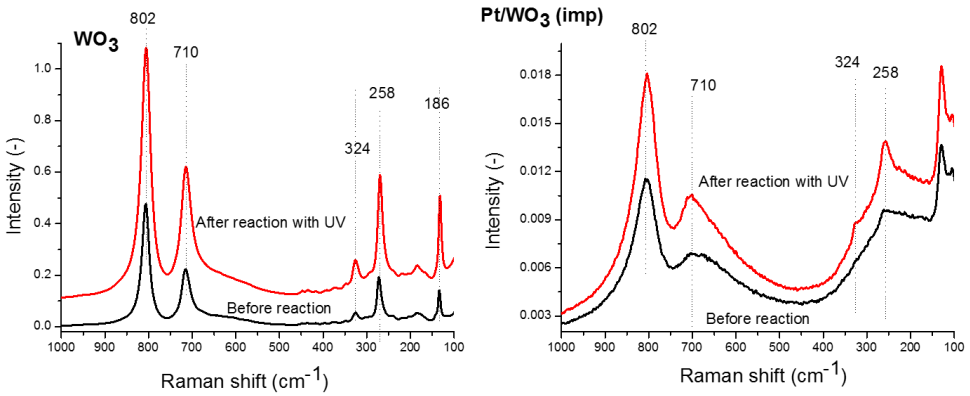

Figure 9: Raman spectra for WO_3 (Left) and Pt/WO_3 (imp) (Right) before and after illumination (using a 365 nm LED) in the presence of ethanol and oxygen.

To analyze the WO_3 phase in more detail, Raman spectra were measured. Figure 9 shows Raman spectra of WO_3 (left) and Pt/WO_3 (imp) (right) before and after reaction. In Figure 9 (left), five well-resolved peaks at 129, 258, 324, 710 and 802 cm^{-1} can be observed. Peaks centered at 710 and 802 cm^{-1} are attributed to W-O-W stretching modes, and the three peaks at smaller Raman shift at 129, 258 and 324 cm^{-1} are induced by W-O-W bending vibrational modes [13]. Compared to WO_3, Pt/WO_3 (imp) shows decreased Raman intensity of 100 times (Figure 9), showing light reflectivity has significantly decreased. The peaks are also considerably broader. This might be due to electronic interactions or electron transfer from Pt nanoparticles to WO_3 [27], but this requires further investigation.

4. Discussion

WO_3 and Pt/WO_3 have been studied with respect to many fields of application, including gas sensing [11] and photo- [28, 29] and electrocatalysis [30]. As a photo-electrocatalyst, Pt/WO_3 has been studied in conversion of methanol [31].

The main achievement of this research is the observation of dark activity for Pt/WO_3 in oxidation of ethanol to acetaldehyde and surface bound products such as formyl acetate. The presence of metallic Pt was found essential for activity, as a result of comparing H-Pt/WO_3, Pt/WO_3 (imp) and PtO/WO_3 (PD) in activity, and analysis of these samples by XPS. To the best of our knowledge, this is the first time such dark activity has been reported for this material. The activity is quite remarkable, since in case of Pt/TiO_2, no dark activity was detected in identical experimental conditions [22]. Since also WO_3 in the absence of Pt did not show any activity, we propose that the interface between metallic Pt and WO_3 is an important factor to explain the photocatalytic and dark activity. In the following we will discuss the implications of this finding for the use of Pt/WO_3 as a gas sensor, or (gas phase) photocatalyst for ethanol conversion in more detail, while we realize that the concentration of ethanol used in this study, needed to obtain sufficient sensitivity in the analyses, is significantly higher than typically relevant for these fields of application.

To the best of our knowledge, the basis for sensing applications lies in the observation of a resistivity change of the semiconductor (WO_3) upon interaction of the surface with the gas molecules to be detected. Sermon et al. have nicely summarized what interactions with gases (in their case H_2S) and the surface, might lead to measureable signals [32], two of which are relevant for our study: (i) simple adsorption with electron donation to the oxide conduction band; (ii) dissociation of H_2S, which may produce atomic hydrogen to which the trioxide might respond; and (iii) direct combustion of H_2S on the oxide. The first explanation is usually not very likely, since selectivity in sensing applications is then hard to explain. Moreover, on the basis of our results, simple (non-reactive) surface interactions appear not feasible, even at room temperature, given the significant surface yield of oxidized products. Regarding the second explanation, dissociation of ethanol would produce exclusively acetaldehyde (and hydrogen), whereas we observe extensive formation of oxidized products involving reaction with oxygen. Therefore, we propose sensing of ethanol in aerobic conditions is most likely related to explanation iii), direct combustion. This is also in agreement with the need for Pt to achieve significant ethanol conversion and one of the proposed sensing mechanisms by Zhang et al. [27]

Pt is likely needed to create atomic oxygen, which through a spill-over mechanism might induce combustion of surface bound ethanol, which we demonstrate leads to acetaldehyde and formate formation, and consecutive oxidation products thereof (e.g. formyl acetate, CO and CO_2). We propose this most likely occurs at the interface of the noble metal and the metal oxide (WO_3 here). From TEM images (Figure 1), we observe Pt nanoparticles indeed strongly interact with the WO_3 surface, which should be beneficial for activity. Also, the small particle sizes of the Pt nanoparticles improve the rate of the spillover effect [27]. The importance of the presence of O_2 for the reaction is also shown in Figure A3. In the absence of O_2 (surface bound) products of ethanol oxidation over Pt/WO_3 (imp) could not be observed.

Platinized WO_3 has also been applied in photocatalytic conversion of alcohols. For example Aminian et al. [4] have analyzed performance in oxidation of isopropyl alcohol (IPA), and show some spontaneous oxidation in producing acetone occurs over the catalyst surface in the dark. However, this activity is significantly smaller than observed in our study on ethanol oxidation. Further, Aminian et al. [4] do not discuss the surface chemistry in detail, and did not observe CO or CO_2 formation in the dark. Interestingly, these authors found a dramatic effect of the WO_3 morphology on the photocatalytic rates, which is in agreement with our hypothesis that interfacial phenomena between the Pt nanoparticles and the WO_3 might be relevant in explaining the remarkable activity of this material observed in alcohol oxidation.

Based on our observations, the role of light in stimulating the reaction is proposed to be beyond the commonly advocated mechanism in which an excited conduction band electron stimulates oxygen reduction, and the hole induces formation of reactive intermediates (OH radicals, or intermediate radicals formed by oxidation of the substrate (ethanol)). Light has very little effect on promoting the rate of formation of surface adsorbed species, whereas a significant effect was observed in forming gas phase acetaldehyde. We therefore propose that light stimulates desorption of oxidized intermediates from the catalyst surface. This is in agreement with Figure A2, which shows light stimulates desorption of acetaldehyde, previously formed by reaction of ethanol in the dark. The origin of light induced desorption might be related to changes in surface charge, surface hydration, or enhancement in temperature. These phenomena are currently further investigated in our laboratories.

5. Conclusion

Pt/WO_3 catalysts were found to be effective in the oxidative dehydrogenation of ethanol to acetaldehyde. The activity of these materials depends strongly on the nature of the Pt species. PtO containing WO_3 is completely ineffective for the reaction. By impregnation, a significant fraction of Pt was formed (approximately 50% of Pt was in the metallic state) and this resulted in an effective catalyst. The activity could be further improved by hydrogenation of the impregnated sample, which resulted exclusively in metallic Pt as confirmed by XPS analysis. The remarkably high activity of the Pt/WO_3 is likely related to interfacial synergy between the Pt particles and the WO_3 surface. The rate of formation of surface adsorbed acetaldehyde was not much affected by the absence or presence of light, while the gas phase production rate was significantly higher in the presence of light. We propose this is due to light stimulated desorption of the product acetaldehyde.

References

[1] Y. Shiraishi, Y. Sugano, S. Ichikawa, T. Hirai, Visible light-induced partial oxidation of cyclohexane on WO_3 loaded with Pt nanoparticles, Catalysis Science and Technology, 2 (2012) 400-405.
[2] J. Kim, C.W. Lee, W. Choi, Platinized WO_3 as an environmental photocatalyst that generates OH radicals under visible light, Environmental Science and Technology, 44 (2010) 6849-6854.
[3] O. Tomita, B. Ohtani, R. Abe, Highly selective phenol production from benzene on a platinum-loaded tungsten oxide photocatalyst with water and molecular oxygen: selective oxidation of water by holes for generating hydroxyl radical as the predominant source of the hydroxyl group, Catal Sci Technol, 4 (2014) 3850-3860.
[4] M.K. Aminian, J.H. Ye, Morphology influence on photocatalytic activity of tungsten oxide loaded by platinum nanoparticles, J Mater Res, 25 (2010) 141-148.
[5] S.B. Sadale, K. Noda, K. Kobayashi, K. Matsushige, Hydrogen production from gas phase photocatalytic decomposition of methanol using Pt-supported nanocrystalline WO_3 films, Phys Status Solidi C, 8 (2011).
[6] X.Y. Chen, Y. Zhou, Q. Liu, Z.D. Li, J.G. Liu, Z.G. Zou, Ultrathin, Single-Crystal WO_3 Nanosheets by Two-Dimensional Oriented Attachment toward Enhanced Photocatalystic Reduction of CO_2 into Hydrocarbon Fuels under Visible Light, Acs Appl Mater Inter, 4 (2012) 3372-3377.
[7] K. Sayama, K. Mukasa, R. Abe, Y. Abe, H. Arakawa, A new photocatalytic water splitting system under visible light irradiation mimicking a Z-scheme mechanism in photosynthesis, Journal of Photochemistry and Photobiology A: Chemistry, 148 (2002) 71-77.
[8] Y. Tae Kwon, K. Yong Song, W. In Lee, G. Jin Choi, Y. Rag Do, Photocatalytic behavior of WO_3-loaded TiO_2 in an oxidation reaction, Journal of Catalysis, 191 (2000) 192-199.
[9] Y.-M. Lu, C.-P. Hu, The colored and bleached properties of tungsten oxide electrochromic films with different substrate conductivities, Journal of Alloys and Compounds, 449 (2008) 389-392.
[10] I. Jiménez, J. Arbiol, G. Dezanneau, A. Cornet, J.R. Morante, Crystalline structure, defects and gas sensor response to NO_2 and H_2S of tungsten trioxide nanopowders, Sensors and Actuators B: Chemical, 93 (2003) 475-485.
[11] X.L. Li, T.J. Lou, X.M. Sun, Y.D. Li, Highly sensitive WO_3 hollow-sphere gas sensors, Inorganic Chemistry, 43 (2004) 5442-5449.
[12] H. Zheng, Y. Tachibana, K. Kalantar-Zadeh, Dye-sensitized solar cells based on WO_3, Langmuir, 26 (2010) 19148-19152.

[13] C.Y. Su, H.C. Lin, C.K. Lin, Fabrication and optical properties of Ti-doped W18O 49nanorods using a modified plasma-arc gas-condensation technique, Journal of Vacuum Science and Technology B: Microelectronics and Nanometer Structures, 27 (2009) 2170-2174.
[14] A. Ponzoni, E. Comini, M. Ferroni, G. Sberveglieri, Nanostructured WO_3 deposited by modified thermal evaporation for gas-sensing applications, Thin Solid Films, 490 (2005) 81-85.
[15] S.H. Baeck, K.S. Choi, T.F. Jaramillo, G.D. Stucky, E.W. McFarland, Enhancement of photocatalytic and electrochromic properties of electrochemically fabricated mesoporous WO_3 thin films, Advanced Materials, 15 (2003) 1269-1273.
[16] O. Arutanti, T. Ogi, A.B.D. Nandiyanto, F. Iskandar, K. Okuyama, Controllable crystallite and particle sizes of WO_3 particles prepared by a spray-pyrolysis method and their photocatalytic activity, AIChE Journal, 60 (2014) 41-49.
[17] S. Badilescu, P.V. Ashrit, Study of sol-gel prepared nanostructured WO_3 thin films and composites for electrochromic applications, Solid State Ionics, 158 (2003) 187-197.
[18] S. Salmaoui, F. Sediri, N. Gharbi, Characterization of h- WO_3 nanorods synthesized by hydrothermal process, Polyhedron, 29 (2010) 1771-1775.
[19] M. Penza, C. Martucci, G. Cassano, NO_x gas sensing characteristics of WO_3 thin films activated by noble metals (Pd, Pt, Au) layers, Sensors and Actuators, B: Chemical, B50 (1998) 52-59.
[20] V. Srivastava, K. Jain, Highly sensitive NH_3 sensor using Pt catalyzed silica coating over WO_3 thick films, Sensors and Actuators, B: Chemical, 133 (2008) 46-52.
[21] K. Wenderich, A. Klaassen, I. Siretanu, F. Mugele, G. Mul, Sorption-determined deposition of platinum on well-defined platelike platelike WO_3, Angewandte Chemie - International Edition, 53 (2014) 12476-12479.
[22] B.D. Fraters, R. Amrollahi, G. Mul, How Pt nanoparticles affect TiO_2-induced gas-phase photocatalytic oxidation reactions, Journal of Catalysis, 324 (2015) 119-126.
[23] M.S. Hamdy, R. Amrollahi, G. Mul, Surface Ti^{3+}-containing (blue) titania: A unique photocatalyst with high activity and selectivity in visible light-stimulated selective oxidation, ACS Catalysis, 2 (2012) 2641-2647.
[24] Z. Topalian, B.I. Stefanov, C.G. Granqvist, L. Österlund, Adsorption and photo-oxidation of acetaldehyde on TiO_2 and sulfate-modified TiO_2: Studies by in situ FTIR spectroscopy and micro-kinetic modeling, Journal of Catalysis, 307 (2013) 265-274.

[25] M.A. Pereira da Silva, R.M. Cardoso, M. Schmal, Propane oxidation on Pt-WO_3/γ-Al2O_3 catalytic systems, Brazilian Journal of Chemical Engineering, 20 (2003) 51-56.
[26] X. Liu, J. Zhang, T. Yang, X. Guo, S. Wu, S. Wang, Synthesis of Pt nanoparticles functionalized WO3 nanorods and their gas sensing properties, Sensors and Actuators B: Chemical, 156 (2011) 918-923.
[27] J. Zhang, X. Liu, M. Xu, X. Guo, S. Wu, S. Zhang, S. Wang, Pt clusters supported on WO_3 for ethanol detection, Sensors and Actuators B: Chemical, 147 (2010) 185-190.
[28] M.B. Johansson, G.A. Niklasson, L. Österlund, Structural and optical properties of visible active photocatalytic WO_3 thin films prepared by reactive dc magnetron sputtering, J Mater Res, 27 (2012) 3130-3140.
[29] O. Arutanti, A.B.D. Nandiyanto, T. Ogi, T.O. Kim, K. Okuyama, Influences of Porous Structurization and Pt Addition on the Improvement of Photocatalytic Performance of WO_3 Particles, Acs Appl Mater Inter, 7 (2015) 3009-3017.
[30] J. Shim, C.R. Lee, H.K. Lee, J.S. Lee, E.J. Cairns, Electrochemical characteristics of Pt-WO3/C and Pt-TiO_2/C electrocatalysts in a polymer electrolyte fuel cell, Journal of Power Sources, 102 (2001) 172-177.
[31] J. Georgieva, S. Sotiropoulos, E. Valova, S. Armyanov, N. Karanasios, Methanol oxidation and photo-oxidation at Pt/WO_3 electrocatalysts on graphite substrates, J Electroanal Chem, 727 (2014) 135-140.
[32] E.P.S. Barrett, G.C. Georgiades, P.A. Sermon, The mechanism of operation of WO_3-based H2S sensors, Sensors and Actuators: B. Chemical, 1 (1990) 116-120.

Appendix

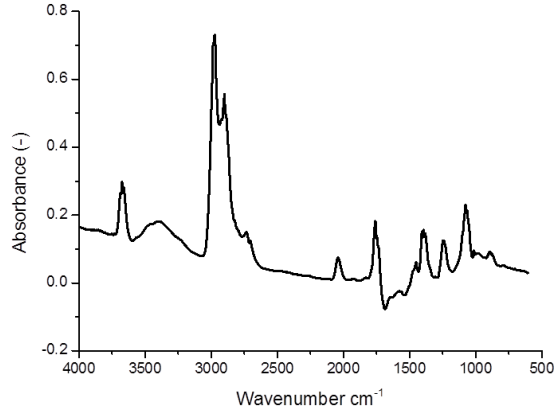

Figure A1: DRIFT spectra of ethanol adsorbed on Pt/WO_3 (imp) obtained after 10 min interaction in the dark.

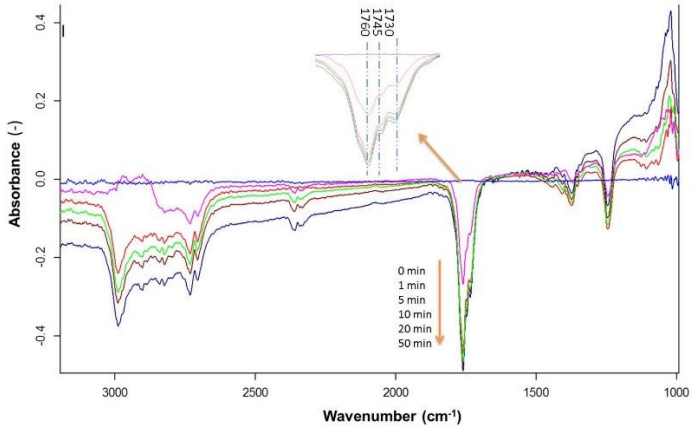

Figure A2: *In situ* DRIFT spectra obtained from 0 to 50 min during illumination of H- Pt/WO_3 (imp). The last spectrum of Figure 6 (left) was used as background, the negative features indicate desorption and conversion of acetaldehyde from the surface.

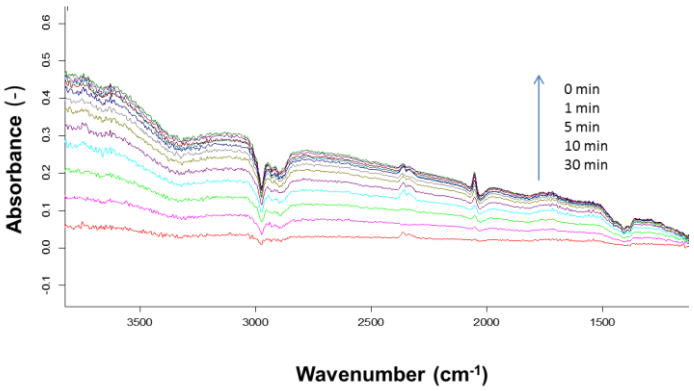

Figure A3: *In situ* DRIFT spectra obtained from 0 to 30 min over Pt/WO_3 (imp). A flow of 20 mL/min of He saturated with ethanol instead of dry air was used for the experiment. Other conditions were the same as the experiment of Figure 3. This experiment shows the importance of O_2 for ethanol conversion.

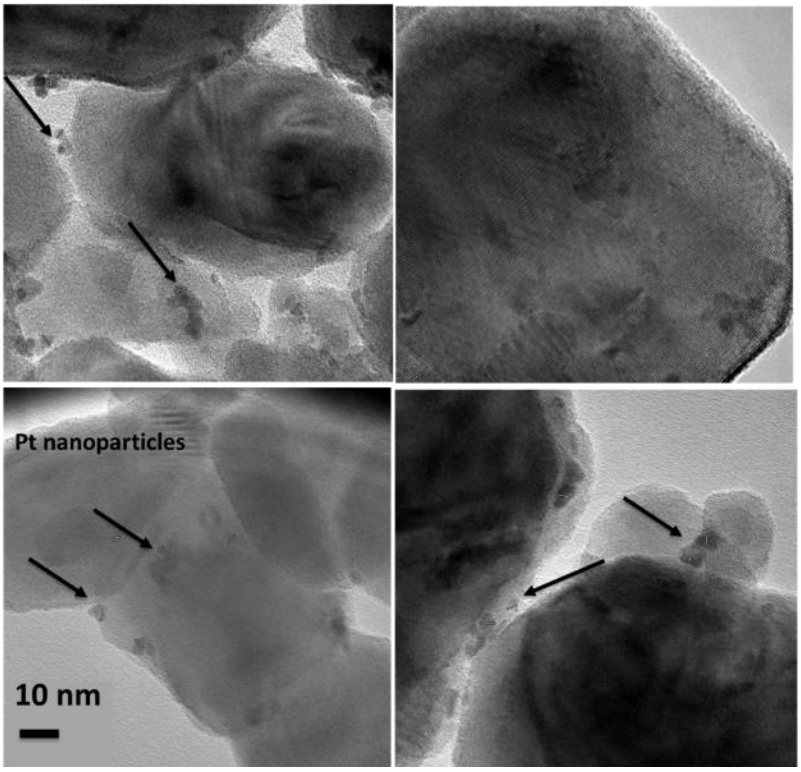

Figure A4: Additional TEM images of Pt/WO_3 (imp). The arrows indicate the presence of Pt.

Chapter 7

Strategies to Design Efficient Silica-Supported Photocatalysts for Reduction of CO_2

The photocatalytic reduction of CO_2 by water vapour to produce light hydrocarbons was studied over a series of catalysts consisting of variable loading of Ti incorporated in TUD-1 mesoporous silica, either modified by ZnO nanoparticles or isolated Cr-sites. Unexpectedly, the performance of ZnO-Ti-TUD-1 and Cr-Ti-TUD-1 was inferior to the parent Ti-TUD-1. An explanation can be found in experiments on the photocatalytic degradation of a mixture of hydrocarbons (i.e. CH_4, C_2H_4, C_2H_6, C_3H_6, and C_3H_8) under the same illumination conditions. Ti-TUD-1 exhibits the poorest activity in hydrocarbons degradation, while ZnO-Ti-TUD-1 and Cr-Ti-TUD-1 showed very significant degradation rates. This study clearly demonstrates the importance of evaluating hydrocarbon conversion over photocatalysts active in converting CO_2 to hydrocarbons (in batch reactors).

This chapter is based on: M. S. Hamdy, R. Amrollahi, I. Sinev, B.Mei, G. Mul; "Strategies to Design Efficient Silica-Supported Photo-catalysts for Reduction of CO_2", Journal of the American Chemical Society (**JACS**), 2014, 136 (2), pp 594–597.

1. Introduction

Over the last decade, the contribution of solar panels to the production of electricity has significantly increased. To compensate for imbalances in energy production and demand and to sustain net stability, it is of eminent importance to create scalable solutions for storage of energy provided by sunlight. A possible route to store solar energy is to directly convert solar light into a fuel. Compared to hydrogen, (liquid) hydrocarbons have the advantage of an existing infrastructure, making production, distribution and application of these environmentally benign solar fuels attractive. Prospective solar to fuel converters require the development of very efficient photocatalysts. Modifications of crystalline TiO_2 based catalysts have been reported extensively in the literature[1-8] to be active in light and water induced photocatalytic reduction of CO_2, including modification by surface Cu-sites [4], or attachment of metallic co-catalyst nanoparticles, such as Ag [8], Pd [7], or Pt [6]. The currently best performing catalysts in direct CO_2 reduction to hydrocarbons, in particular on a per active site basis, are materials containing isolated Ti-sites in silica matrices, pioneered by Anpo and his co-workers in the 1990s [9]. Several silica matrices have been reported effective when hosting Ti-sites, including Zeolites and Mesoporous materials [10-13]. However, implementation of these materials in solar to fuel converters is still impractical, because of the low yields typically achieved with these catalysts [14, 15].

In this chapter, we evaluate three strategies to improve on the current standing of the intriguing catalysts on the basis of Ti-sites in silica matrices. First we adapt the pore structure and improve Ti dispersion by incorporation of Ti-sites in a TUD-1 silica matrix. Second we add ZnO to provide CO_2 adsorption capacity for times sunlight is not available for reaction [16], and third we evaluate the performance of visible light sensitive Cr-O-Ti sites [17, 18]. We provide novel insight in the synergy between isolated Ti and ZnO nanoparticles, as well as CrO_x and TiO_x, not only regarding changes in the apparent CO_2 reduction rates, but in particular by discussing the ability and consequences of the newly created sites to convert hydrocarbons to CO_2, the reverse of the desired process.

2. Experimental methods

2.1. Catalyst preparation

The following chemicals were obtained and used in the synthesis of the catalysts without further treatment: Tetraethyl orthosilicate (TEOS, +98% ACROS), triethanolamine (TEA, 97% ACROS), tetraethylammonium hydroxide (TEAOH, 35% Aldrich), titanium (IV) butoxide (97%, Sigma Aldrich), zinc acetate dihydrate (>98%, Sigma Aldrich) and chromium (III) nitrate nonahydrate (99%, Sigma Aldrich).

Different samples of functionalized TUD-1 were prepared: 1) A series of Ti-TUD-1 (Si/Ti = 1000-10) [19, 20] labelled as Ti-x, where x is the loading % of Ti. 2) A sample of ZnO-Ti-TUD-1, with Si/Ti = 100 and Si/Zn = 10, the sample labeled as Ti1-Zn10. 3) A sample of ZnO-TUD-1 with Si/Zn = 10, and labeled as Zn-10. 4) A sample of Cr-Ti-TUD-1 with Si/Ti = 100 and Si/Cr = 100, the sample labelled as Ti1-Cr1. 5). Finally, a sample of Cr-TUD-1 with Si/Cr ratio = 100 and labeled as Cr-1 [21].

All samples were prepared through the well-established one-pot hydrothermal synthesis procedure described earlier [21]. The synthesis procedure consists of aging, drying, hydrothermal treating, and finally calcining a homogeneous mixture of TEOS, TEA, TEAOH, H_2O and the metal precursors with a molar ratio of 1 SiO_2: 1 TEA: 0.5 TEAOH: 11 H_2O: *x* MO.

2.2. Catalyst characterization

The X-ray diffraction patterns (XRD) were recorded on a Bruker D2 model X-ray diffractometer using Cu K_α radiation (λ=1.54 Å) as the X-ray source operating at 30 kV and 10 mA over the 2θ range of 10-90°.

The diffused reflectance UV-visible spectra (DRS) of the samples were recorded by an UV-vis spectrometer (EVOLUTION 600, Thermal Scientific) with a diffuse reflectance accessory using $BaSO_4$ as reference at room temperature.

Nitrogen adsorption/desorption isotherms were recorded on a Micromeritics Tristar System ASAP 2400 at 77 K. Samples were previously evacuated at 573 K and 10^{-3}

Pa for 24 h. The pore size distribution was calculated from the adsorption branch using the Barret-Joyner-Halenda (BJH) model. The BET method was used to calculate the surface area (S_{BET}) of the samples, while the mesopore volume (V_{meso}) and pore diameter (D_{meso}) were determined using the t-plot method.

X-ray absorption fine structure (XAFS) measurements (Zn *K*-edge, 9659 eV) were carried out at HASYLAB (DESY, Hamburg, Germany) at beamline C using a double-crystal Si(111) monochromator, which was detuned to 65% of maximum intensity to exclude higher harmonics in the X-ray beam. The spectra were recorded in transmission mode at liquid nitrogen temperature to suppress thermal disorder. For the measurements, samples were pressed in self-supporting pellets (13 mm diameter) and wrapped with Kapton tape. All spectra were measured simultaneously with the reference spectrum of a zinc foil placed between second and third ionization chambers. This allowed absolute energy calibration. The spectra of Zn foil and ZnO, which were used as reference, were collected under the same conditions. All spectra were measured 2 times to ensure their reproducibility.

Analysis of the EXAFS spectra was performed with the software VIPER for Windows. In the spectra of the absorption coefficient μ, a Victorian polynomial was fitted to the pre-edge region for background subtraction. A smooth atomic background μ_0 was evaluated using a smoothing cubic spline. The Fourier analysis of the k^2-weighted experimental function $\chi = (\mu-\mu_0)/\mu_0$ was performed with a Kaiser window. The required scattering amplitudes and phase shifts were calculated by the *ab initio* FEFF8.10 code for the Wurtzite ZnO structure. The fitting was done in the *k*- and *r*-spaces. The shell radius *r*, coordination number *N*, Debye-Waller factor σ^2 and adjustable "muffin-tin zero" ΔE were determined as fitting parameters. The errors of the fitting parameters were found by decomposition of the statistical χ^2 function near its minimum, taking into account maximum pair correlations.

TPD measurements were performed in a stainless-steel flow setup equipped with a calibrated online mass spectrometer (Balzers GAM400). In a typical experimental sequence 50 mg of catalyst were placed in a quartz-lined stainless steel U-tube reactor. A thermocouple was placed into the catalyst bed to measure the temperature during the desorption experiments. The sample was pre-treated at 400 °C with a heating ramp of 10 K min^{-1} in 50 NmL min^{-1} 1% O_2/He and then kept at 400 °C for 1 h. After cooling to room temperature the reactor was purged with He, and subsequently CO_2 adsorption was performed with a flow rate of 50 mL min^{-1} 4.1% CO_2/He for 15 min. After purging with He for 30 min the temperature was increased

to 400 °C with a heating ramp of 10 K min^{-1} and held at this temperature for 1 h. During desorption the concentration of CO_2 in He was measured continuously.

High-Resolution Transmission Electron Microscopy (HR-TEM) was carried out on a Philips CM30UT electron microscope with a field emission gun as the source of electrons operated at 300 kV. Samples were mounted on a copper-supported carbon polymer grid by placing a few droplets of a suspension of the ground sample in ethanol on the grid, followed by drying at ambient conditions.

In-situ Diffuse Reflectance Infrared Fourier Transform spectroscopy was carried out using a Bruker Vertex 70 spectrometer equipped with a Liquid N_2 cooled MCT detector, and a three window DRIFTS (Diffuse and Reflectance Infrared Fourier Transform Spectroscopy) cell. Two ZnSe windows allowed IR transmission, and a third (Quartz) window allowed the introduction of UV/Vis light into the cell. Prior to the illumination experiments, 25 mg of the as-synthesized Ti-TUD-1 and Cr-Ti-TUD-1 catalysts were heated up to 393 K in He (30 mL/min) for 0.5 h, in order to remove the majority of adsorbed water. A spectrum was recorded of this state of the catalysts, to serve as background for a spectral series of formaldehyde adsorption. Formaldehyde was introduced in the cell by evaporation of a 10 weight percent formaldehyde water mixture into a flow of 20 mL/min of He. After exposure of the catalyst to this flow for 30 minutes, the lines to the cell were closed, and illumination started. The last spectrum recorded after introduction of formaldehyde served as background for the series recorded during illumination. In-situ IR signals were recorded every 10 min under UV/Vis light irradiation (100 Watt Hg lamp (Dr. Groebel), wavelength range 250 – 600nm)).

2.3. Photocatalytic performance

2.3.1. Catalyst pre-treatment

In order to remove any possible residual carbon [22], the so called moisture/He test was carried out, in which the catalysts were illuminated in a He/water vapor environment. Gas samples were withdrawn and analyzed by GC. This process was continued until zero hydrocarbons were recorded, which is an indication that the sample is clean and ready for the photocatalytic test.

2.3.2. Photocatalytic performance evaluation

The photocatalytic reduction of CO_2 in the presence of H_2O vapor was evaluated in a home-made multi-cell photocatalytic set-up. The set-up consists of 12 identical cylindrical reactors (inner volume 50 mL), which are connected to a sample loop for gas dosage and sampling. The applied light source is a 120W high-pressure mercury lamp with a spectrum ranging from 280 to 650 nm. The reaction was conducted with a ratio 0.5 of CO_2 (38 µmol) over H_2O (76 µmol). All reactors were operated in batch mode and illuminated for 8 h. The production of hydrocarbons was monitored by a compact gas chromatograph equipped with Molsieve 5A and capillary Porabond Q columns connected to a TCD detector (used for separation of H_2, O_2, N_2, CO and CH_4). A second Porabond Q column connected to an FID detector was used for separation and detection of C_1-C_4 alkanes and alkenes. Concentrations were analyzed with an accuracy of ±0.5 ppm. In evaluating the reaction, 100 mg of the catalysts were distributed evenly at the bottom of the reactor to create a uniform layer with a thickness of approximately 1-2 mm. The reactors were evacuated down to 3 mbar and then the CO_2/He mixture saturated with water vapor was introduced. The evacuation/filling cycle was repeated three times, followed by initiation of illumination.

2.3.3. The reusability of the Ti-1 sample

The stability and reusability of the Ti-1 sample was evaluated as follows. The gases produced in the first experiment were removed by evacuation from the reactor, and then a fresh CO_2/H_2O mixture was introduced. This process was repeated six times without any treatment of the catalyst.

2.3.4. Hydrocarbon degradation

The study of hydrocarbon degradation (the backward reactions) was carried out by using a standard gas mixture of 1 volume-% of CH_4, C_2H_4, C_2H_6, C_3H_6, and C_3H_8 in Helium. By dilution, a He stream containing 25 ppm of each component and 4 mol% of water vapor was introduced into the reactors containing the catalyst powders. Evacuation/filling cycles were repeated at least three times before lamp ignition and start of the degradation experiments. The photocatalytic degradation of the gas mixture was monitored by gas chromatography.

3. Results

The elemental analysis and textural properties of the samples prepared on the basis of the TUD-1 matrix, varying Ti-content, and either having ZnO nanoparticles or Cr^{6+} centers as additional ingredients, are listed in Table A1. The composition of the final catalysts reflects the synthesis gel compositions very well. The N_2 desorption/adsorption isotherms of the Ti-1, Ti1-Cr1 and Ti1-Zn10 samples (the numbers indicate the loading of the element in TUD-1) (Figure A1), are of type IV, representative for mesoporous materials according to IUPAC classification. The isotherm of the ZnO modified material (Zn-10) is slightly different as compared to the other composites, suggesting the formation of ZnO nanoparticles inside the pores. These ZnO nanoparticles are that small, that they are not visible in XRD patterns. The XRD patterns contain a broad diffraction line at around 23◦ -2 θ which is indicative of well-ordered amorphous silica [23, 24]. UV-Vis spectra of the prepared samples are plotted in Figure 1. All spectra were collected at ambient conditions. By comparison it is evident that the absorption band at 220 nm, assigned to isolated Ti sites in tetrahedral coordination [25], is somewhat reduced in intensity in the presence of the ZnO nanoparticles, but generally the absorption features appear a composite of the individual contributions of the ZnO nanoparticles and the Ti sites. ZnO nanoparticles supported on silica usually show a broad adsorption band around 240 - 400 nm [26, 27]. Relative intensities in the spectrum of CrO_x sites appear very different when in the presence Ti sites: the 480 nm absorption is reduced in intensity, whereas the relative intensity of the absorption at 375 nm increases. The 375 nm absorption and the shoulder at 480 nm are usually assigned to ligand to metal charge transfer (from O^{2-} to Cr^{6+}) of tetrahedrally coordinated Cr^{6+} [28, 29]. Additionally, the absence of a peak around 600 nm is an indication that $Cr^{3+}O_x$ is not present in the samples.

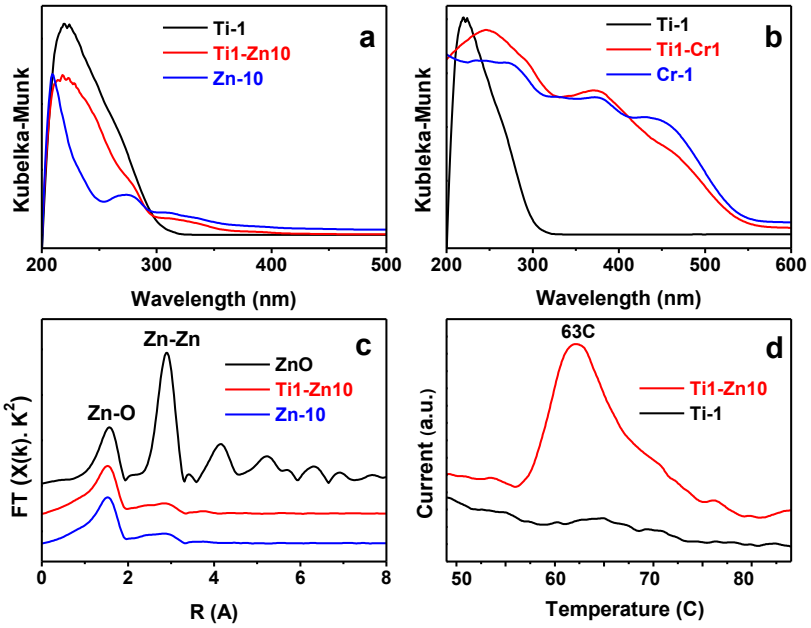

Figure 1. UV-Vis DRS spectra of the modified Ti-TUD-1 catalysts recorded in ambient conditions, **a:** the spectrum of the Ti-1-Zn-10 composite as compared to Zn-10 and Ti-1. **b:** the spectrum of the Ti1-Cr1 sample as compared to Cr-1 and Ti-1. **c:** ZnK EXAFS spectra of Zn-10 and Ti1-Zn10, compared to a reference ZnO sample. **d:** CO_2 TPD spectra of Ti-1 and Ti1-Zn10 samples.

In XANES spectra of the Ti1-Zn10 and Zn-10 samples (see Figure A2), the position of the ZnK X-Ray absorption edge remains unchanged when in the presence of titanium – at ca. 9662.5 eV, which is 1 eV higher as compared to ZnO measured in the same conditions (9661.5 eV). We therefore conclude that zinc is present as Zn^{2+} in all samples. The spectral shape of the XANES post-edge region of the two samples shows two relatively low maxima at 9664.6 and 9668.3 eV instead of one intense peak at 9668.7 eV typical for ZnO. This observation leads to the conclusion that a fraction of the Zn cations is located in the framework of TUD-1 as divalent cations and, more importantly, a considerable fraction of Zn is present in the form of ZnO nano-particles. This is in agreement with the work of Yoshida et al [30], who attributed the small band at 9668 eV measured for ZnO/SiO_2 catalysts to formation of clusters/oligomers of tetrahedral $[ZnO_4]^{6-}$ units.

The EXAFS spectrum (in the Fourier transformation) of Ti1-Zn10 is compared to those of Zn-10 and ZnO in Figure 1c. Two distinct peaks are observed in the spectrum of ZnO, the first around 1.5A is assigned to neighboring oxygen atoms in the first shell, while the second around 2.9A is assigned to Zn atoms in the second shell. The similarity in spectra suggests that the zinc oxide species in the Zn-10 and Ti1-Zn10 samples have the same Zn–O bond length and coordination number as those present in bulk ZnO (i.e. ZnO_4^{6-} tetrahedra). Furthermore, the spectra of Zn-10 and Ti1-Zn10 samples show a weak band around 2.5-3A which is corresponding to the second shell (i.e. Zn–Zn). The weak intensity of this absorption indicates that the coordination number of neighboring Zn atoms would be very low, which is in agreement with the formation of nanoparticles of ZnO [30]. The presence of these nanoparticles is further confirmed in a micrograph of the Ti1-Zn10 sample (Figure A4). The characteristic morphology of TUD-1 [31], and highly dispersed ZnO nanoparticles with a size of 5-7 nm can be observed, which is consistent with the pore diameter of this sample [19]. To study the ability of the ZnO containing samples to absorb CO_2, temperature programmed desorption (TPD) of CO_2 adsorbed at room temperature was carried out (Figure 1d). A desorption peak of CO_2 at 63^{o}C was observed in the desorption curve, which is absent in the curve of the Ti-1 sample. This confirms the ability of ZnO to bind CO_2 at room temperature and shows a relatively easy release of this CO_2.

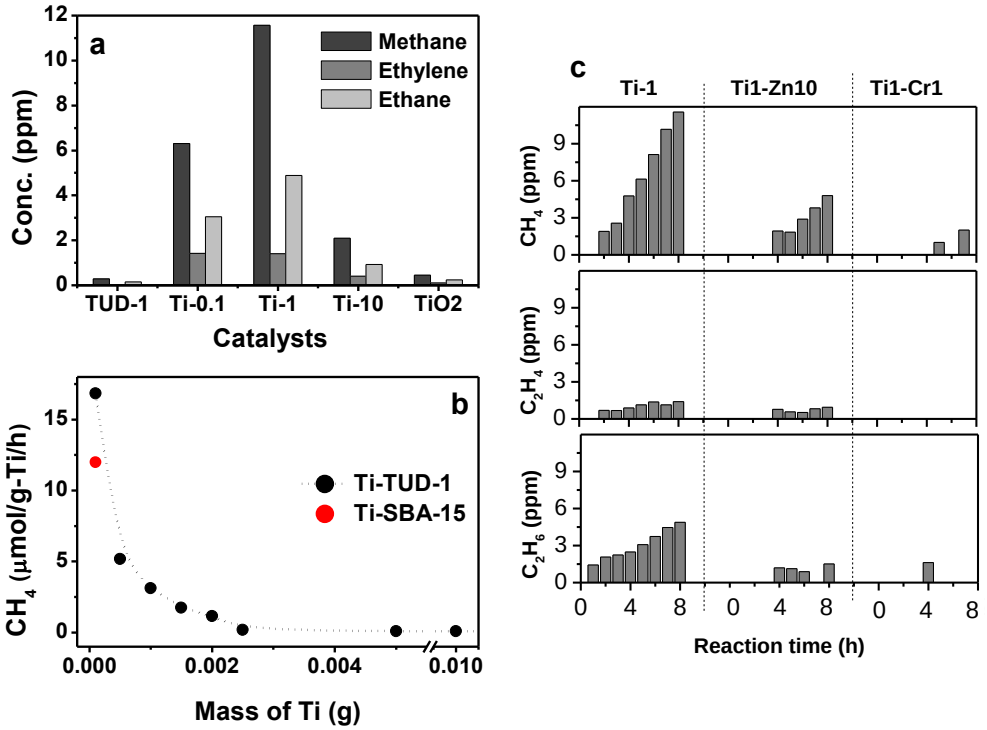

Figure 2. a: The concentration of the hydrocarbons (i.e. methane, ethylene and ethane) produced after 8h of illumination over the different Ti-TUD-1 samples. **b:** the concentration of methane per mass of titanium for the different Ti-TUD-1 samples and Ti-SBA-15. **c:** A comparison between the concentrations of produced hydrocarbons over Ti-1, Ti1-Zn10, and Ti1-Cr1.

Before discussion of the photocatalytic performance of the samples, it is important to note that removal of hydrocarbon residue, present in the samples as a consequence of the preparation procedure, is essential to confirm conversion of CO_2. Even after calcination at elevated temperature, small amounts of methane are typically observed upon illumination of the catalysts in the presence of water vapour [22]. UV treatment in humidified He was used to remove residual carbon, typically apparent by formation of at least 3 ppm of methane (8h of illumination in He/H_2O environment) for the Ti and Cr containing samples, to as high as 12 ppm for the Ti-1-Zn-10 and the Zn-10 samples. The cleaning of these ZnO containing samples was difficult and took 5 cycles to reach an acceptable level of CH_4 to evaluate CO_2 reduction.

First we will discuss the effect of the Ti loading on the hydrocarbon formation efficacy, presented in Figure 2a. After 8h of illumination, two reference samples, siliceous TUD-1 and TiO_2 Hombikat (the latter consisting of a high surface area anatase phase) show minor quantities of products. Of the Ti-TUD-1 samples, Ti-1 is the most active, showing methane, ethylene and ethane as products. The amount of produced hydrocarbons is higher than obtained using Ti-0.1 or Ti-10. This can be explained by the amount of isolated tetrahedrally coordinated Ti^{4+} species available for the reaction. This increases comparing Ti-0.1 and Ti-1, and decreases comparing Ti-1 and Ti-10. Ti-10 contains nanoparticles of TiO_2 (octahedrally coordinated Ti-sites) inside the pores of TUD-1 [19], which are less effective in apparent hydrocarbon formation [9].

Figure 2b shows the decreasing trend in methane production rate as a function of increasing Ti-mass, confirming isolated Ti^{4+} centres provide the optimal catalytic environment for hydrocarbon production. A comparison between the photocatalytic rates of Ti-TUD-1 and Ti-SBA-15 showed a 30% increase in the total hydrocarbons produced for TUD-1. The advantage of using TUD-1 as a support lies in the relatively high Ti loading that can be applied, before loss of dispersion of isolated tetrahedrally coordinated sites is apparent. Related to this aspect, comparison of TUD-1 with other mesoporous materials has been reported few times such as in [32-35]. The Ti-1 sample is catalytically stable: Fig A5 shows reproducibility in the amount of products formed, when using the Ti-1 sample in 6 consecutive runs.

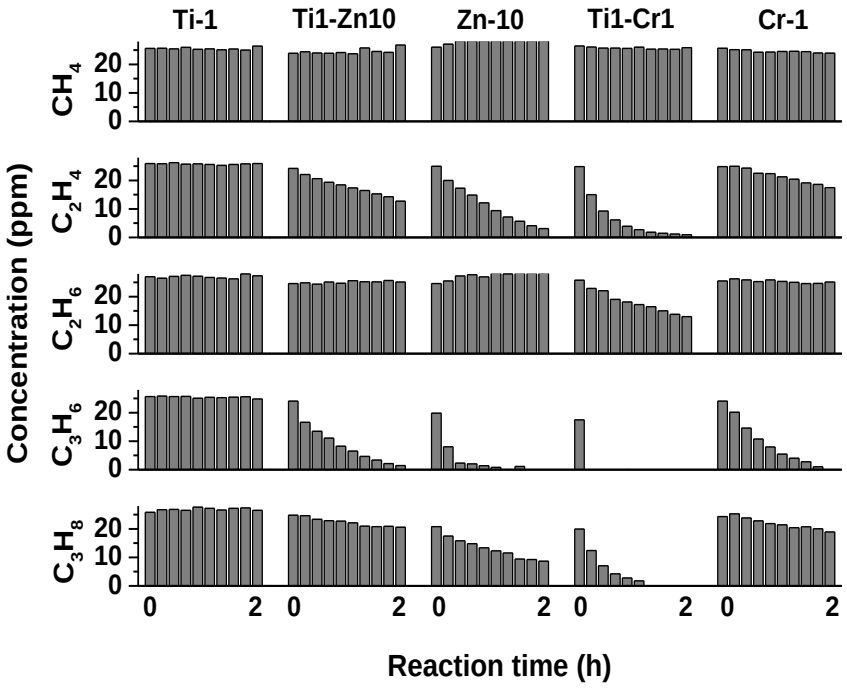

Figure 3. The degradation profiles of the standard hydrocarbons over the prepared samples. The concentrations were recorded every 15 min. for the duration of 2 hours.

The photocatalytic performance of the Ti-1 sample is compared to the performance of Ti1-Zn10 and Ti1-Cr1 in Figure 2c. Surprisingly, the performance of Ti-1 is significantly better than of the modified samples. Ti-TUD-1 showed less than half in productivity after incorporation of the ZnO nanoparticles. The detrimental effect of adding Cr is even worse: Ti-TUD-1 almost completely lost its efficacy.

An explanation for the adverse effect of the modifications of the catalyst can be found in the following experiments. A mixture of five different hydrocarbons CH_4, C_2H_4, C_2H_6, C_3H_6, and C_3H_8 was exposed to the catalyst formulations in the presence of light and water vapour, and the result shown in Figure 3. Not surprisingly, methane only slowly degrades over the catalytic systems in a period of 135 minutes of illumination. The saturated hydrocarbons (i.e. ethane and propane) are less stable than methane, and significant conversion can be observed, in particular over the Ti-1-Cr-1 sample. Depending on catalyst composition, unsaturated hydrocarbons (i.e. ethylene and propylene) were degraded very efficiently. An order in

photocatalytic performance of Ti1-Cr1 > Zn-10 > Cr-1 > Ti1-Zn10 > Ti-1 has been identified. This experiment shows how important evaluation of the back-reaction of hydrocarbons is in explaining performance of catalysts in CO_2 reduction, in particular if batch reactors are used. This is often necessary to reach concentrations of products detectable by flame ionisation detectors of GC equipment. It should also be noted that the activity of Ti-10 and in particular Hombikat TiO_2 is significantly higher in hydrocarbon oxidation, as compared to Ti-1 (Figure A6), which might explain the usually observed poor performance of e.g. modified crystalline TiO_2 in CO_2 reduction.

To the best of our knowledge, the absence of photocatalytic oxidation activity of methane and ethane over purely tetrahedrally coordinated Ti supported on silica has not been reported previously. However, the extent of activity of the catalysts active in hydrocarbon oxidation is generally in agreement with literature observations. Yamashita et al [36] showed that whereas ethylene was hardly activated by Ti-MCM-41, propylene [37, 38] and propane [19, 39] are significantly converted. It has also been reported that methane, ethane and propane can be oxidized over ZnO containing catalysts at slightly elevated temperatures (T = 493K (Wada et al) [40] and 500-550 K (Watanabe et al) [41]). We show photocatalytic conversion of propane is also feasible over silica supported nanoparticles of ZnO at room temperature. $Cr^{6+}O_x$ supported on silica was found to activate propane [21], and propylene [42]. Moreover, the synergy between Ti^{4+} and Cr^{6+} for hydrocarbon degradation observed in Figure 3 is in agreement with the pioneering work of Yamashita et al, who observed activation of propane using Cr-Ti-MCM-41 [36], Cr-Ti-HMS, and Cr-Ti-zeolites [43, 44], respectively.

The small conversion rate of methane shown in Figure 3, does not come in complete agreement with the significant reduction in formation of this product in the CO_2 reduction experiments shown in Figure 2c, in particular for the ZnO containing catalysts. We believe this might be due to reverse, rather than forward reactions of intermediates. We have previously proposed formaldehyde being a key intermediate in the formation of methane, for which hypothesis Strunk et al [45] recently provided additional evidence. It has further been reported that ZnO can photo-degrade formaldehyde to carbon dioxide and water [46, 47], thus effectively reducing the apparent rate of formation of methane in photocatalytic reduction of CO_2. A secondary detrimental effect of ZnO might be ineffective light absorption by ZnO nanoparticles (shielding Ti-centers, in particular of the low wavelength UV radiation (Figure 1a)), leading to a lower steady state concentration of photoexcited isolated

Ti-centers. This presumably also contributes to the lower apparent rate in CO_2 reduction of the ZnO containing composite. The degradation of formaldehyde to CO_2 likely also contributes to the negative effect of Cr^{6+} ions on performance of Ti-TUD-1 in production of methane. Cr^{6+} was reported to significantly enhance the performance of TiO_2 in the degradation of formaldehyde [48, 49]. To demonstrate the conversion of formaldehyde, the supplementary information contains *in situ* Diffuse Reflectance Infrared spectra of light induced conversion of formaldehyde in the presence of water vapour (Figure A7). Comparing the spectra of Ti-1 to that of Ti1-Cr1 after illumination for an hour, the Cr-containing sample displays the signature of vibrational modes of formates, which are completely absent in the spectrum of the Ti-1 catalyst. When formate is coordinating to metal ions in zeolitic environment, bands at 1580 cm^{-1}, ~1370 cm^{-1} and 1350 cm^{-1} can be assigned to the ν_{as} OCO, δ C-H, and ν_s OCO modes, respectively [50]. One last observation from the data of Figure 3 needs explanation: the Ti1-Zn10 sample exhibits an apparent photocatalytic degradation activity towards ethylene, propylene and propane which is significantly smaller than of the Zn-10 catalyst. Presumably, CO_2 produced by conversion of hydrocarbons over the ZnO nanoparticles, is converted reversibly to hydrocarbons over the Ti-centers, in agreement with the data of Figure 2c.

4. Conclusion

In summary, of the three modifications of silica supported Ti catalysts, alteration of the silica support has led to improvement in catalytic performance, explained by the relatively high loadings that can be achieved without losing dispersion of isolated Ti centers. Addition of ZnO nanoparticles leads to a smaller apparent rate in hydrocarbon production, despite the achieved storage capacity for CO_2. Adding visible light absorption functionality by CrO_x, is even more detrimental to the observed production of hydrocarbons. Both ZnO and CrO_x addition to Ti-TUD-1 lead to significantly enhanced rates in the backward reactions of intermediates, such as formaldehyde, as well as of the produced hydrocarbons (in particular ethylene).

This study clearly demonstrates the importance of evaluating (backward) hydrocarbon conversion, when attempting to produce these by photocatalytic CO_2 reduction in the presence of water vapour. Photocatalyst and process development should attempt to minimize hydrocarbon conversion in process conditions needed for CO_2 reduction. This is not easy to achieve, since hydrocarbon oxidation is not only caused by the presence of oxygen, the co-product of CO_2 reduction, but also by water vapour, which is at the same time essential for the first step in activating CO_2.

References

[1] T. Inoue, A. Fujishima, S. Konishi, K. Honda, Photoelectrocatalytic reduction of carbon dioxide in aqueous suspensions of semiconductor powers, Nature, 277 (1979) 637-638.

[2] T. Mizuno, K. Adachi, K. Ohta, A. Saji, Effect of CO_2 pressure on photocatalytic reduction of CO_2 using TiO_2 in aqueous solutions, Journal of Photochemistry and Photobiology A: Chemistry, 98 (1996) 87-90.

[3] S. Kaneco, Y. Shimizu, K. Ohta, T. Mizuno, Photocatalytic reduction of high pressure carbon dioxide using TiO_2 powders with a positive hole scavenger, Journal of Photochemistry and Photobiology A: Chemistry, 115 (1998) 223-226.

[4] I.H. Tseng, W.C. Chang, J.C.S. Wu, Photoreduction of CO_2 using sol-gel derived titania and titania-supported copper catalysts, Applied Catalysis B: Environmental, 37 (2002) 37-48.

[5] S.S. Tan, L. Zou, E. Hu, Photocatalytic reduction of carbon dioxide into gaseous hydrocarbon using TiO_2 pellets, Catalysis Today, 115 (2006) 269-273.

[6] J. Pan, X. Wu, L. Wang, G. Liu, G.Q. Lu, H.M. Cheng, Synthesis of anatase TiO2 rods with dominant reactive {010} facets for the photoreduction of CO_2 to CH4 and use in dye-sensitized solar cells, Chemical Communications, 47 (2011) 8361-8363.

[7] T. Yui, A. Kan, C. Saitoh, K. Koike, T. Ibusuki, O. Ishitani, Photochemical reduction of CO_2 using TiO_2: Effects of organic adsorbates on TiO_2 and deposition of Pd onto TiO_2, ACS Applied Materials and Interfaces, 3 (2011) 2594-2600.

[8] S. Krejcikova, L. Matejova, K. Koci, L. Obalova, Z. Matej, L. Capek, O. Solcova, Appl. Catal., B, 111 (2012).

[9] M. Anpo, K. Chiba, Photocatalytic reduction of CO_2 on anchored titanium oxide catalysts, Journal of Molecular Catalysis, 74 (1992) 207-212.

[10] H. Yamashita, Y. Fujii, Y. Ichihashi, S.G. Zhang, K. Ikeue, D.R. Park, K. Koyano, T. Tatsumi, M. Anpo, Selective formation of CH3OH in the photocatalytic reduction of CO_2 with H_2O on titanium oxides highly dispersed within zeolites and mesoporous molecular sieves, Catalysis Today, 45 (1998) 221-227.

[11] K. Ikeue, H. Yamashita, M. Anpo, T. Takewaki, Photocatalytic reduction of CO_2 with H_2O on Ti-β zeolite photocatalysts: Effect of the hydrophobic and hydrophilic properties, Journal of Physical Chemistry B, 105 (2001) 8350-8355.

[12] H.C. Yang, H.Y. Lin, Y.S. Chien, J.C.S. Wu, H.H. Wu, Mesoporous TiO2/SBA-15, and Cu/TiO_2/SBA-15 composite photocatalysts for photoreduction of CO_2 to methanol, Catalysis Letters, 131 (2009) 381-387.

[13] C.C. Yang, J. Vernimmen, V. Meynen, P. Cool, G. Mul, Mechanistic study of hydrocarbon formation in photocatalytic CO_2 reduction over Ti-SBA-15, Journal of Catalysis, 284 (2011) 1-8.
[14] A. Dhakshinamoorthy, S. Navalon, A. Corma, H. Garcia, Photocatalytic CO_2 reduction by TiO_2 and related titanium containing solids, Energy and Environmental Science, 5 (2012) 9217-9233.
[15] K. Mori, H. Yamashita, M. Anpo, Photocatalytic reduction of CO_2 with H_2O on various titanium oxide photocatalysts, RSC Advances, 2 (2012) 3165-3172.
[16] B. Mei, A. Becerikli, A. Pougin, D. Heeskens, I. Sinev, W. Grünert, M. Muhler, J. Strunk, Tuning the acid/base and structural properties of titanate-loaded mesoporous silica by grafting of zinc oxide, Journal of Physical Chemistry C, 116 (2012) 14318-14327.
[17] L. Davydov, E.P. Reddy, P. France, P.G. Smirniotis, Transition-metal-substituted titania-loaded MCM-41 as photocatalysts for the degradation of aqueous organics in visible light, Journal of Catalysis, 203 (2001) 157-167.
[18] S. Shen, L. Guo, Hydrothermal synthesis, characterization, and photocatalytic performances of Cr incorporated, and Cr and Ti co-incorporated MCM-41 as visible light photocatalysts for water splitting, Catalysis Today, 129 (2007) 414-420.
[19] M.S. Hamdy, O. Berg, J.C. Jansen, T. Maschmeyer, J.A. Moulijn, G. Mul, TiO_2 nanoparticles in mesoporous tud-1: synthesis, characterization and photocatalytic performance in propane oxidation, Chem. Eur. J., 12 (2006) 620-628.
[20] M. Ramakrishna Prasad, M.S. Hamdy, G. Mul, E. Bouwman, E. Drent, Efficient catalytic epoxidation of olefins with silylated Ti-TUD-1 catalysts, Journal of Catalysis, 260 (2008) 288-294.
[21] M.S. Hamdy, O. Berg, J.C. Jansen, T. Maschmeyer, A. Arafat, J.A. Moulijn, G. Mul, Chromium-incorporated TUD-1 as a new visible light-sensitive photo-catalyst for selective oxidation of propane, Catalysis Today, 117 (2006) 337-342.
[22] C.C. Yang, Y.H. Yu, B. Van Der Linden, J.C.S. Wu, G. Mul, Artificial photosynthesis over crystalline TiO_2-based catalysts: Fact or fiction?, Journal of the American Chemical Society, 132 (2010) 8398-8406.
[23] W. Chen, W. Cai, L. Zhang, G. Wang, L. Zhang, Sonochemical processes and formation of gold nanoparticles within pores of mesoporous silica, Journal of Colloid and Interface Science, 238 (2001) 291-295.
[24] F. Adam, T.S. Chew, J. Andas, A simple template-free sol-gel synthesis of spherical nanosilica from agricultural biomass, Journal of Sol-Gel Science and Technology, 59 (2011) 580-583.

[25] S. Klein, B.M. Weckhuysen, J.A. Martens, W.F. Maier, P.A. Jacobs, Homogeneity of titania-Silica mixed oxides: On UV-DRS studies as a function of titania content, Journal of Catalysis, 163 (1996) 489-491.
[26] O.P. Tkachenko, K.V. Klementiev, E. Löffler, I. Ritzkopf, F. Schüth, M. Bandyopadhyay, S. Grabowski, H. Gies, V. Hagen, M. Muhler, L. Lu, R.A. Fischer, W. Grünert, The structure of zinc and copper oxide species hosted in porous siliceous matrices, Physical Chemistry Chemical Physics, 5 (2003) 4325-4334.
[27] D.W. Bahnemann, C. Kormann, M.R. Hoffmann, Preparation and characterization of quantum size zinc oxide: A detailed spectroscopic study, Journal of Physical Chemistry, 91 (1987) 3789-3798.
[28] J.J. Zou, Y. Liu, L. Pan, L. Wang, X. Zhang, Photocatalytic isomerization of norbornadiene to quadricyclane over metal (V, Fe and Cr)-incorporated Ti-MCM-41, Applied Catalysis B: Environmental, 95 (2010) 439-445.
[29] L. Zhang, Y. Zhao, H. Dai, H. He, C.T. Au, A comparative investigation on the properties of Cr-SBA-15 and CrO_x/SBA-15, Catalysis Today, 131 (2008) 42-54.
[30] H. Yoshida, T. Shimizu, C. Murata, T. Hattori, Highly dispersed zinc oxide species on silica as active sites for photoepoxidation of propene by molecular oxygen, Journal of Catalysis, 220 (2003) 226-232.
[31] J.C. Jansen, Z. Shan, L. Marchese, W. Zhou, N.V.D. Puil, T. Maschmeyer, A new templating method for three-dimensional mesopore networks, Chemical Communications, (2001) 713-714.
[32] C.X.S. Wang, A. Gaffney, R. Song, Proceedings of 245th ACS Meeting, (2013).
[33] G. Imran, M.P. Pachamuthu, R. Maheswari, A. Ramanathan, S.J. Sardhar Basha, Catalytic activity of MnTUD-1 for liquid phase oxidation of ethylbenzene with tert-butyl hydroperoxide, Journal of Porous Materials, 19 (2012) 677-682.
[34] T. Heikkilä, J. Salonen, J. Tuura, N. Kumar, T. Salmi, D.Y. Murzin, M.S. Hamdy, G. Mul, L. Laitinen, A.M. Kaukonen, J. Hirvonen, V.P. Lehto, Evaluation of mesoporous TCPSi, MCM-41, SBA-15, and TUD-1 materials as API carriers for oral drug delivery, Drug Delivery, 14 (2007) 337-347.
[35] Z. Guo, C. Zhou, S. Hu, Y. Chen, X. Jia, R. Lau, Y. Yang, Epoxidation of trans-stilbene and cis-cyclooctene over mesoporous vanadium catalysts: Support composition and pore structure effect, Applied Catalysis A: General, 419-420 (2012) 194-202.
[36] T. Kamegawa, T. Shudo, H. Yamashita, Preparation of Cr-Ti binary oxide anchored mesoporous silica by CVD method and their photocatalytic activities, Topics in Catalysis, 53 (2010) 555-559.

[37] H. Yoshida, C. Murata, T. Hattori, Screening study of silica-supported catalysts for photoepoxidation of propene by molecular oxygen, Journal of Catalysis, 194 (2000) 364-372.
[38] H. Yamashita, S. Nishio, I. Katayama, N. Nishiyama, H. Fujii, Photo-induced super-hydrophilic property and photocatalysis on transparent Ti-containing mesoporous silica thin films, Catalysis Today, 111 (2006) 254-258.
[39] Y. Hu, N. Wada, K. Tsujimaru, M. Anpo, Photo-assisted synthesis of V and Ti-containing MCM-41 under UV light irradiation and their reactivity for the photooxidation of propane, Catalysis Today, 120 (2007) 139-144.
[40] K. Wada, K. Yoshida, T. Takatani, Y. Watanabe, Selective photo-oxidation of light alkanes using solid metal oxide semiconductors, Applied Catalysis A, General, 99 (1993) 21-36.
[41] K. Wada, K. Yoshida, Y. Watanabe, T. Suzuki, Chem. Commun., (1991) 726.
[42] X. Shi, S. Ji, K. Wang, Oxidative dehydrogenation of ethane to ethylene with carbon dioxide over Cr-Ce/SBA-15 catalysts, Catalysis Letters, 125 (2008) 331-339.
[43] S. Ohshiro, O. Chiyoda, K. Maekawa, Y. Masui, M. Anpo, H. Yamashita, Design of Cr-oxide photocatalyst loaded on zeolites and mesoporous silica as a visible-light-sensitive photocatalyst, Comptes Rendus Chimie, 9 (2006) 846-850.
[44] Y. Masui, S. Ohshiro, M. Anpo, T. Ohmichi, I. Katayama, H. Yamashita, Preparation of (Cr,Ti)-containing mesoporous silica photocatalyst using a photo-assisted deposition method: Selective oxidation of propene with oxygen under visible light irradiation, e-Journal of Surface Science and Nanotechnology, 3 (2005) 448-452.
[45] B. Mei, A. Pougin, J. Strunk, Influence of photodeposited gold nanoparticles on the photocatalytic activity of titanate species in the reduction of CO_2 to hydrocarbons, Journal of Catalysis, 306 (2013) 184-189.
[46] Y. Liao, C. Xie, Y. Liu, Q. Huang, Enhancement of photocatalytic property of ZnO for gaseous formaldehyde degradation by modifying morphology and crystal defect, Journal of Alloys and Compounds, 550 (2013) 190-197.
[47] Z. Ai, S. Lee, Y. Huang, W. Ho, L. Zhang, Photocatalytic removal of NO and HCHO over nanocrystalline Zn_2SnO_4 microcubes for indoor air purification, Journal of Hazardous Materials, 179 (2010) 141-150.
[48] K.A. Michalow, E.H. Otal, D. Burnat, G. Fortunato, H. Emerich, D. Ferri, A. Heel, T. Graule, Flame-made visible light active TiO_2:Cr photocatalysts: Correlation between structural, optical and photocatalytic properties, Catalysis Today, 209 (2013) 47-53.
[49] R.C.W. Lam, M.K.H. Leung, D.Y.C. Leung, L.L.P. Vrijmoed, W.C. Yam, S.P. Ng, Visible-light-assisted photocatalytic degradation of gaseous formaldehyde by

parallel-plate reactor coated with Cr ion-implanted TiO_2 thin film, Solar Energy Materials and Solar Cells, 91 (2007) 54-61.
[50] M.C. Kung, S.S.Y. Lin, H.H. Kung, In situ infrared spectroscopic study of CH_4 oxidation over Co-ZSM-5, Topics in Catalysis, 55 (2012) 108-115.

Appendix

Table A1. The elemental analysis, textural properties and the colors of the prepared samples.

Sample	Code	Elemental analysis		Texture properties			Color
		Si/Ti	Si/M[a]	S[b] (m^2/g)	V[c] (cm^3/g)	D[d] (nm)	
Ti-TUD-1	Ti-1	112	0	628	1.07	9.1	White
ZnO-Ti-TUD-1	Ti1-Zn10	109	9.8	735	0.82	5.1	White
Zn-TUD-1	Zn-10	0	9.98	680	0.91	6.3	White
Cr-Ti-TUD-1	Ti1-Cr1	108	111	625	1.28	10.2	Yellow
Cr-TUD-1	Cr-1	0	118	590	1.43	8.8	Yellow

[a] M = Zn or Cr

[b] BET Specific surface area

[c] Mesoporous volume

[d] Mesoporous diameter

Figure A1

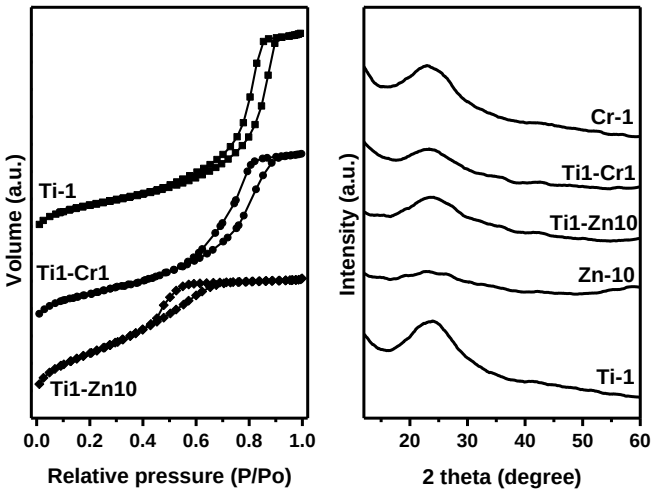

Figure A1. Left panel: The N_2 isotherms of the Ti-1 sample compared to the modified samples, Ti1-Cr1 and Ti1-Zn10. Left panel: Wide angle XRD patterns of the prepared samples.

Figure A2

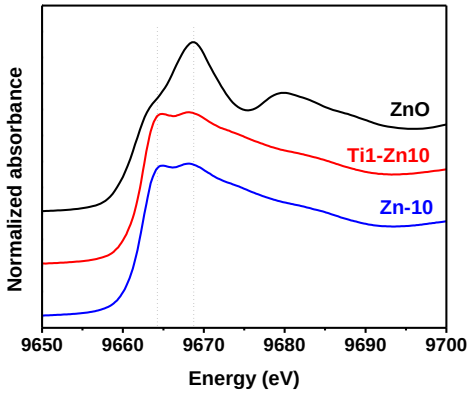

Figure A2. ZnK XANES spectra of Zn-10 and Ti1-Zn10, as compared to reference ZnO.

Figure A3

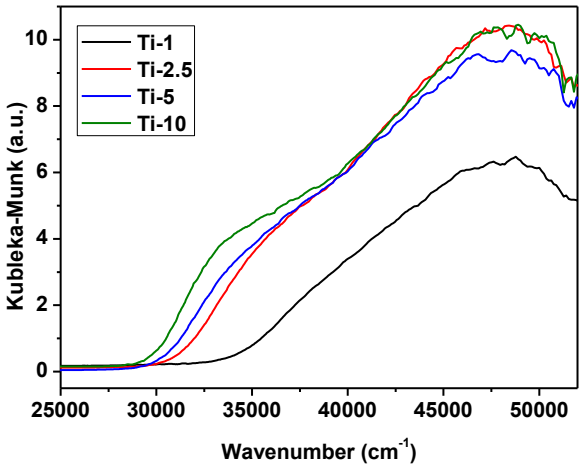

Figure A3 UV-DRS spectra of Ti-TUD-1 samples. Spectra were measured under dried conditions where samples were heated over-night at 180°C.

Table A2. The % of tetrahedral Ti^{4+} in Ti-TUD-1 samples.

Sample	Ti^{4+} tetrahedral*
Ti-1	99.9%
Ti-2.5	68%
Ti-5	65%
Ti-10	58%

* The tetrahedral Ti^{4+} % was calculated by dividing the area of the 48000 cm^{-1} peak by the summation of the areas of the 48000 cm^{-1} peak and the 35000 cm^{-1} peak.

Figure A4

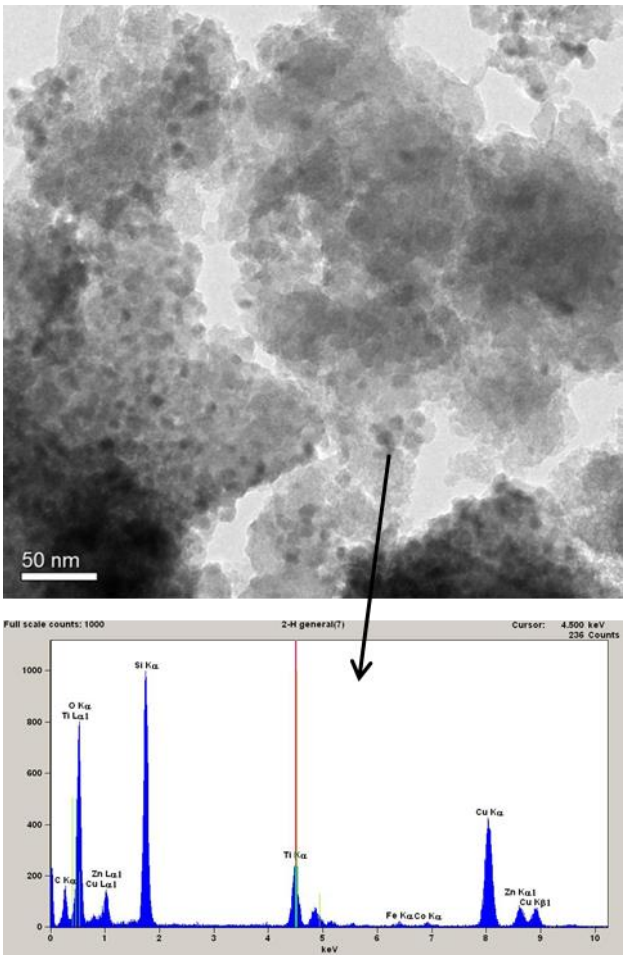

Figure A4. Top panel: HR-TEM micrograph of the Ti1-Zn10 sample. Bottom panel: A print-screen image of the EDX analysis of the sample. The arrow signals the area focused on for the analysis.

Figure A5

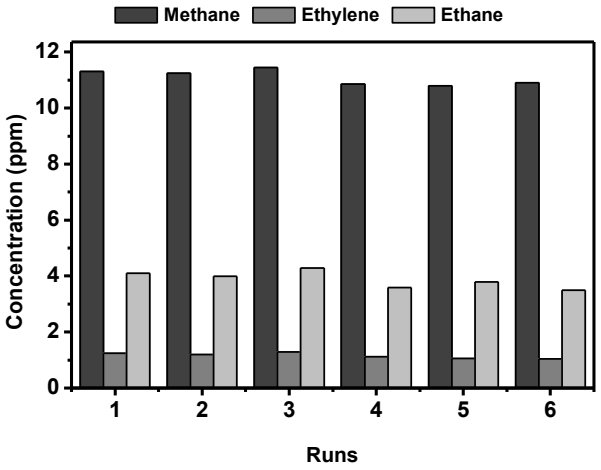

Figure A5. The concentration of the different hydrocarbons produced after 8 hours of illumination, for a repetition of 6 runs over the same Ti-1 sample, without any further treatment between runs.

Figure A6

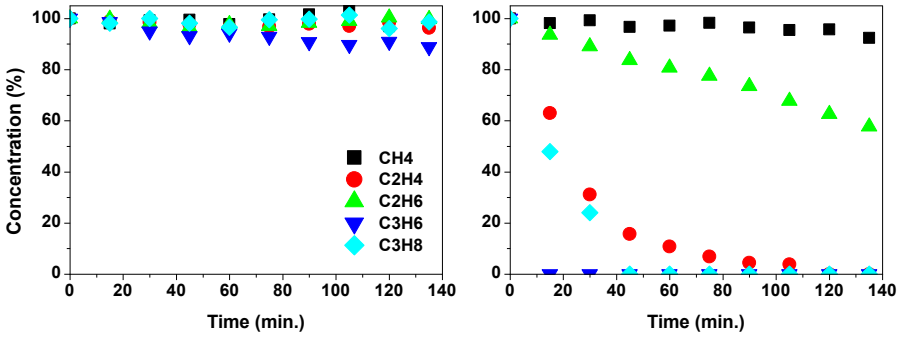

Figure A6. The degradation profiles of the different hydrocarbons over Ti-10 (Left panel) and Hombikat TiO_2 (Right panel).

Figure A7

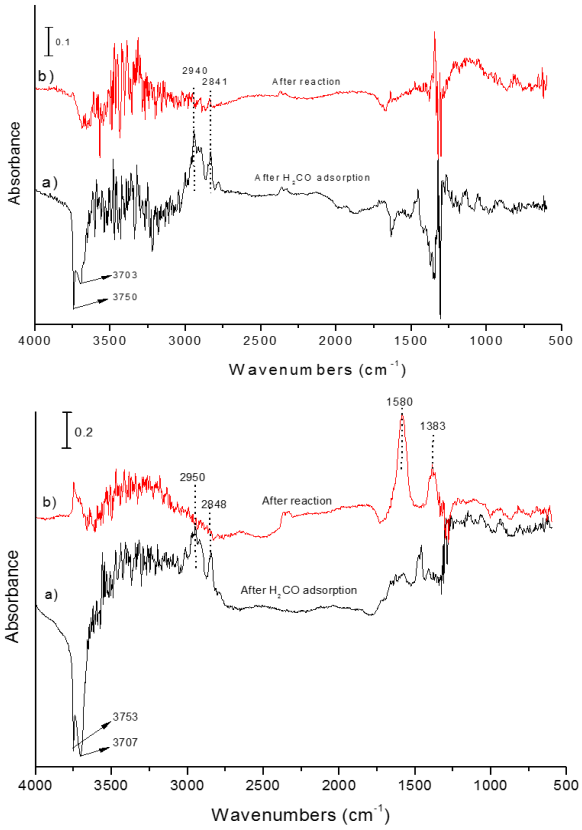

Figure A7. DRIFT spectra recorded after adsorption of formaldehyde/water (spectrum a), recorded against a background of the catalyst dried at 393 K, followed by illumination (spectrum b), recorded after 1 hour, against spectrum a) as background. The upper panel contains the spectra of Ti-1, and the bottom panel of Ti1-Cr1. Comparing the two catalytically active materials, it is evident that formaldehyde is effectively oxidized to formate (1580 and 1383 cm^{-1}) over the Cr containing catalytic formulation, whereas formate formation is not observed for the catalyst without Cr. This supports the hypothesis that besides a high activity for oxidation of hydrocarbon products, intermediates (formaldehyde) are likely to show very different chemistry over supported Cr-containing catalysts as compared to Ti-only.

Table A3. The first order rate constant of the hydrocarbons degraded over the different Ti-TUD-1 samples. The obtained negative values are due to slight production of methane and/or ethane due conversion of carbon contamination in the ZnO containing samples.

	The first order rate constant *k x 10^{-3} (min^{-1})*				
Hydrocarbon	**Ti-1**	**Ti1-Zn10**	**Zn-10**	**Ti1-Cr1**	**Cr-1**
Methane	0.08	0.02	-2.49	1.02	0.97
Ethylene	0.10	4.5	11.6	80.3	2.06
Ethane	-0.33	-0.13	-1.76	5.9	0.05
Propylene	0.35	17.0	44.7	640.0	18.9
Propane	0.85	1.66	7.01	125.8	2.13

Chapter 8

Outlook

Recommendations for future work

1. Selective photocatalytic oxidation

In this thesis, liquid phase selective methylcyclohexane oxidation has been studied to determine the performance of various photocatalysts, including reduced 'blue' TiO_2, Au promoted TiO_2, and TiO_2 modified by 'dopants' and Pt metallic nanoparticles. Photocatalytic selective oxidation is still a developing field and the mechanism behind the formation of intermediates and products is typically not understood. It would be very illustrative to study the effects of oxygen partial pressure and water concentration on selectivity, to obtain more in depth understanding of the origin of the oxygen involved in production of (partially) oxidized MCH. Either direct activation of oxygen dissolved in the liquid medium, or oxygen associated with the oxides used for photocatalysis (Mars and van Krevelen mechanism) could be feasible. For oxidation of cyclohexane, evidence for a Mars and van Krevelen mechanism has been found by using $^{18}O_2$ in the oxidation process [1]. At the same time, the results presented in chapter 3 indicate that oxygen vacancies increase the photocatalytic performance of TiO_2 in the conversion of MCH to ketones, even though these were found not to be stable. The use of $^{18}O_2$ in the oxidation process catalyzed by photo-excited 'blue' TiO_2 could reveal more mechanistic detail on the role of these surface vacancies in photocatalytic oxidation of organic molecules (in the liquid phase). Additionally, connecting the in situ ATR spectroscopic cell to Mass Spectrometry (ATR-MS) would be useful, to be able to also quantitatively determine the amount, and if $^{18}O_2$ is used, the origin of gas phase products (CO, CO_2) formed in the process.

Research aimed at obtaining more in depth knowledge of structure activity correlations for TiO_2 containing other elements (e.g. Cr, V) as dopant is also suggested. E.g. these elements could be beneficial for stabilizing oxygen vacancies. In this case maybe the overall activity compared to pure blue Ti^{3+} containing TiO_2 is also improved. Another option to increase activity could be to combine semiconductors with suitable band level positions to create heterojunctions, as has been proposed by Kudo and coworkers to enhance performance in the overall water splitting reaction [2]. Little is known about the efficiency of creating these junctions in stimulating selective oxidation processes, whereas again studies using labeled oxygen could be illustrative in the elucidation of the mechanism relevant for these materials.

It is well-known that Pt deposition on the surface of photocatalysts can help to improve electron- hole pair separation and decrease recombination. In many cases, adding Pt nanoparticles improved photocatalytic activity. We also showed this effect is applicable in chapters 5 and 6 in case of $Pt/Cr/TiO_2$ and Pt/WO_3. But unexpectedly, during our research, deposition of Pt on Blue Ti^{3+} (not shown in this thesis) decreased the activity and selectivity of MCH oxidation. The negative effect of Pt in this case is recommended to be further studied in detail.

Au/P25 also needs some further characterization in order to understand the chemical nature of Au and its role in generating the plasmon resonance energy effect. Additional measurements (such as XPS) are necessary to understand the structure-activity correlation of Au in photocatalytic selective oxidation.

2. Gas sensing

Pt/WO_3 is used in gas sensing applications, for example for sensing of ethanol. In chapter 6, performance of Pt/WO_3 in selective oxidation has been evaluated by use of a batch reactor. Additionally, connecting the In situ Diffuse Reflectance Infrared Fourier Transformed spectroscopy to Mass Spectrometry (DRIFT-MS) is useful, to obtain further detail in the mechanism of the oxidation reaction.

Further analysis of the specific material in sensing ethanol is interesting. The development of a lab reactor which could be used to simultaneously mimic commercial sensors and allow analysis of molecular surface transformations would be quite valuable. Also reactor design optimizing sensing capability would be interesting. Using light, rather than temperature to enhance sensing sensitivity might be more energetically favorable. Then an irradiation source (e.g. LED) and exact control of pressure, should be considered. In summary, a lot of research could be done in the gas sensing field. In case of gas sensing, also Pt/WO_3-TiO_2 is proposed as a promising gas sensor. In our case, maybe it has benefit to combine WO_3 and TiO_2 functionalized by photo-deposited Pt.

Research at the interface between materials for (photo) catalysis and gas sensing might provide synergy and induce improvements for both.

References

[1] A.R. Almeida, J.A. Moulijn, G. Mul, Photocatalytic oxidation of cyclohexane over TiO2: Evidence for a Mars-van krevelen mechanism, Journal of Physical Chemistry C, 115 (2011) 1330-1338.
[2] A. Iwase, Y.H. Ng, Y. Ishiguro, A. Kudo, R. Amal, Reduced graphene oxide as a solid-state electron mediator in Z-scheme photocatalytic water splitting under visible light, Journal of the American Chemical Society, 133 (2011) 11054-11057.

Summary

The focus of the research described in this thesis was on the engineering and design of effective photocatalysts able to catalyze the oxidative conversion of hydrocarbons. The prepared catalysts were synthesized by using different procedures involving sol-gel precursors, and impregnation or photo-deposition of metallic nanoparticles. The prepared materials were characterized by several techniques in order to identify the obtained composition and morphology. The photocatalytic performance of the prepared materials was investigated in different oxidative photocatalytic conversions such as methylcyclohexane (MCH) oxidation, ethanol oxidation, or simultaneous oxidation of mixtures of hydrocarbons. To evaluate performance of the synthesized materials, several techniques have been used such as ATR-FTIR, DRIFT, a multi-reactor set-up, and a top illuminated batch reactor setup.

In **chapter 1**, an introduction is given to the basic principles of photocatalysis. Furthermore, an introduction to the photocatalysts and the applied SiO_2 based support (TUD-1) is given, as well as background on some general aspects of the mechanism of plasmonic enhancement of photocatalytic activity.

In **chapter 2**, an overview of the experimental procedures is presented. An introduction is given to IR spectroscopy applying two different reaction cells, one for liquid (ATR), and another for gas phase analysis (DRIFT). Also a photocatalytic reactor system equipped with a GC (gas chromatograph) is described, as well as the use of a setup containing multiple reactors for evaluation of gas phase photocatalysis.

In **chapter 3**, blue titania is shown to be a more active photocatalyst than either P25 or commercial rutile titania in the photocatalytic oxidation of MCH, in particular at 425 nm. Blue titania also showed higher selectivity towards production of ketones. The catalyst unfortunately showed deactivation as a result of photo-induced oxidation of Ti^{3+} to Ti^{4+} by molecular oxygen. A schematic diagram of the MCH oxidation process over different photocatalysts (i.e. blue titania, P25 and rutile) is shown in Figure 1.

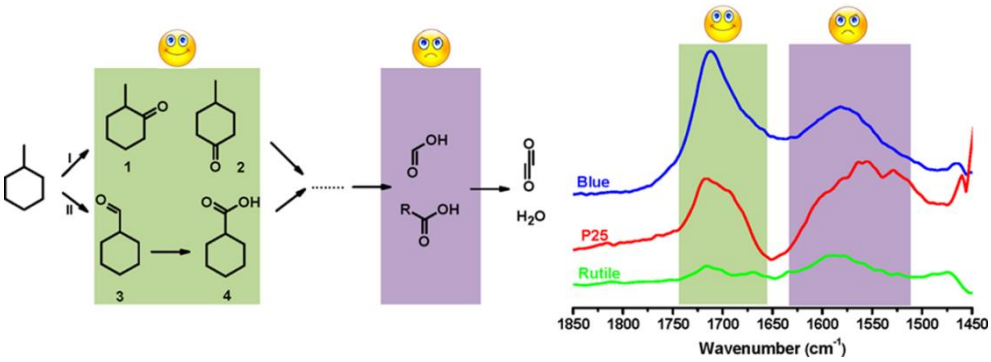

Figure 1: Schematic overview of the MCH oxidation processes and spectra observed for blue titania, P25 and rutile

The influence of Au nanoparticles prepared by deposition–precipitation was evaluated for promoting photocatalytic activity of P25 in the oxidation of methylcyclohexane. The results are described in **chapter 4.** In situ ATR-FTIR spectroscopy was used to compare the rates of reaction. Illumination was manipulated by using arrays of LEDs with alternating wavelengths of 375 and 525 nm, or 425 and 525 nm. At 375 and in particular at 425 nm, Au was found to significantly enhance the rate induced by P25 in methylcyclohexane oxidation. Illumination of Au-promoted P25 at 525 nm did not result in any measureable activity, nor was the addition of 525 nm light effective in further enhancement of activity at 375 or 425 nm. This excludes heating of Au particles to be of influence in promoting the rates at 375 and 425 nm. To validate whether the enhancement at 425 nm was purely catalytic, or if plasmonic effects were relevant, the rates of Au/TiO_2 were compared to those achieved with Pt-promoted TiO_2 at 375 and 425 nm. As expected, at 375 nm Pt nanoparticles showed a larger positive effect than Au nanoparticles, explained by the higher catalytic efficiency of Pt in the oxygen reduction reaction; an essential half reaction in converting alkanes over photo-excited TiO_2. Surprisingly, the effect of Pt nanoparticles was much lower than of the Au nanoparticles in the reaction performed at 425 nm. This strongly suggests that besides a catalytic effect, plasmonic phenomena induced by Au at 425 nm result in an additional enhancement of activity. Since at 525 nm the catalyst is completely inactive, we propose this plasmonic effect requires overlap in absorption intensity of P25 and Au nanoparticles, allowing so-called plasmon resonance energy transfer (see Figure 2).

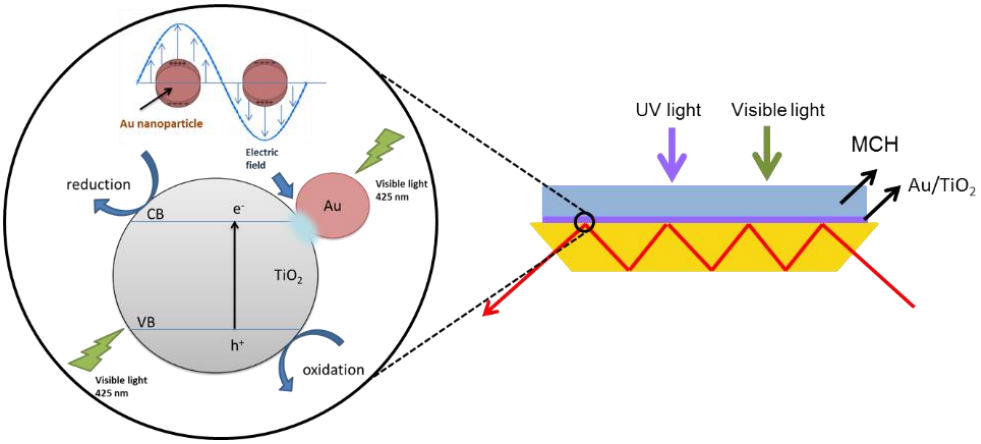

Figure 2: Graphical abstract of chapter 4, showing that "plasmon resonance energy transfer" is the main phenomenon to explain high performance of Au/TiO_2 in MCH oxidation as analyzed by ATR-FTIR spectroscopy.

Chapter 5 is focused on the synergetic effect of Pt nanoparticles and Cr^{6+} in enhancement of the photocatalytic oxidation activity of TiO_2, prepared by a sol gel based procedure. Besides Cr^{6+}, other modifications of the TiO_2 structure investigated include the incorporation of Ag, Cu, and V and Pt ions in the TiO_2 crystal structure. The sol-gel synthesized materials were characterized by XRD, BET, TEM, and Raman and UV/Vis spectroscopy. UV-Vis spectroscopy showed significant visible light absorption was induced by incorporation of ions in the TiO_2 lattice, especially for Cr/TiO_2 and V/TiO_2. These were also found the most effective in visible light oxidation of MCH. To further enhance the performance of Cr/TiO_2, Pt nanoparticles were synthesized on the surface of this material by methanol induced photodeposition. $Pt/Cr/TiO_2$ outperformed the other catalysts (TiO_2, Cr/TiO_2 or Pt/TiO_2) dramatically in oxidative conversion of MCH under visible light illumination.

Chapters 3, 4 and 5 are focused on oxidation of MCH as a model reaction for selective, photocatalytic oxidation of hydrocarbons in the liquid phase. In **chapter 6**, another model reaction was investigated, i.e. the conversion of ethanol, when present in the gas phase. Photocatalytic ethanol conversion is relevant for air purification. Pt/WO_3 prepared by an impregnation method was found to be very effective in the

oxidative dehydrogenation of ethanol to acetaldehyde and CO_2, even in dark conditions. The activity and selectivity of Pt/WO_3 strongly depends on the nature of the Pt species. PtO containing WO_3 was completely ineffective for the (dark) reaction. The remarkably high (dark) activity of the Pt/WO_3 is likely related to interfacial synergy between the Pt particles and the WO_3 surface. A graphical abstract, summarizing the main result of this chapter is shown in Figure 3.

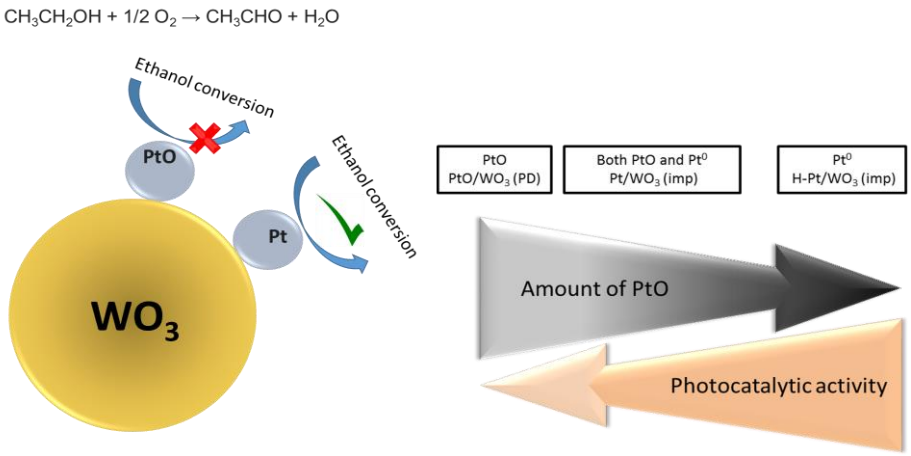

Figure 3: Graphical abstract, showing the main results of chapter 6.

Finally, in **chapter 7**, two modifications of silica supported Ti catalysts were prepared to enhance performance in photocatalytic conversion of CO_2. Adding ZnO nanoparticles, which were anticipated to increase the sorption of CO_2, led to a smaller apparent rate in hydrocarbon production. Addition of visible light absorption functionality by CrO_x, was even more detrimental to the observed production of hydrocarbons. Both ZnO and CrO_x addition to Ti-TUD-1 lead to significantly enhanced rates in the backward reactions of intermediates, such as formaldehyde, as well as of the produced hydrocarbons (in particular ethylene), explaining the negative effect of these additions to the catalyst composition. Figure 4 shows a schematic overview of the reversibility of photocatalytic reduction of CO_2 to light hydrocarbons over ZnO-Ti-TUD-1 or Cr-Ti-TUD-1.

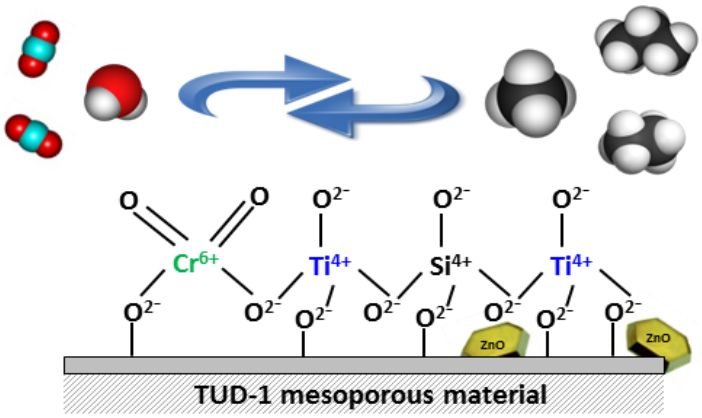

Figure 4: Schematic overview of the reversibility of photocatalytic reduction of CO_2 to produce light hydrocarbons over ZnO-Ti-TUD-1 or Cr-Ti-TUD-1.

Samenvatting

De focus van het onderzoek dat in deze thesis beschreven wordt is het ontwikkelen van effectieve fotokatalysatoren die de oxidatieve omzetting van koolwaterstoffen kunnen katalyseren. Deze werden gefabriceerd door middel van een aantal methodes zoals sol-gel chemie, in combinatie met impregnatie of fotodepositie van metalen nanodeeltjes. De gemaakte materialen werden gekarakteriseerd door verschillende technieken om hun compositie en morfologie te bepalen. Hun fotokatalytische prestatie werd onderzocht in meerdere oxidatieve omzettingen, zoals die van methylcyclohexaan (MCH), ethanol of simultane oxidatie van koolwaterstof mengsels. Hun prestatie werd geëvalueerd door gebruik te maken van verschillende technieken, zoals ATR-FTIR, DRIFT, een multi-reactor opstelling, en een van boven belichte reactor die het meten van op glas plaatjes aangebrachte coatings mogelijk maakte.

In **hoofdstuk 1** worden de basisprincipes van fotokatalyse geïntroduceerd. Ook wordt er een introductie gegeven over de fotokatalysatoren en de op SiO_2 gebaseerde katalysatoren (TUD-1), alsmede achtergrondinformatie voor een aantal algemene aspecten van het mechanisme achter de plasmonische versterking van fotokatalytische activiteit.

In **hoofdstuk 2** wordt een overzicht gepresenteerd van de experimentele procedures. Een introductie tot IR spectroscopie wordt gegeven, met een focus op analyse met twee verschillende reactie cellen: één voor metingen in de vloeistoffase (ATR) en één voor metingen in de gasfase (DRIFT). Verder wordt een fotokatalytische reactor met gas chromatograaf (GC) beschreven, en het gebruik van een opstelling met meerdere reactoren voor de evaluatie van fotokatalyse in de gasfase.

In **hoofdstuk 3** wordt aangetoond dat blauw TiO_2 een actievere fotokatalysator is voor de oxidatie van MCH dan P25 en commercieel rutiel TiO_2, in het bijzonder bij 425 nm. Blauw TiO_2 produceerde ketonen ook meer selectief ten opzichte van CO_2. Helaas leed deze katalysator wel onder deactivering als gevolg van foto-geïnduceerde oxidatie van Ti^{3+} naar Ti^{4+} door moleculaire zuurstof. Een schematische weergave van het MCH oxidatieproces over verschillende fotokatalysatoren (i.e. blauw TiO_2, P25 en rutiel TiO_2) is weergegeven in Figuur 1.

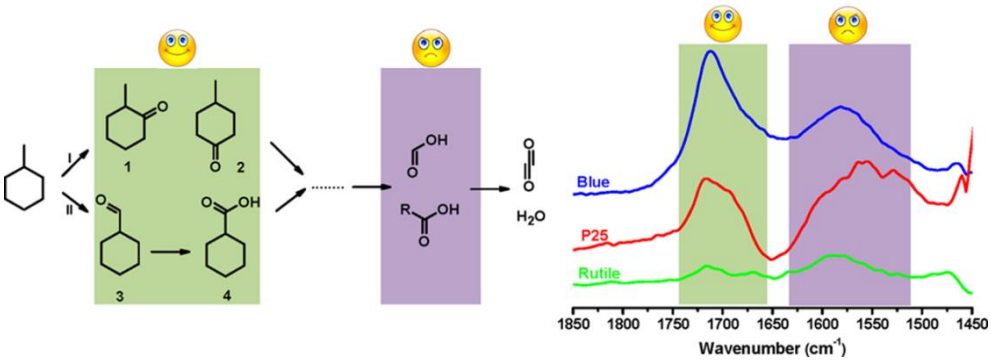

Figuur 1: Schematisch overzicht van MCH oxidatieprocessen en de spectra geobserveerd voor blauw TiO_2, P25 en rutiel.

De invloed van Au nanodeeltjes, gemaakt met depositie-precipitatie, werd geëvalueerd op het versterken van de fotokatalytische activiteit van P25 voor de oxidatie van MCH. De resultaten zijn te vinden in **hoofdstuk 4**. In-situ ATR-FTIR spectroscopie werd gebruikt om de reactiesnelheden te vergelijken. Belichting werd geïnduceerd door middel van een reeks LEDs met afwisselend golflengtes van 375 en 525 nm, of 425 en 525 nm. Bij 375 en in het bijzonder bij 425 nm verbeterde Au de reactiesnelheid significant. Het belichten van Au-gepromoot P25 bij 525 nm leverde geen meetbare activiteit op, noch leverde de toevoeging van dit licht verdere verbetering op bij 375 of 425 nm. Dit sluit de invloed van verhitting van de Au deeltjes op de reactiesnelheid bij 375 en 425 nm uit. Om te valideren of de verbetering puur katalytisch was, of dat plasmonische effecten relevant waren, werden de reactiesnelheden van Au/TiO_2 vergeleken met die bereikt met Pt-gepromoot TiO_2 bij 375 en 425 nm. Zoals verwacht vertoonde de Pt nanodeeltjes bij 375 nm een groter positief effect dan de Au deeltjes, wat verklaard wordt door het grotere katalytische effect van Pt in de zuurstofreductiereactie; een essentiële halfreactie voor de conversie van alkanen over foto-geëxciteerd TiO_2. Verassend genoeg was het effect van de Pt nanodeeltjes veel lager dan dat van de Au nanodeeltjes bij 425 nm. Dit suggereert sterk dat naast een katalytisch effect, er ook een plasmonisch fenomeen geïnduceerd wordt door Au bij 425 nm dat leidt tot een extra versterking van de activiteit. Aangezien bij 525 nm de katalysator compleet inactief is, stellen wij dat dit plasmonische effect een overlap in absorptie intensiteit van P25 en Au vereist, waardoor zogenaamde plasmonen-resonantie energieoverdracht toegestaan wordt (zie figuur 2).

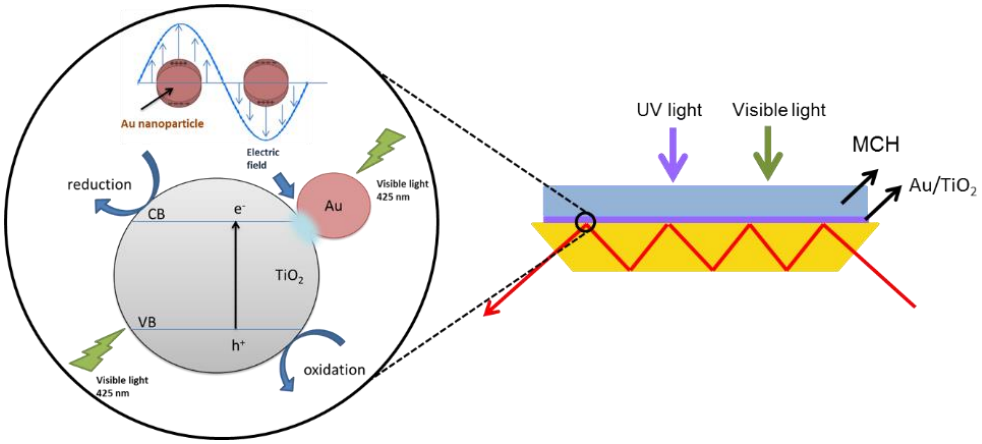

Figuur 2: Grafisch uittreksel van hoofdstuk 4, waarin gedemonstreerd wordt dat "plasmonen-resonantie energieoverdracht" het voornaamste fenomeen is dat de goede prestatie verklaard van Au/TiO_2 voor MCH oxidatie zoals geanalyseerd door ATR-FTIR spectroscopie.

In **hoofdstuk 5** ligt de nadruk op het synergetische effect van Pt nanodeeltjes en Cr^{6+} promotie van de katalytische oxidatieactiviteit van TiO_2, gemaakt met een sol-gel procedure. Naast Cr^{6+} worden andere modificaties van de TiO_2 structuur onderzocht, onder andere het inbrengen van Ag, Cu, V en Pt ionen in de TiO_2 kristalstructuur. De materialen gemaakt met sol-gel synthese werden gekarakteriseerd door XRD, BET, TEM en Raman- en UV-Vis spectroscopie. Dat laatste gaf aan dat significante absorptie van zichtbaar licht werd geïnduceerd door het inbrengen van ionen in het TiO_2 rooster, in het bijzonder Cr/TiO_2 en V/TiO_2. Deze werden ook het meest effectief bevonden voor de oxidatie van MCH bij zichtbaar licht. Om de prestatie van Cr/TiO_2 verder te verbeteren werden Pt nanodeeltjes gesynthetiseerd op de oppervlakte van het materiaal door methanol-geïnduceerde fotodepositie. $Pt/Cr/TiO_2$ presteerde dramatisch veel beter dan de andere katalysatoren (TiO_2, Cr/TiO_2 or Pt/TiO_2) voor de oxidatieve conversie van MCH onder bestraling met zichtbaar licht.

Hoofstukken 3, 4 en 5 zijn gericht op de oxidatie van MCH als modelreactie voor selectieve fotokatalytische oxidatie van koolwaterstoffen in de vloeistoffase. In **hoofdstuk 6** wordt een andere model reactie onderzocht, i. e. de omzetting van ethanol in de gasfase. Fotokatalytische conversie van ethanol is relevant voor

luchtzuivering. Pt/WO_3, gemaakt met een impregnatiemethode, bleek zeer effectief te zijn in het oxidatief dehydrogeneren van ethanol naar acetaldehyde en CO_2, zelfs onder donkere omstandigheden. De activiteit en selectiviteit van Pt/WO_3 hangt sterk af van de vorm van het Pt. WO_3 met PtO was volledig ineffectief bij de (donkere) reactie. De opmerkelijk hoge activiteit van het Pt/WO_3 is waarschijnlijk gerelateerd aan synergie die plaatsvindt op de raakvlakken van de Pt deeltjes en het WO_3 oppervlak. Een grafische weergave van de voornaamste conclusies van dit hoofdstuk worden samengevat in Figuur 3.

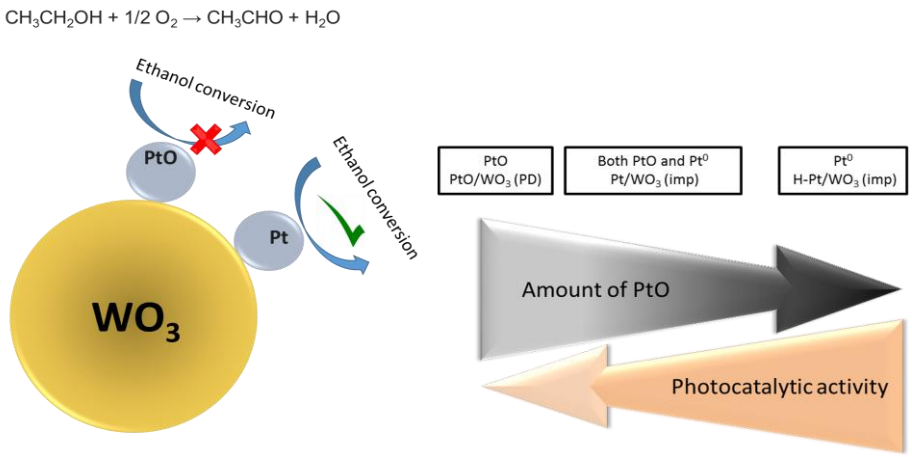

Figuur 3: Grafische weergave van de voornaamste conclusies van hoofdstuk 6.

Tot slot staat in **hoofdstuk 7** beschreven hoe SiO_2-ondersteunde Ti katalysatoren werden gemaakt om de prestatie met betrekking tot de fotokatalytische omzetting van CO_2 te verbeteren. Het toevoegen van ZnO nanodeeltjes, waarvan verwacht werd dat deze de sorptie van CO_2 zouden vergroten, leidde tot een tragere vorming van koolwaterstoffen. De toevoeging van de mogelijkheid tot absorptie van zichtbaar licht door middel van CrO_x resulteerde in nóg lagere koolwaterstof productie. Zowel ZnO als CrO_x toevoeging aan Ti-TUD-1 leidde tot significant verhoogde terugwaartse reactiesnelheden van intermediaire verbindingen zoals formaldehyde, alsook van de geproduceerde koolwaterstoffen (met name ethyleen), wat het negatieve effect van deze toevoegingen verklaart. Figuur 4 laat een schematisch overzicht zien van de omkeerbaarheid van de fotokatalytische reductie van CO_2 naar lichte koolwaterstoffen over ZnO-Ti-TUD-1 or Cr-Ti-TUD-1.

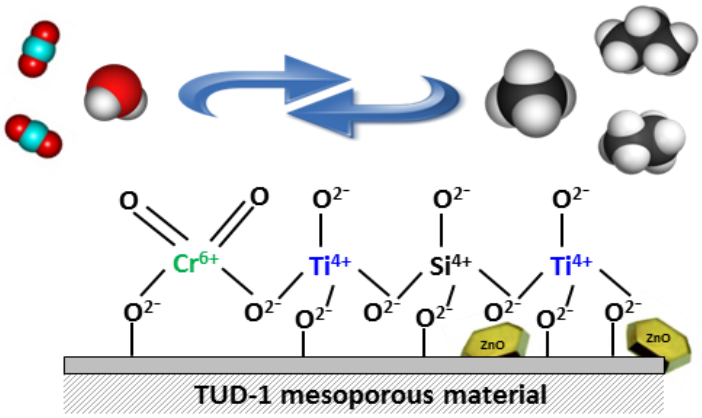

Figuur 4: Schematisch overzicht van de omkeerbare fotokatalytische reductie van CO_2 naar lichte koolwaterstoffen over ZnO-Ti-TUD-1 or Cr-Ti-TUD-1.


الحمد لله رب العالمين

Acknowledgements

First of all, I would like to thank my supervisor, Prof. dr. Guido Mul, who gave me the opportunity to work in the Netherlands at the PCS group. Guido thanks for all your guidance and support during my PhD and your always open office policy for my questions. You changed my mind about the word "Prof. dr….". Despite your busy schedule, you helped me several times when I had a trouble with IR spectroscopy in the lab. Guido, thanks for all our weekly discussions and your never-ending positive attitude. I will always remember our long meetings when we discussed about results and also your patience with my crazy scientific questions.

Prof. dr. Mohamed S. Hamdy, I was so lucky that you were my daily supervisor during the first two years of my PhD. Hamdy, thanks for all your help, I really enjoyed working with you. Thanks for guiding me in many areas even after leaving the Netherlands you were continuously guiding me by e-mails.
I would like to thank the rest of committee members, Prof. dr. Leon. Lefferts, Prof. dr. Andre ten Elshof, Prof. dr. Rob Lammertink, Prof. dr. James Anderson and Dr. Jennifer Strunk for making time to evaluate my thesis.
I would also like to thank Dr. Bastian Mei, and Dr. Ilya Sinev from the Ruhr University Bochum for the collaboration in the research described in chapter 7.

Many thanks to Robert, for all the support in the PCS labs, especially your efforts to connect the gas controller to the DRIFT set-up. That was a substantial help in my projects. Also, I would like to thank Bert, technician of the CPM group, helping us by providing a new OPUS software. In addition, for his great help to solve our problems with the cooling system of the IR spectrometer. Lidy, I would like to thank you for arranging many documents. I am sure I took your time more than other PhDs during these years, thanks Lidy.

Kasper, it was my pleasure to work with you all these years. Thanks for introducing me to most of the equipment in the labs: XRD, UV-Vis, the GC and so on, and also all your help to solve issues with the GC setup. Thanks for your kind help to translate dozens of Dutch letters. Joana and Sun-Young, we had many delightful moments together. Joana, special thanks that you accepted to join me at Halal restaurants every night in Lyon when we went for EuropaCat congress. I will never forget your kindness. Sun-Young, thanks for all your kind help, your advice when I had an oral presentation in the NCCC conference and a lot of things you offered me when I moved from the campus. Alexander, we never had a collaboration together, but many thanks that every time I asked a question, you tried to find the best and complete

answer. Vera, although you just joined our group a few months ago, thanks for the positive energy that you brought to our group and also thanks for translating my summary to Dutch.

Moreover, I would like to thank all present and former PCS group members as well as all students and visitors in our group, especially Kai, Yuxi, Alexandere, Recep, Robert, Nesha, Bindikt, Michel, Vic, Mehrzad, Zheng, Yi, Yan, Khalid, Engin, Hendra, Yang, and Chieh-Chao. During my PhD, I enjoyed all the social activities we had at the coffee and lunch breaks, our excursions to Berlin and Valencia and all the NCCC conferences.

I would like to thank Besma and Hadis who accepted to be my paranymphs during the defence of my PhD dissertation. Besma, you know that you are my dear friend and I am so happy that I can meet you again after you moved to U.S. I am sure we will keep in touch. My invitation to visit Iran is always there for you and your family whenever you like. Hadis, I never forget you and your husband offered your apartment when we did not have a place to stay. Each Arbaeen, I will remember your hospitality. Also many thanks that you helped me to design my cover page.

I would like to extend my deepest gratitude to all my Iranian friends in the Netherlands for all enjoyable moments we shared during these years and for all our Saturday gatherings. Maryam (Hajighasemi), we had many special events and moments in your house. For sure I miss your kind hospitality, your delicious dinners. Also special thanks for all supports from you and your husband both when I was alone here. Zahra (Taghikhaki), we really miss you after you left Enschede, I am sure many families remember the kind help from you during your stay. Thank you and your husband for great parties and trips that we had together. Fatemeh (Mahmoudi), Narges, Hajar, Shokoufeh, Vahan, Neda, Hengameh, Maryam (Khodaverdian), Fatemeh (Nouri), Maedeh, Elaheh, Mahdeih, Sara, Zeinab, and Tahereh, with you and your families, I always felt that I was in Iran, thank you for your unwavering friendship.

I would like to acknowledge and thanks my parents for all their encouragement and love. Without you it was impossible to even start this journey. Mother, with no doubt you are my best friend, and best teacher in every single moment of my life. Thanks father, I couldn't have done it without your huge supports throughout all the ups and downs of my education. Thanks to my beloved brothers, Mohammad, Ali and

Hamid, and my wonderful sister, Reihaneh. You know how much I love you. Thanks to all our almost daily calls, your positive energy your inspiring words.

Last but not least, I would like to acknowledge and thank my husband, Mohammad Jamal, the soul of my life. Jamal I am so proud of myself because of having you. I need something more than words to express my love to you for your great support and unconditional love. We have experienced many things together. We laughed together, travelled a lot and discussed about everything. You always stand next to me in all the good and bad moments. Thanks for your love.

The Author

Rezvaneh Amrollahi Buky received her B. Sc. Degree in Physics (both atomic and solid-state fields) from University of Science and Technology (IUST), Iran in 2005. She obtained her M. Sc. Degree in Physics from Sharif University of Technology, in 2009. In 2011, November, she moved to the Netherlands and joined the PhotoCatalytic Synthesis (PCS) group at the University of Twente to pursue her PhD degree in the field of photocatalysis.

A list of publications in which she participated at the University of Twente is as follows:

- Synergy between Pt nanoparticles and Cr^{6+} in the photocatalytic performance of sol-gel derived TiO_2'.

R. Amrollahi, M. S. Hamdy, G. Mul; to be submitted

- Room temperature selective (photo) catalytic oxidation of ethanol to acetaldehyde over Pt/WO_3

R. Amrollahi, K. Wenderich, G. Mul; submitted to ACS Applied Materials and Interfaces

- How Pt nanoparticles affect TiO_2 induced gas phase photocatalytic oxidation reactions

B. D.Fraters, R. Amrollahi, G. Mul

Journal of Catalysis, 2015, 324, pp119–126.

- Strategies to Design Efficient Silica-Supported Photo-catalysts for Reduction of CO_2

M. S. Hamdy, R. Amrollahi,I. Sinev, B.Mei, G. Mul

Journal of the American Chemical Society (**JACS**), 2014, 136 (2), pp 594–597.

- Understanding promotion of photocatalytic activity of TiO_2 by Au nanoparticles"

R. Amrollahi, M. S. Hamdy, G. Mul

Journal of Catalysis, 2014, 319, pp 194–199.

- Surface Ti^{3+} Containing (blue) Titania: A Unique Photocatalyst with High Activity and Selectivity in Visible Light-Stimulated Selective Oxidation

M. S. Hamdy, R. Amrollahi, G. Mul

ACS Catalysis, 2012, 2 (12), pp 2641-2647.

The focus of the research was on the engineering and design of effective photocatalysts able to catalyze the oxidative conversion of hydrocarbons. The prepared catalysts were synthesized by using different procedures involving sol-gel precursors, and impregnation or photo-deposition of metallic nanoparticles. The photocatalytic performance of the prepared materials was investigated in different photocatalytic conversions such as MCH oxidation, ethanol oxidation, or simultaneous oxidation of mixtures of hydrocarbons.

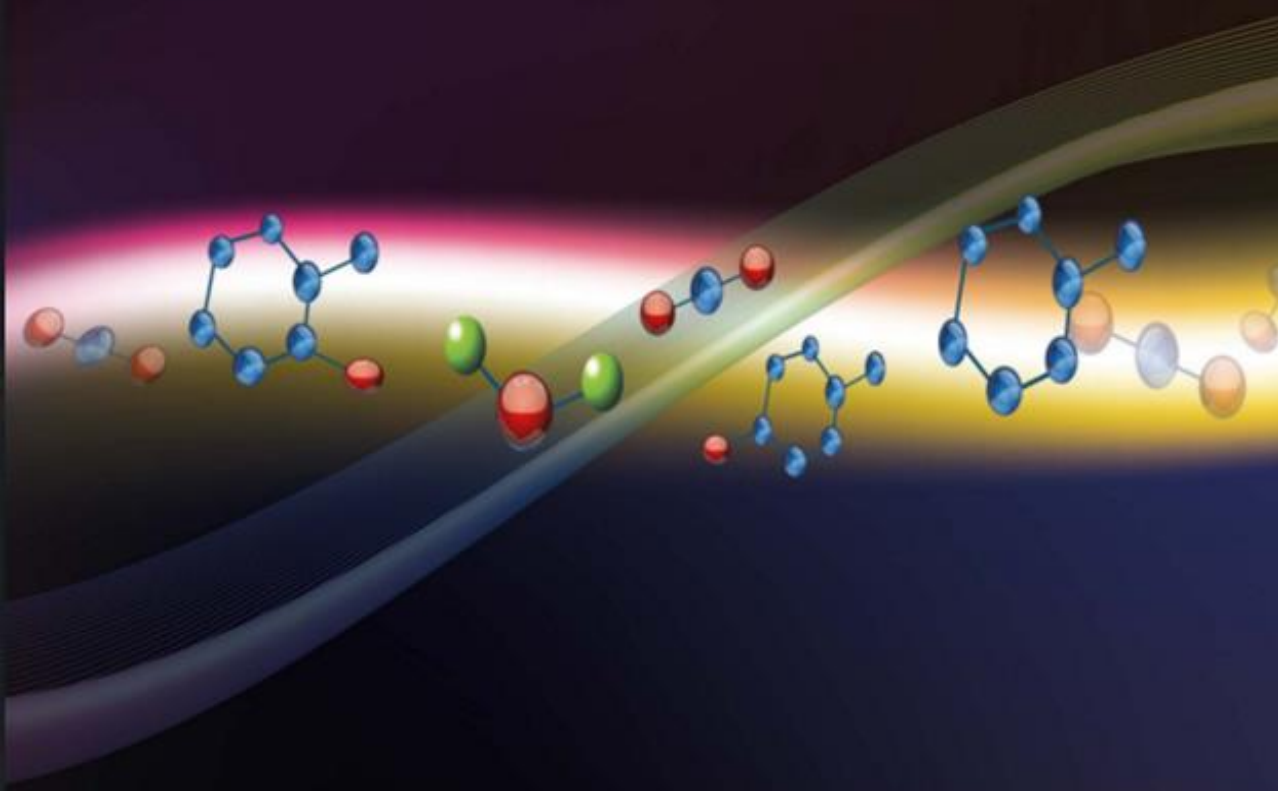

ISBN: 978-90-365-4065-0